

**IMPROVEMENT OF IT-SOFC BY TAILORING
THE MICROSTRUCTURE OF LSCF CATHODE
AND GDC ELECTROLYTE**

**A Thesis Submitted to
the Graduate School of Engineering and Sciences of
İzmir Institute of Technology
in Partial Fulfillment of the Requirements for the Degree of**

DOCTOR OF PHILOSOPHY

in Mechanical Engineering

**by
Can SINDIRAÇ**

**July 2019
İZMİR**

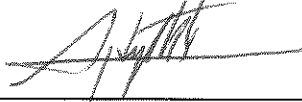
We approve the thesis of Can SINDIRAC

Examining Committee Members:



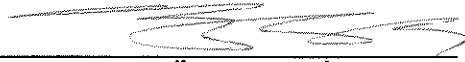
Prof. Dr. Sedat AKKURT

Department of Mechanical Engineering, İzmir Institute of Technology



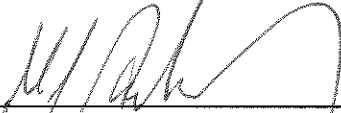
Prof. Dr. Ali Aydın GÖKTAŞ

Department of Metallurgical and Materials Engineering, Dokuz Eylül University



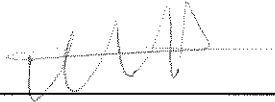
Assoc. Prof. Dr. Özgenç EBİL

Department of Chemical Engineering, İzmir Institute of Technology



Assist. Prof. Dr. M. Fatih TOKSOY

Department of Mechanical Engineering, İzmir Institute of Technology



Assist. Prof. Dr. Aligül BÜYÜKAKSOY

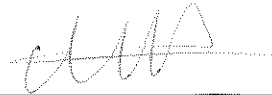
Department of Materials Science and Engineering, Gebze Technical University

11 July 2019



Prof. Dr. Sedat AKKURT

Supervisor, Department of
Mechanical Engineering
İzmir Institute of Technology



Assist. Prof. Dr. Aligül BÜYÜKAKSOY

Co-Supervisor, Department of
Materials Science and Engineering
Gebze Technical University



Prof. Dr. Sedat AKKURT

Head of the Department of
Mechanical Engineering

Prof. Dr. Aysun SOFUOĞLU

Dean of the Graduate School of
Engineering and Sciences

ACKNOWLEDGMENTS

In the beginning, I would like to express sincere gratitude to my advisor Prof. Dr. Sedat Akkurt, who is one of the best mentors a student can have. Since my first day in IYTE, Dr. Akkurt believes me like nobody else and gave continuous support and his excellent academic guidance. His endless patience and motivations during my Ph.D. are beyond my imagination. I will always be thankful throughout my life for his advices about science and life.

I am also very grateful to my co-advisor, Assist. Prof. Dr. Aligül Büyükaksoy for his scientific advice and insightful discussions. Beyond his academic advises, his encouragements and guidance to complete tasks are so precious for me and hard to forget in entire my life.

Besides my advisors, I would like to thank the rest of my dissertation committee members, Assoc. Prof. Dr. Özgenc Ebil and Assist. Prof. Dr. M. Fatih Toksoy for their invaluable advises and feedbacks. Besides, I am grateful to Dr. Ebil and Prof. Dr. Muhsin Çiftçiođlu, who gave me access to their laboratories and provided me to finish a part of this thesis.

I want to thank TUBITAK for their financial support.

I am thankful to Seda akırlar, who is my fellow lab mate for her hardworking in our projects to finish them before deadlines. Moreover, I also would like to thank all my colleagues at the Izmir Institute of Technology who have been supporting me during my research and the writing process. I am thankful for IYTE MAM members, Murat Mirza, Sedat elik, Devrim zalp, and Mesut Altınay for their technical assistance.

I am sincerely thankful to Bekir Dursun who always a great supporter to me and encourage me when I really need since my childhood. Besides, I would like to thank my workmates Dođuş Zeren, Mehmet Deniz Guneş, Cihan Turhan, Salim Cenk Elmacı, Asena Altan, yküm Kırsoy, Sıla Tura Baykara for all delightful conversations and discussions during coffee sessions.

Last but definitely not least, I sincerely express my deepest gratitude to my parents, zhan Sındıra and Filiz Sındıra and my beloved fiancée, Merve Bozdemir. This dissertation would not have been possible without their continuous support, warm love, and patience.

ABSTRACT

IMPROVEMENT OF IT-SOFC BY TAILORING THE MICROSTRUCTURE OF LSCF CATHODE AND GDC ELECTROLYTE

The high operating temperature of solid oxide fuel cells (SOFC) brings about some restrictions like the high cost of fuel cell, long start-up time, thermal stress, and decreasing lifetime. Thus, lowering the operating temperature is vital for improvement of SOFC. However, reducing the operating temperature leads to some negative effects on solid oxide fuel cell performance by increasing the electrolyte and electrode resistances.

This dissertation focuses on tailoring the cathode and/or electrolyte layers to obtain improved electrochemical performances. For this purpose, some strategies are proposed. These are (i) thin film cathode nanocomposite cathode layer formation, (ii) infiltration of porous GDC by LSCF/LSCF+GDC, (iii) infiltration of porous GDC by GDC solution to improve densification at lower temperature and finally (iv) electrochemical characterization of GDC densified by infiltration.

ÖZET

LSCF KATOT VE GDC ELEKTROLİTİNİN MİKROYAPISININ MODİFİYE EDİLMESİYLE OS-KOYH PERFORMANSININ İYİLEŞTİRİLMESİ

Katı Oksit Yakıt Hücreleri'nin (KOYH) yüksek çalışma sıcaklıkları; yakıt hücresinin pahalı olması, uzun açılış süreleri, termal stress ve ömrün azalması gibi sorunlara neden olmaktadır. Bu yüzden, KOYH'ların çalışma sıcaklıkları düşürülmesi oldukça önem taşımaktadır. Fakat, çalışma sıcaklığını düşürmenin elektrolit ve elektrot rezistansını arttırdığından dolayı KOYH performansı üzerinde olumsuz etkileri vardır.

Bu tezde, katot ve elektrolit katmanlarının modifiye edilerek elektrokimyasal performansının iyileştirilmesine odaklanmıştır. Bu amaçla bazı stratejiler önerilmiştir. Bunlar (i) ince film nanokompozit katot tabakası oluşturulması (ii) LSCF ve LSCF+GDC solusyonlarının boşluklu GDC tabakasına infiltre edilmesi (iii) boşluklu GDC yapısının GDC solusyonu infiltre edilerek düşük sıcaklıklarda yoğunlaştırılması ve son olarak (iv) infiltrasyon ile yoğunlaştırılmış GDC elektrolitinin elektrokimyasal özelliklerinin incelenmesi.

TABLE OF CONTENTS

LIST OF FIGURES	ix
LIST OF TABLES	xv
CHAPTER 1 INTRODUCTION	1
1.1. Types of Fuel Cells.....	2
1.2. Advantages and Disadvantages of SOFCs	3
1.3. Operation of SOFCs	4
1.4. Open Circuit Voltage.....	5
1.5. SOFC Components and Materials	5
1.5.1. The Electrolyte	6
1.5.2. The Anode	7
1.5.3. The Cathode	8
1.6. Research Scope.....	10
1.7. References	13
CHAPTER 2 FABRICATION OF LSCF AND LSCF-GDC NANOCOMPOSITE THIN FILMS USING POLYMERIC PRECURSORS	16
2.1. Abstract.....	16
2.2. Introduction	17
2.3. Experimental Methods.....	19
2.3.1. Fabrication of Electrolyte Substrates	20
2.3.2. Fabrication of Electrolyte Substrates	20
2.3.3. Structural and Microstructural Characterization	21
2.3.4. Electrochemical Performance Analysis	22
2.3.5. Surface Analysis.....	22
2.4. Results and Discussions	23
2.4.1. Phase Analysis	23
2.4.2. Microstructural Analysis	24
2.4.3. Electrochemical Analysis.....	26
2.4.4. Long Term Stability Tests.....	31
2.5. Summary.....	36

2.6. References	37
CHAPTER 3 ELECTROCHEMICAL PERFORMANCE OF $\text{La}_{0.6}\text{Sr}_{0.4}\text{Co}_{0.2}\text{Fe}_{0.3}\text{O}_{3-\delta}$ - $\text{Ce}_{0.9}\text{Gd}_{0.1}\text{O}_{2-\delta}$ COMPOSITE SOFC CATHODES FABRICATED BY ELECTROCATALYST AND/OR ELECTROCATALYST-IONIC CONDUCTOR INFILTRATION	42
3.1. Abstract.....	42
3.2. Introduction	43
3.3. Experimental.....	46
3.3.1. Fabrication of the Dense GDC Electrolytes and Porous GDC Scaffold	46
3.3.2. Preparation of Polymeric Precursors and the Infiltration Process .	47
3.3.3. Crystal Structure and Microstructure Analyses	49
3.3.4. Electrochemical Performance Analysis	49
3.4. Results and Discussions	49
3.5. Conclusion.....	60
3.6. References	61
CHAPTER 4 LOWERING THE SINTERING TEMPERATURE OF SOLID OXIDE FUEL CELL ELECTROLYTES BY INFILTRATION	65
4.1. Abstract.....	65
4.2. Introduction	66
4.3. Experimental Methods.....	68
4.3.1. Fabrication of Porous GDC Scaffold Electrolyte.....	68
4.3.2. Polymeric Precursor Solution Preparation and Infiltration Process	69
4.3.3. Density Measurement.....	70
4.3.4. Structural and Microstructural Characterization	71
4.3.5. Coding of Samples	71
4.4. Results and Discussions	72
4.4.1. Crystal Structure Analyses	72
4.4.2. Weight and Density Measurements	72
4.4.3. Microstructural Analyses	76
4.5. Summary.....	82
4.6. References	83

CHAPTER 5 ELECTRICAL PROPERTIES OF GADOLINIA DOPED CERIA ELECTROLYTES FABRICATED BY INFILTRATION-AIDED SINTERING.....	87
5.1. Abstract.....	87
5.2. Introduction	88
5.3. Experimental Methods.....	90
5.4. Results and Discussions	92
5.5. Summary.....	103
5.6. References	105
CHAPTER 6 CONCLUSIONS	109

LIST OF FIGURES

<u>Figure</u>	<u>Page</u>
Figure 1.1. Comparison of emissions from different sources.....	1
Figure 1.2. Sketch of William Grove's fuel cell.	2
Figure 1.3. Classification of fuel cells	3
Figure 1.4. Schematic drawing of a fuel cells.....	4
Figure 1.5. Comparison of ionic conductivity of various electrolyte candidates.	7
Figure 1.6. A typical ABO_3 perovskite unit cell.....	9
Figure 1.7. Oxygen reduction reaction (ORR) steps in (a) pure electronic conductor, (b) electronic and ionic composite conductor and (c) mixed ionic- electronic conductor (MIEC).....	9
Figure 1.8. LSCF and LSCF-GDC nanocomposite deposition on dense GDC electrolyte by spin coating.....	12
Figure 1.9. Infiltration of LSCF and LSCF-GDC nanoparticles inside of porous thick GDC scaffold on dense GDC electrolyte symmetrically.	13
Figure 2.1. Graph showing the durations for which the LSCF and LSCF-GDC electrodes were exposed to each temperature	22
Figure 2.2. Thin film x-ray diffraction patterns of LSCF and LSCF-GDC, heat treated in air 500°C or 700°C	24
Figure 2.3. A representative scanning electron microscopy image of cross-section of LSCF-GDC nanocomposite thin film deposited onto GDC electrolyte, annealed in air at 700°C for 2 hours	25
Figure 2.4. Atomic force microscopy (AFM) images of single phase LSCF, annealed at (a) 500°C (b) 700°C for 4 hours and (c) at 600°C for 80 hours following the prior heat treatments. The bottom row shows the AFM images of LSCF-GDC composite thin films, also annealed at (d) 500°C, (e) 700°C for 2 hours, and (f) at 600°C for 80 hours using the same heat treatments.	25
Figure 2.5. Impedance spectra obtained from (a) LSCF/GDC/LSCF and (b) LSCF- GDC/GDC/LSCF-GDC symmetrical half cells at 600°C in air, (c) the equivalent circuit model used to fit the obtained impedance data	27

<u>Figure</u>	<u>Page</u>
Figure 2.6. Impedance spectra obtained from the temperature dependence of the polarization resistance ($ASR_{\text{electrode}}$) values obtained from the fitting of the impedance data. The polarization resistance data, obtained other groups have been added from comparison.	28
Figure 2.7. Schematic representation of the proposed oxygen pathways for (a) single phase LSCF and (b) LSCF-GDC nanocomposite cathode.	30
Figure 2.8. Changes in the impedance spectra obtained from (a) symmetrical LSCF/GDC/LSCF half-cells, (b) symmetrical LSCF-GDC/GDC/LSCF-GDC half-cells, and (c) the normalized polarization resistances of both the LSCF and LSCF-GDC thin film electrodes with time at 600 °C.	32
Figure 2.9. X-ray photoelectron spectroscopy survey scans of LSCF thin films a) prior to and b) after long-term annealing at 600 °C, in stagnant air, LSCF-GDC thin films c) prior to and d) after long-term annealing at 600 °C, in stagnant air.	33
Figure 3.1. Schematic representation of proposed pathways of oxygen ions at cathode layers prepared by (a) single phase LSCF and (b) LSCF+GDC polymeric precursor solution infiltration into porous GDC scaffolds.	47
Figure 3.2. Schematic representation of experimental flow chart depicting the formation of the porous scaffold, and the infiltration of the scaffold multiple times to deposit nano sized LSCF or LSCF+GDC.	48
Figure 3.3. Schematic representation of experimental flow chart depicting the formation of the porous scaffold, and the infiltration of the scaffold multiple times to deposit nano sized LSCF or LSCF+GDC.	51
Figure 3.4. Scanning electron microscopy (SEM) images of fractured cross sections of (a) a representative LSCF+GDC infiltrated cathode (40x) also including the Ag current collector and the electrolyte, (b) a previously sintered porous GDC scaffold layer without any infiltration, (c) porous GDC scaffold infiltrated 45 times with LSCF precursor solution after annealing at 700°C for 2h, (d) porous GDC scaffold infiltrated 45 times by LSCF precursor solution and heat treated at 700°C for 100 hours, (e) porous GDC scaffold infiltrated 30 times with LSCF+GDC solution after annealing at 700°C for 2h, (f) porous GDC scaffold infiltrated 30 times by LSCF+GDC precursor solution and heat treated at 700°C for 100 hours. ...	51

<u>Figure</u>	<u>Page</u>
Figure 3.5. Relative amounts of La, Sr, Co, Fe, Ce and Gd elements determined by energy dispersive X-ray spectroscopy (EDX) measurements performed at the middle part of the cathode layers prepared by (a) LSCF and (b) LSCF+GDC infiltration into porous GDC scaffolds.....	52
Figure 3.6. Heating/cooling schedule followed during impedance spectroscopy measurements	53
Figure 3.7. Impedance spectra obtained from cathodes prepared by a) 10x b) 20x c)30x d)35x e)40x f)45x g)50x LSCF infiltration into porous GDC scaffolds. Measurements were conducted on symmetrical half cells at 700°C, in air. The equivalent circuit models used to fit the obtained impedance data are provided in insets.....	54
Figure 3.8. a) Bode plots showing the impedance response of LSCF (50x) infiltrated symmetrical half-cell measured at 600, 650 and 700°C. (b) Temperature dependence of the cathode polarization resistance of infiltrated LSCF (50x) sample, also showing the individual contributions of the high and low frequency resistance components (i.e., R2 and R3) to total resistance. Impedance spectroscopy measurements were performed on symmetrical half-cells cells, in air.	55
Figure 3.9. (a) Bode plots showing the impedance response of LSCF (50x) infiltrated symmetrical half-cell measured at 600, 650 and 700°C. (b) Temperature dependence of the cathode polarization resistance.....	56
Figure 3.10. Impedance spectra obtained from cathodes prepared by a) 10x b) 20x c)30x d)40x LSCF+GDC infiltration into porous GDC scaffolds. Measurements were conducted on symmetrical half cells at 700°C in air. The equivalent circuit models used to fit the obtained impedance data are provided in insets.....	58
Figure 3.11. Temperature dependence of the cathode polarization resistances obtained from the impedance spectroscopy measurements of symmetrical half-cell with cathodes prepared by different amounts of (from 10x to 40x) LSCF+GDC infiltration into porous GDC scaffolds. Cathode polarization resistance of blank porous GDC layer brushed with silver current collector was also added for comparison.	59

<u>Figure</u>	<u>Page</u>
Figure 3.12. Long term stability test results (polarization resistance measured at 700°C) of the symmetrical cells with LSCF 45x and LSCF+GDC 30x infiltrated as a function of dwell time	60
Figure 4.1. Schematic representation of the sintering behavior of the consolidated GDC ceramic particles with and without polymeric GDC precursor infiltration. Here, the infiltrated GDC phase serves to i) form connections between particles that are otherwise uncoordinated (e.g., between particles 2 and 3), ii) increase the overall solids loading of the green body and iii) provide fast diffusion routes through its amorphous volume.....	70
Figure 4.2. X-ray diffraction patterns of a) blank, b) 15 or 20 times gadolinia doped ceria (GDC) infiltrated and c) 15, 20 or 25 times FeOx infiltrated GDC pellets sintered at 800-1500 °C (a) or 1000-1200 °C (b and c).....	73
Figure 4.3. Effect of the sintering temperature on the relative density of the GDC pellets. The sintering procedure was performed for 8 hours in stagnant air	73
Figure 4.4. a) Effect of polymeric gadolinia doped ceria (GDC) precursor infiltration cycles on the % weight increase of the porous GDC scaffolds when 0.02 (35-G-20), 0.04 (35-G-40), 0.06 (35-G-60) and 0.08 M (35-G-80) solutions are used, b) effect of the secondary heat treatment temperature on the final relative density of the GDC infiltrated porous GDC scaffolds when the infiltration was carried out for 25 or 35 cycles using polymeric precursor solutions with 0.04, 0.06 or 0.08 M concentrations and c) impact of solution molarity on the final relative density of the 25 or 35 times GDC infiltrated porous GDC scaffolds when the final heat treatment was carried out at 1200 °C.	75
Figure 4.5. a) Effect of polymeric FeOx precursor infiltration cycles on the % weight increase of the porous GDC scaffolds when 0.015 or 0.020 M solutions are used, b) effect of the secondary heat treatment temperature on the final relative density of the FeOx infiltrated porous GDC scaffolds when the infiltration was carried out for 25 or 35 cycles using polymeric precursor solutions with 0.01, 0.015 or 0.020 M concentrations and c) impact of solution molarity on the final relative density of the 25 or 35 times FeOx infiltrated porous GDC scaffolds when the final heat treatment was carried out at 1200 °C.	77

<u>Figure</u>	<u>Page</u>
Figure 4.6. Scanning electron microscopy images of the fracture surfaces of the gadolinia doped ceria pellets a) 800 b) 900 c) 1000 d) 1100 e) 1200 f) 1300 g) 1400 h) 1450 and i) 1500 for 8 hours in air. The insets provide higher magnification images.	78
Figure 4.7. Scanning electron microscopy images of the fractured surfaces of porous gadolinia doped ceria (GDC) scaffolds infiltrated for 25 cycles using a 0.04 M polymeric GDC precursor and heat treated at a-c) 1000 °C (25-G-40-1000) and d-f) 1200 °C (25-G-40-1200) for 8 hours in air, of porous GDC scaffolds infiltrated for 35 cycles using a g-i) 0.04 M (35-G-40-1200) and j-l) 0.08 M (35-G-80-1200) polymeric GDC precursor solution both sintered at 1200 °C for 8 hours in air. The images in the same row were taken from the top, middle and bottom sections (from left to right) of the same sample to observe the uniformity of the microstructure. The insets show higher magnification images.	78
Figure 4.8. Scanning electron microscopy images of the fractured surfaces of porous gadolinia doped ceria (GDC) scaffolds infiltrated with a polymeric FeOx precursor solution with a molarity of 0.015 M for 25 cycles, sintered at a-c) 1000 °C (25-F-15-1000) and d-f) 1200 °C (25-F-15-1200), porous GDC scaffolds infiltrated with a polymeric FeOx precursor with a molarity of 0.020 M for g-i) for 25 (25-F-20-1200) and j-l) 35 cycles (35-F-20-1200), sintered at 1200 °C for 8 hours in air. The images in the same row were taken from the top, middle and bottom sections (from left to right) of the same sample to observe the uniformity of the microstructure. The insets show higher magnification images.	80
Figure 4.9. Change in the atomic ratios of Fe, Ce and Gd cations in the FeOx infiltrated gadolinia doped ceria (GDC) ceramic which yielded a highest relative density of 97% (sample code: 25-F-15-1100-8) with distance from the top surface, obtained from energy dispersive x-ray spectroscopy (EDX) analyses. The regions where EDX measurements were collected are labelled as the «T», «M» and «B» on the scanning electron microscopy image of the cross-section of the sample and denote top, middle and bottom sections respectively.....	82

<u>Figure</u>	<u>Page</u>
Figure 5.1. Schematic representation of the infiltration-aided sintering process	90
Figure 5.2. The Scanning electron microscopy images of the fracture surfaces of all seven samples obtained in the secondary electron mode.	93
Figure 5.3. Variation of grain size with relative density for all samples 1-7.....	95
Figure 5.4. High frequency portions impedance spectra measured at 300°C for GDC fabricated by (a) conventional (b) infiltration-aided sintering along with their equivalent circuit fitting lines. The equivalent circuit models used to fit data are given as insets.....	96
Figure 5.5. Effect of grain size on the ratio of grain boundary resistivity to total resistivity as measured at (a) 300, (b) 350 and (c) 400°C.	98
Figure 5.6. Arrhenius plots of (a) bulk (grain) and (b) grain boundary conductivities of the seven samples and their activation energies.....	100
Figure 5.7. Temperature dependences of the total conductivities of all samples and their activation energies.....	101
Figure 5.8. Variation of total electrical conductivity with relative density for all samples	102
Figure 5.9. Open circuit voltage values obtained under stagnant air and 10% hydrogen – 90% argon at the cathode and anode sides respectively, at 450-700 °C in samples 3 and 7. Dotted lines are obtained from refs [56-57].	103

LIST OF TABLES

<u>Table</u>	<u>Page</u>
Table 2.1. Surface cation % of LSCF and LSCF-GDC thin films annealed at 700°C for 4 hours, before and after long term annealing at 600°C, obtained from x-ray photoelectron spectroscopy analyses	35
Table 3.1. Cathode polarization resistance values (per electrode) and the corresponding activation energies of LSCF infiltrated cathodes for prepared by different number of infiltration cycles measured at 700 °C	57
Table 3.2. Cathode polarization resistance values (per electrode) and the corresponding activation energies of LSCF infiltrated cathodes for prepared by different number of infiltration cycles measured at 700 °C	59
Table 4.1. Table showing the processing parameters and the corresponding sample code numbers.....	71
Table 4.2. Effect of sintering temperature on gadolinia doped ceria (GDC) grain size and relative density.....	79
Table 4.3. Grain size and relative densities of the gadolinia doped ceria (GDC) and the FeOx infiltrated porous GDC scaffolds.....	81
Table 5.1. The sample code numbers and related infiltration process parameters. Relative density and grain size values of final ceramics are also listed with the standard deviations in paranthesis. Note that 1-3 are not infiltrated.	93
Table 5.2. Area specific bulk (grain) and grain boundary resistances, along with the capacitance and summit frequency values extracted from the equivalent circuit fitting of the EIS data collected at 300°C.....	95
Table 5.3. Variation of activation energy of total electrical conductivity in the lower and higher temperature range. T* refers to the transition temperature and is 425°C for all samples in the present case.	102

CHAPTER 1

INTRODUCTION

The increase in world population and the use of more advanced technology for improved life standard lead to accelerated demand for energy which is mainly generated through fossil fuel resources negatively affecting on global warming as a result of CO₂ gas production [1]. Generation of efficient and clean electrical power is, thus, a big challenge that must be undertaken. [1,2]. Fuel cells can potentially play an important role in accomplishing this task. Contrary to conventional energy conversion devices, fuel cells can convert chemical energy to electrical energy directly without combustion [3]. As a result, fuel cells are considered as a promising, clean and reliable energy source (Figure 1.1).

As they work without combustion their efficiencies are not constrained by Carnot cycles, which provide significant enhancement in efficiency (> 60%) [3]. Further, these pollution-free devices operate with hydrogen providing a potential to liberate us from the use of fossil fuel resources which can reduce environmental risks [2]. Despite high tech aura of fuel cells, the basic principle of them was demonstrated by Sir William Groove, father of fuel cells, in 1839. He gained an electric current by connecting an oxygen cathode and a hydrogen anode. His experimental set-up is shown in Figure 1.2 [2,4].

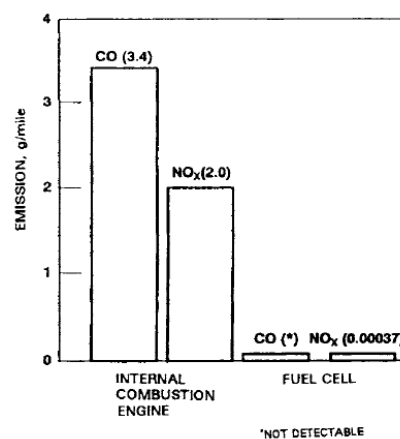


Figure 1.1. Comparison of emissions from different sources
(Source: Stamboli and Traversa, 2002)

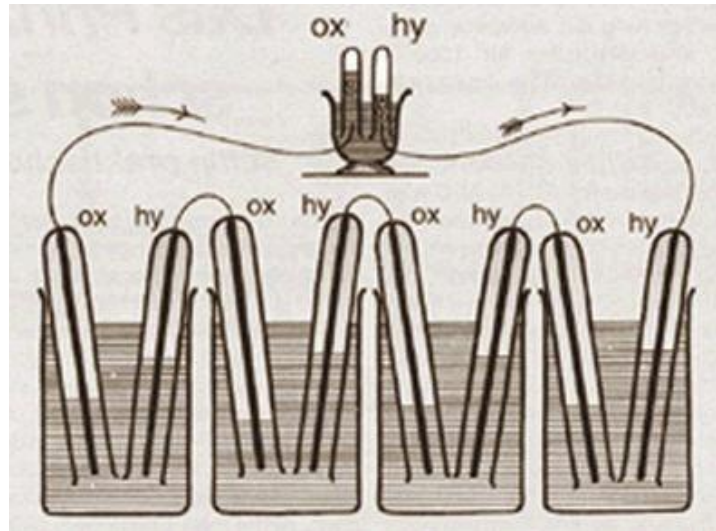


Figure 1.2. Sketch of William Grove's fuel cell.
(Source: Minh and Takahashi, 1995)

Historically, the major advance in the use of fuel cells appeared in 1960s in connection with the Apollo and Gemini space programs in NASA. Gemini 5 was the first spacecraft that used fuel cells instead of batteries in August 1965. Having water as the reaction product was the added benefit in space [5-6].

1.1. Types of Fuel Cells

All fuel cells consist of three components: a porous cathode, a porous anode, and an electrolyte layer in contact. A number of fuel cells have been designed and classified by the chemical nature of the electrolyte materials used in the cell. They are named after the type of their electrolyte as summarized in Figure 1.3 [7]. Low-temperature fuel cells (Proton Exchange Membrane Fuel Cells-PEMFC, Alkaline Fuel Cells-AFC) are mainly considered for cars due to short heating time. Although, efficiencies of LT fuel cells are low (i.e., in the range of 40-50%), but are still higher than the efficiencies of internal combustion engines. Molten Carbonate Fuel Cells (MCFC) and Solid Oxide Fuel Cells (SOFCs) are classified as high-temperature fuel cells [8]. They are developed for continuous power supply; therefore, they are suitable for use in power plants. Furthermore, efficiencies of high-temperature fuel cells are higher than low-temperature fuel cells. Besides, fuel variety is wider in HT-fuel cells than LT-fuel cells [8]. This dissertation is focused on SOFCs.

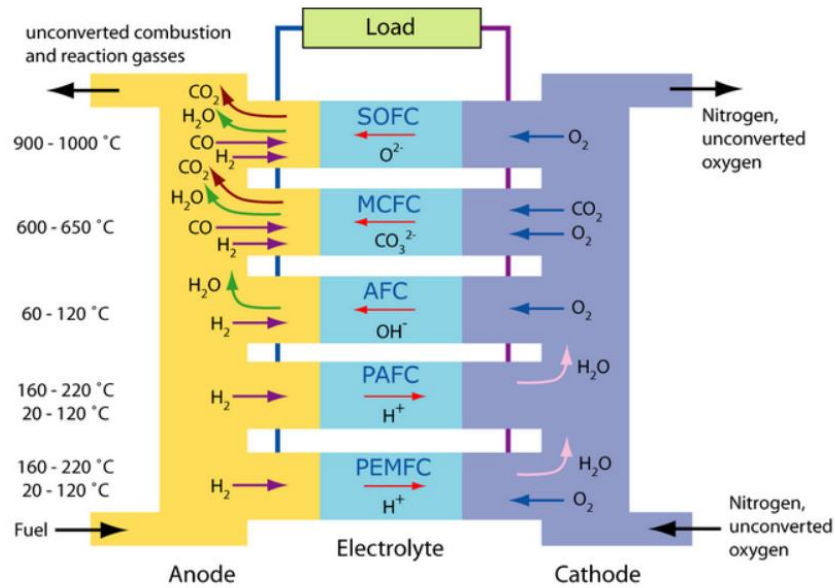


Figure 1.3. Classification of fuel cells
(Source: Singhal et.al., 2015)

1.2. Advantages and Disadvantages of SOFCs

In addition to the advantages of all fuel cells (i.e., clean and reliable operation), SOFC offer other advantages. These are;

- SOFCs have the highest efficiencies among the fuel cell types (>60%). Their efficiency rate can be increased by using combined heat and power (CHP) applications [1].
- Fuel flexibility that allows choice of carbon-based fuels, natural gas, biogas, etc. [1,2,9].
- High operating temperature allows the internal reforming of gaseous hydrocarbon fuels [1].
- SOFCs are modular, and they have almost no moving parts [4].
- SOFCs work quietly which makes their use indoors possible [10].
- A long-life expectancy as 40.000-80.000 hours [1].

Despite many advantages, SOFCs are still not fully commercialized due to difficulties in hydrogen storage, excessive materials and fabrication costs, long heat-up and cool-down times, and structural stresses that arise during operation due to cyclic expansion and contraction of components. Therefore, thermal expansion/contraction compatibility of components is crucial [1,8,11].

1.3. Operation of SOFCs

A typical SOFC system can be seen schematically in Figure 1.4. An SOFC single cell consists of three components; the fuel electrode (a.k.a. anode), the air electrode (a.k.a. cathode) and an electrolyte which is sandwiched in the middle. Additional components, such as interconnectors and sealants, are required to make stacks [12].

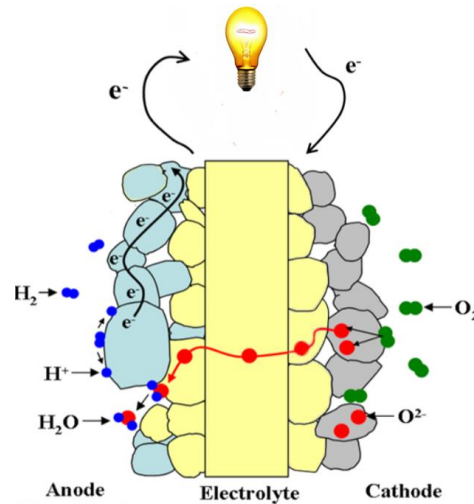
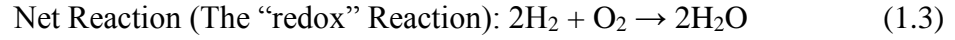
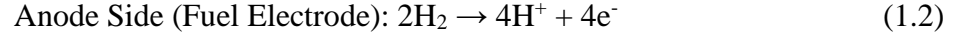
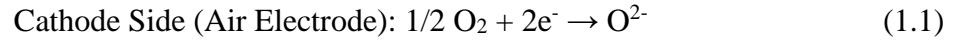


Figure 1.4. Schematic drawing of a fuel cells
(Source: Bowman et. al., 2013)

Working principle of SOFC is quite similar to batteries such as two electrodes and an electrolyte produce electricity via electrochemical reactions. However, unlike batteries, SOFCs does not require recharging or run down [14]. SOFCs generate electricity as long as they are fed by oxygen and hydrogen much like filling the gas tank of a car. Hydrogen fuel is fed onto the anode component while the cathode is fed by oxygen. Oxygen molecules are adsorbed and reduced to oxygen ions by oxygen reduction reactions (ORR) as given in Equation 1.1. Once generated, the oxygen ions need to travel through the cathode, electrolyte and anode to meet with hydrogen to produce electrons and water vapor. This makes it necessary for the electrolyte to provide a fast and easy pathway for ion conduction. So a good electrolyte is one that is ion-conducting and gas-tight. Air and fuel electrodes, on the other hand, need to be porous to maximize surface reactions. At the surface of the fuel electrode (anode) oxidized hydrogen ion (H^+) reacts with the oxygen ion (O^{2-}) that just came through the electrolyte to form water and electrons (see Equations 1.2 and 1.3). The released electrons run through the outside of the cell via an external circuit. Therefore, electrons can be fed back into the cathode to

complete the electrical circuit [15-16]. As long as fuel and oxygen are fed to the cell, the system will work consistently and will generate electricity.



1.4. Open Circuit Voltage

The electrochemical potential difference due to the difference in the oxygen partial pressures between both electrodes is the driving force for SOFC; and it is called as "open circuit voltage (OCV)" [12]. OCV is calculated via Nernst equation (Equation 1.4 and 1.5). Basically, OCV is the measured voltage since current equals zero [14-15].

$$\text{OCV} = E_0 - \frac{RT}{nF} \ln(K) \quad (1.4)$$

where

$$K = \frac{\rho_{\text{H}_2\text{O}}}{\rho_{\text{O}_2}^{0.5} \rho_{\text{H}_2}} \quad (1.5)$$

where R is the universal gas constant (8.314 J.K⁻¹.mol⁻¹), n is the number of electrons, T represents the operating temperature in Kelvin, E₀ is the cell voltage at standard conditions, F is the Faraday constant (9.65x10⁴ C.mol⁻¹). OCV range of a single cell is around 0.9-1.1 eV which frequently decreases due to polarization losses (i.e., ohmic losses, polarization resistances, etc.). Therefore, practical OCV is lower than its ideal potential [15]. Decreases in OCV are signals that report degradation in SOFC power output. If less than 0.7 eV it indicates gas leakage in electrolyte [2-4].

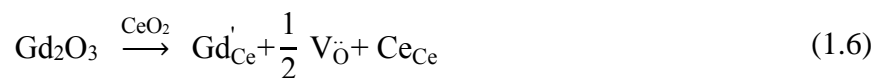
1.5. SOFC Components and Materials

Requirements of components make the material selection for SOFC challenging. This section deals with materials of electrolyte, anode and cathodes.

1.5.1. The Electrolyte

Ionic conductivity of the electrolyte layer must be high since it is responsible for conducting oxygen ions from the cathode side to the anode. Therefore, ionic conductivity must be greater than $0.01 \text{ S}\cdot\text{cm}^{-1}$ at the operating temperature. Also, the electrolyte layer possesses low electronic conductivity to block electrons to diffuse inside electrolyte and hence, electrons flow through the external circuit. Moreover, the electrolyte layer must be dense (at least 95 relative density) to ensure gas impermeability in order to avoid violent burn-out. Furthermore, it must be thermodynamically stable at reducing and oxidizing conditions as it is exposed to both atmospheres. Finally, Coefficient of Thermal Expansion (CTE) of electrolyte material must be compatible with anode and cathode. The temperature dependences of ionic conductivities of potential materials for electrolyte [16] are shown in Figure 1.5. Despite high ionic conductivity values of LaGaO_3 -based perovskites (also referred as LSGM) [17-18] and bismuth oxide (BiO_2) [19] have drawbacks like their high electronic conductivity and instability under reducing atmosphere. These issues lead to degradation in the maximum open circuit voltage due to electronic leakage [20]. Additionally, their costs are much higher than other candidates.

For these reasons, yttria-stabilized zirconia (YSZ) has been most popular electrolyte material due to its high ionic conductivity values at high-temperature range (i.e., 0.03 S/cm and 0.01 S/cm at 800°C and 1000°C , respectively) [2]. However, YSZ electrolyte dramatically loses its ability of good ionic conductivity when the operating temperature is reduced to the range of $500\text{-}700^\circ\text{C}$ which renders it useless. Extensive research for a replacement electrolyte in this temperature range came up with CeO_2 doped with Gd_2O_3 , Sm_2O_3 , etc with $\text{Ce}_{0.9}\text{Gd}_{0.1}\text{O}_{1.95}$ being the most commonly employed one [20]. Gd^{3+} doped CeO_2 (GDC), for example, shows remarkable ionic conductivity of around 0.025 S/cm at 600°C [20]. CeO_2 may be doped by different cations such as Gd, Sm, Nd, La, Sm, Y and Yb [21]. Among them, Gd^{3+} has the lowest ionic radius mismatch; and this leads to enhanced transport properties [20]. Defect reactions by Gd^{3+} doping to CeO_2 is shown with Kröger-Vink notation in Equation 1.6 [12].



$\text{Ce}_{0.9}\text{Gd}_{0.1}\text{O}_{1.95}$ (GDC) is a popular electrolyte material due to its promising ionic conductivity and compatibility with LSCF cathodes. Therefore; this material is chosen as the electrolyte material in this thesis.

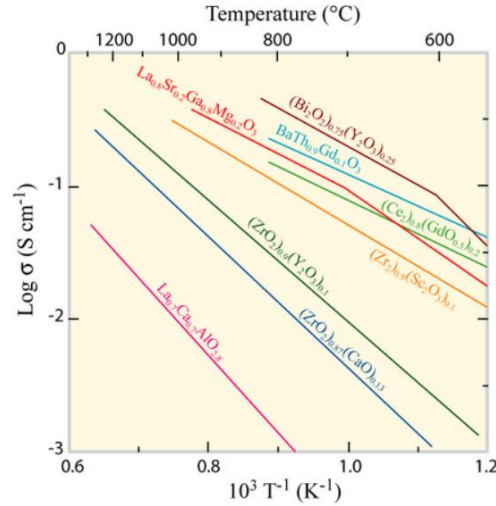


Figure 1.5. Comparison of ionic conductivity of various electrolyte candidates. (Source: Singhal et. al., 2015)

1.5.2. The Anode

An SOFC anode (fuel electrode) usually is the thickest layer and is porous to provide high surface area for reaction of fuel with oxygen. This layer should have high electrical conductivity and sufficient stability in reducing atmospheres. Anode, electrolyte and interconnect layers must be compatible in their thermal expansion characteristics [22]. Anode side is usually a porous cermet consisting of ceramic and metallic phases. Metallic phase provides electronic conductivity and the ceramic phase ensures sufficient ionic conductivity [22]. The relative nickel content determines the type of conductivity that will predominate. A percolation occurs around 30% nickel addition which is critical for the type of conductivity. Above the threshold of 30%, cermet becomes an electronic conductor and below this threshold percentage, cermet possesses ionic conductivity [23-24].

Ni/YSZ cermet is one of the most popular SOFC anode materials. Ni is an excellent hydrogen oxidation catalyst. Also, the CTE values of Ni and YSZ are close to each other [4]. In recent years, ceria-based electrolytes replaced YSZ, and thus Ni-GDC cermet gained attention. Moreover, the ability to suppress carbon deposition is higher in

Ni-GDC cermet than in Ni-YSZ. This ability allows the use of hydrocarbon fuels as fuel in SOFC. However, rapid grain growth of Ni particles brings about agglomeration and oxidation around GDC and YSZ particles, which eventually lead to performance degradation [24-25] upon sintering at elevated temperatures. A potential solution to this drawback is proposed in Chapters 3 and 4.

1.5.3. The Cathode

The cathode (a.k.a air electrode) is the electrode where oxygen reduction reaction (ORR) occurs which requires high catalytic activity. Besides, the cathode material should be constantly supplied with electrons through an external circuit making it necessary to have high electronic conductivity (>100 S/cm) [21,26]. Porosities between 25 and 40% are required to allow gas transport through cathode to the interface of cathode/electrolyte [20]. Besides, ionic conductivity value of cathode must be high to ensure transport of oxygen ions obtained after ORR [20]. Thermal expansion coefficients (CTE) of the cathode, electrolyte and interconnect should match. Finally, it should be chemically stable [27].

Perovskite-type materials with general formula, ABO_3 are the most suitable material for the cathode layer. A typical representation of ABO_3 type is shown in Figure 1.6. The larger A-site (e.g. La, Sr, Pb, Ca, etc.) and the smaller B-site cations (e.g. Co, Fe, Cr, Zr, Ti, etc.) make up the structure [20,28].

Strontium doped lanthanum manganate ($La_{1-x}Sr_xMnO_{3-d}$, also known as LSM) is one of the most common cathode materials because of their compatibility with YSZ [20]. $CTE_{LSM}=12.4 \times 10^{-6} K^{-1}$ is match with $CTE_{YSZ}=10.5 \times 10^{-6} K^{-1}$. Besides, LSM has high electronic conductivity (120 S/cm at 800°C). However, ionic conductivity of LSM is dramatically low as $4 \cdot 10^{-8}$ S/cm at 800°C [29]. Therefore, LSM is a pure electronic conductor ($\sigma_e \gg \sigma_i$) and ORR can only occur at triple phase boundaries (TPB) where cathode (α), electrolyte (γ) and gas phase (β) meet (Figure 1.7a). ORR occurs only at TPB and porosity in LSM is critical for oxygen transportation [4]. Besides, at elevated temperatures as 1200 °C, YSZ and LSM undergo a reaction and form undesirable phases like $La_2Zr_2O_7$ (LZ) [31].

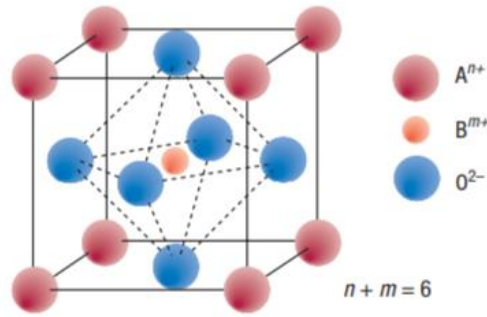


Figure 1.6. A typical ABO_3 perovskite unit cell.
(Source: Boukamp, 2008)

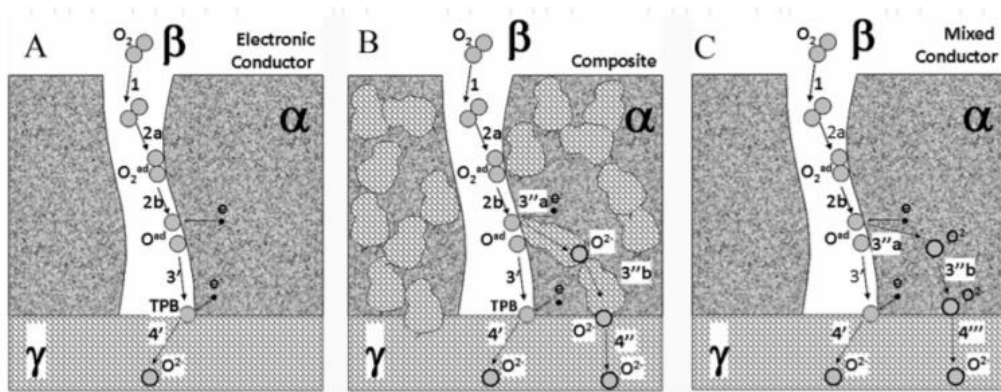


Figure 1.7. Oxygen reduction reaction (ORR) steps in (a) pure electronic conductor, (b) electronic and ionic composite conductor and (c) mixed ionic-electronic conductor (MIEC).
(Source: Soldati et. al., 2012)

Some strategies were used to enhance the cathodic performance of LSM such as i) increasing its porosity to improve oxygen diffusion and ii) decreasing grain size to nanoscale for extending the cathode surface area [30]. Another attempt to improve SOFC performance is to enlarge the TPB area by formation of composites such as LSM-YSZ or LSM-GDC combinations. Oxygen pathway is extended by the addition of ionic conductor phase (Figure 1.7b) [30,32-33].

LSM is a great candidate for cathodes in the range of 800-1000°C. However, reduction of operating temperature to e.g. 700 °C leads to a dramatic decrease in cathode performance due to low ionic conductivity values. Hence, new materials are required to be used in IT-SOFC temperature ranges [34]. Mixed Ionic-Electronic Conductors (MIEC) became state-of-the-art materials due to their ability to conduct both oxygen ions and electrons [20]. A-site rare-earth cations influence the ionic conductivity and B-site transition metals mostly influence the electronic conductivity. In this type of materials, ORR occurs at entire cathode surface that meets with oxygen gas and O^{2-} ions so formed

can travel inside the bulk (Figure 1.7c) [30,34,35]. Ergo, the requirement of TPBs are bypassed since MIEC materials replaced pure electronic conductor materials. LSCF is one of the most popular MIEC material. Polarization resistance of LSCF is much lower than LSM and CTE compatibility with GDC matches well ($CTE_{LSCF}=12.8 \times 10^{-6} \text{ K}^{-1}$, $CTE_{GDC}=17 \times 10^{-6} \text{ K}^{-1}$) [34,35]. For these reasons, LSCF and mixture of LSCF-GDC are chosen as cathode materials in this dissertation.

1.6. Research Scope

The most compelling reason that SOFCs are not fully commercialized yet is their high operating temperature of 800-1000°C which forbids long term robust operation. Therefore, reduction of this temperature, being one of the most hectic research topics in fuel cells field, helps save on the necessity of using expensive materials especially in interconnect and sealing parts. For example, LaCrO_3 , which is an expensive ceramic interconnect material, can be replaced by its low-cost counterparts upon drop off of the operating temperature [5,34]. Moreover, high operating temperature causes longer heat-up and shut down durations to avoid thermal shock [33,34]. However, there is price paid for reductions in temperature, such as slower ORR, sluggish diffusion of oxygen ions as well as poor electrochemical performance. Therefore, entirely new set of materials was necessary to compensate for the loss of performance due to reduced temperature. Therefore new electrolyte, cathode and anode materials with satisfactory performances emerged in literature [34]. GDC, for example, with its remarkable ionic conductivity is the most recently used electrolyte material which is chosen in this dissertation as the principle electrolyte material. Similarly, the new cathode layer material of choice is a mixed oxide LSCF which shows MIC character as well. Therefore, we chose LSCF as the cathode material in this study. The focus of attention in the thesis was optimizing the electrochemical performances of GDC-LSCF type of cells with little emphasis on the anode layer. Bieberle et al., [36] determined that the total resistance of the cell is dominated by cathode and electrolyte layers. Hence, this dissertation is focused on the improvement of cathode and electrolyte layers by tailoring the microstructures. Polymeric precursor solution technique which is already used in anode layers [37] is adopted in this work to control the microstructure in nanoscale. Even though LSCF and GDC are recently

known to be the best candidates for cathode and electrolyte layers, respectively, for IT-SOFCs, there is still room for improvement in performance.

Four different approaches are developed in this dissertation. These are briefly explained in the following paragraphs each of which constitutes a separate Chapter in the thesis. These Chapters 2 to 5 are all either separately published or submitted for publication in refereed international journals. Publication of these papers is imminent. Therefore the papers are directly copied from these articles and pasted into this dissertation as separate chapters.

The performance of solid oxide fuel cells (SOFCs) is often limited by the slow kinetics of the oxygen reduction reaction (ORR) and diffusion of reduced O^{2-} ion through the cathode. One of the most effective strategies is to solve this problem by using thin films of cathodes to reduce the diffusion distances [34,38]. Thin film based components can be used in micro-scale SOFC, also known as μ -SOFC [38]. μ -SOFCs can be operated at lower temperatures by employing thin electrolyte layers. While the thickness of a conventional SOFC cell is around 1 mm, the thickness of a μ -SOFC cell is only 1 μ m due to the deposition of thin film layers. Besides μ -SOFCs are more stable than conventional SOFCs because of their lower operating temperatures of 400-800°C [39]. As shown in Figure 1.7, LSCF cathode layers and LSCF-GDC nanocomposite cathode layers are coated on GDC electrolyte by spin coating in Chapter 2. Thin film cathodes are investigated microstructural and electrochemically. Also, long term stability tests are done and discussed. This chapter is submitted in Ionics [39]

Chapters 2 and 3 are related to the cathode layers which are derived from polymeric precursor solutions of single phase LSCF and nanocomposite of LSCF-GDC mixtures. Despite LSCF is one of the most state-of-the-art mixed ionic and electronic conductor (MIEC), its conductivity drops sharply upon temperature reduction. Therefore, preparation of mixture with electrolyte material, a well-known strategy for LSM-YSZ composite cathode [36-40], is proposed for LSCF and GDC couple in these chapters. The main idea is to enlarge the active sites by extending the electrolyte through the whole thickness of the LSCF layer. Moreover, the activation energy (E_a) for oxygen diffusion in LSCF is 176 kJ/mol [40] while that for GDC is 87 kJ/mol [40,41]. Thus, a composite of LSCF and GDC coated as a thin film on dense GDC as a cathode for SOFCs is studied in this thesis. Thus, LSCF and LSCF-GDC are compared in this study as cathode materials to see how they would behave when coated as films on electrolytes to solve the

resistance problem due to lowered operating temperature. Theoretical pathways of oxygen ions through single phase LSCF cathode and LSCF-GDC nanocomposite cathode are shown in related chapters.

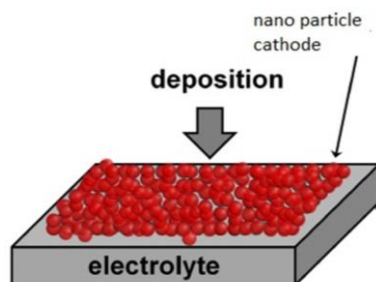


Figure 1.8. LSCF and LSCF-GDC nanocomposite deposition on dense GDC electrolyte by spin coating

In Chapter 3, infiltration, which is another facile technique for the formation of the electrode is studied. A porous GDC thick film deposited by tape casting on dense thick GDC electrolyte is infiltrated by LSCF and LSCF-GDC nanocomposite solution (Figure 1.9). Infiltration with perovskite/ceria combination, specifically lanthanum cobaltite-based perovskite/doped ceria combination [41] produces cathodes with relatively lower area specific resistances (ASR). The fastest pathway for oxygen determines the overall kinetics of the reaction. Aim of this study is to extend the electrochemical reaction zone for fast oxygen transportation by extending the area from cathode/electrolyte interface to the whole cathode layer and hence modifying the oxygen transport pathway. As infiltration is a multi-step process, an optimization work needs to be performed to find the optimal loading number. Electrochemical properties and long-term stabilities of the infiltrated symmetrical cells are also investigated. This chapter is published in Journal of Sol-Gel Science and Technology [43]

Chapters 4 and 5 are related with the electrolyte layers. SOFC electrolytes need to be fully dense to prevent gas leakage. However, the conventional atmospheric sintering temperature of GDC is relatively high above 1400°C. This much of elevated sintering temperature brings about problems related with unstable valance state of cerium (from Ce^{4+} to Ce^{3+}) not to mention the associated cost of heating [2,21,42]. The most significant drawback of high sintering temperature of GDC manifests itself co-sintered in contact with the anode layer. The latter prematurely coarsens while the former is still porous [2,42]. Therefore, the sintering temperature of GDC needs to be lowered, and Chapter 4 is focused on this issue. Infiltration of polymeric precursor solutions is employed in Chapters 4-5 just as it was in Chapter 3. Precursor solution of GDC is infiltrated into the

previously sintered GDC scaffold to fill the pores by the same material which enhances densification during sintering (Figure 1.9). Chapter 5 presents the electrochemical characterization of densified GDC with the assistance of infiltration. The purpose was to check its suitability for use in potential SOFC processes. Chapter 4 and 5 are published in Journal of the European Ceramic Society and Solid State Ionics, respectively. [45,46]

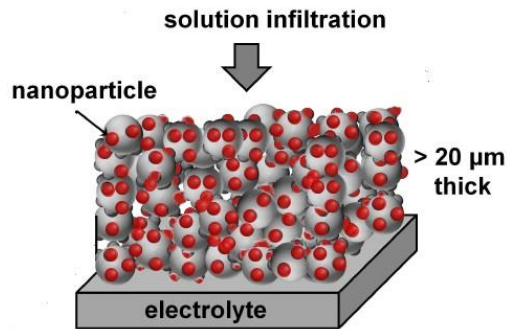


Figure 1.9. Infiltration of LSCF and LSCF-GDC nanoparticles inside of porous thick GDC scaffold on dense GDC electrolyte symmetrically.

1.7. References

- [1] Stambouli, A.; Traversa, E. *Renewable and Sustainable Energy Reviews* **2002**, *6*(5), 433–455.
- [2] Minh, N. Q.; Takahashi, T. *Science and Technology of Ceramic Fuel Cells* **1995**, 165–198.
- [3] Hoogers, G. *Fuel cell technology handbook*; CRC Press: Boca Raton, FL, **2003**.
- [4] Singhal, S.; Kendall, K.; Kendall, M. *High-Temperature Solid Oxide Fuel Cells Fundamentals, Design and Applications*; Elsevier Science & Technology: Saint Louis, **2015**.
- [5] Jain, B.; Jain, S.; Nema, R. *Renewable and Sustainable Energy Reviews* **2015**, *47*, 983–996.
- [6] Andújar, J.; Segura, F. *Renewable and Sustainable Energy Reviews* **2009**, *13* (9), 2309–2322.
- [7] Huang, Y. H.; Dass, R. I.; Xing, Z. L.; Goodenough, J. B. *Science*, **2006**, *312*, 254-257.
- [8] Huijsmans, J.; Berkel, F. V.; Christie, G. *Journal of Power Sources* **1998**, *71*(1-2), 107– 110.

- [9] Office of Energy Efficiency & Renewable Energy. <https://www.energy.gov/eere/office-energy-efficiency-renewable-energy> (accessed May 29, 2019).
- [10] Bauen, A.; Hart, D. *Journal of Power Sources* **2000**, 86 (1-2), 482–494.
- [11] Weaver. *World Fuel Cells* **2002**, 81–96.
- [12] Minh, N.Q., "Ceramic Fuel Cells," *Journal of the American Ceramic Society*, vol. 76, pp. 563-588, 1993.
- [13] Bowman W., Sharma, R, Crozier, P.A, *Microscopy and Microanalysis Proceedings* **2013**
- [14] Revankar, S.; Majumdar, P. *Fuel cells: principles, design, and analysis*; CRC Press, Taylor & Francis Group: Boca Raton, 2014.
- [15] Huang, K.; Goodenough, J. B. *Solid Oxide Fuel Cell Technology* **2009**, 67–84.
- [16] Haile, S. M. *Acta Materialia* **2003**, 51 (19), 5981–6000.
- [17] Huang, P.-N.; Petric, A. *Journal of The Electrochemical Society* **1996**, 143 (5), 1644.
- [18] Jacobson, A. J. *Chemistry of Materials* **2010**, 22 (3), 660–674.
- [19] Jiang N.X., Wachsman E.D.; Jung S.H.A.; *Solid State Ionics*, 2002, 150 (3-4), 347-353.
- [20] Marinha, D.; Dessemond, L.; Djurado, E. *Current Inorganic Chemistry* **2013**, 3 (1), 2–22.
- [21] Steele, B.C.H.; *Solid State Ionics* **2000**, 129, 95-110.
- [22] Vohs, J. M.; Gorte, R. J. *Advanced Materials* **2009**, 21(9), 943–956.
- [23] Sun, C.; Stimming, U. *Journal of Power Sources* **2007**, 171 (2), 247–260.
- [24] Zhu, W.; Deevi, S. *Materials Science and Engineering: A* **2003**, 362 (1-2), 228–239.
- [25] Young, J.; Birss, V. *Journal of Power Sources* **2011**, 196 (17), 7126–7135.
- [26] Haberko, K.; Jasinski, M.; Pasierb, P.; Radecka, M.; Rekas, M. *Journal of Power Sources* **2010**, 195(17), 5527–5533.
- [27] Fabbri, E.; Pergolesi, D.; Traversa, E. *Chemical Society Reviews* **2010**, 39 (11), 4355.
- [28] Boukamp, B. A. *Nature Materials* **2003**, 2 (5), 294–296.

- [29] Ji, Y.; Kilner, J.; Carolan, M. *Solid State Ionics* **2005**, *176* (9-10), 937–943.
- [30] Soldati, A. L.; Baqué, L.C; Troiani, H.E.; Serquis, A.C.; Hydrogen Energy - Challenges and Perspectives, **2012**
- [31] Clausen, C.; Bagger, C.; Bildesorensen, J.; Horsewell, A. *Solid State Ionics* **1994**, *70-71*, 59–64.
- [32] Jørgensen, M.; Primdahl, S.; Bagger, C.; Mogensen, M. *Solid State Ionics* **2001**, *139*(1-2), 1–11.
- [33] Elangovan, S.; Hartvigsen, J.; Khandkar, A.; Privette, R.; Kneidel, K.; Perna, M.; Rowley, D. *Journal of Power Sources* **1998**, *71* (1-2), 354–360.
- [34] Tarancón, A. *Energies* **2009**, *2* (4), 1130–1150.
- [35] Adler, S. B. *Chemical Reviews* **2004**, *104* (10), 4791–4844.
- [36] Bieberle-Hütter, A.; Beckel, D.; Infortuna, A.; Muecke, U. P.; Rupp, J. L.; Gauckler, L. J.; Rey-Mermet, S.; Mural, P.; Bieri, N. R.; Hotz, N.; Stutz, M. J.; Poulikakos, D.; Heeb, P.; Müller, P.; Bernard, A.; Gmür, R.; Hocker, T. *Journal of Power Sources* **2008**, *177* (1), 123–130.
- [37] Buyukaksoy, A.; Kammampata, S. P.; Birss, V. I. *Journal of Power Sources* **2015**, *287*, 349–358.
- [38] Beckel, D.; Bieberle-Hutter, A.; Harvey, A.; Infortuna, A.; Muecke U.P.; Prestat, M.; Rupp, J.L.M.; Gauckler, L.J.; *Journal of Power Sources*, 2007, *173*, 325–345.
- [39] Sındıraç, C.; Ahsen A., Öztürk, O; Akkurt, S.; Birss, V.I; Büyükaksoy, A.; *Submitted to Ionics*
- [40] Barnett, S. *Energy* **1990**, *15* (1), 1–9.
- [41] Murray, E. P.; Barnett, S. A. *Solid State Ionics* **2001**, *143* (3-4), 265–273.
- [42] Dusastre, V.; Kilner, J. *Solid State Ionics* **1999**, *126* (1-2), 163–174.
- [43] Sındıraç, C.; Büyükaksoy, A.; Akkurt, S. *Journal of Sol-Gel Science and Technology* **2019**
- [44] Shah, M.; Barnett, S. *Solid State Ionics* **2008**, *179*(35-36), 2059–2064.
- [45] Sındıraç, C.; Çakırlar, S.; Büyükaksoy, A.; Akkurt, S. *Journal of the European Ceramic Society* **2019**, *39*(2-3), 409–417.
- [46] Sındıraç, C.; Büyükaksoy, A.; Akkurt, S. *Solid State Ionics* **2019**, *340*, 115020.

CHAPTER 2

FABRICATION OF LSCF AND LSCF-GDC NANOCOMPOSITE THIN FILMS USING POLYMERIC PRECURSORS

Can Sındıraç¹, Ali Ahsen^{2,3}, Osman Öztürk^{2,3}, Sedat Akkurt¹, Viola I. Birss⁴, and Aligül Büyükaksoy^{4,5*}

¹ Izmir Institute of Technology, Department of Mechanical Engineering, Urla, İzmir, 35433 Turkey

²Gebze Technical University, Department of Physics, Gebze, Kocaeli 41400, Turkey

³Gebze Technical University, Institute of Nanotechnology, Gebze, Kocaeli 41400, Turkey

⁴ University of Calgary, Department of Chemistry, Calgary, Alberta T2N 1N4, Canada

⁵ Gebze Technical University, Department of Materials Science and Engineering, Gebze, Kocaeli 41400, Turkey

*Corresponding Author:

E-mail: aligul@gtu.edu.tr, Ph: +90 (262) 605-2662

This chapter is submitted to Ionics

2.1. Abstract

The mixed ionic-electronic conductor, $\text{La}_{1-x}\text{Sr}_x\text{Co}_y\text{Fe}_{1-y}\text{O}_3$ (LSCF), is widely used as an oxygen reduction electrocatalyst in solid oxide fuel cell (SOFC) cathodes. A compatible ionic conductor, usually gadolinia doped ceria (GDC), is sometimes mixed with LSCF to introduce a faster ion conducting phase to the electrode layer and thus improve the electrochemical activity. To further increase the electrochemical activity, the electrocatalyst/ionic conductor interfacial area can be maximized by nanostructuring the LSCF-GDC composite. In the present study, we fabricated both single phase LSCF and composite LSCF-GDC thin film electrodes using a facile and cost effective polymeric precursor technique. This method involves the molecular level mixing of cations in solution form and results in average particle sizes of ca. 72 nm and 60 nm upon annealing at relatively low temperatures of 700°C, respectively. For LSCF, electrochemical impedance spectroscopy measurements indicate very low electrode polarization resistances of ca. 0.6 $\Omega\cdot\text{cm}^2$ per electrode at 600 °C. However, the addition of GDC results

in poorer electrochemical activity but better microstructural and electrochemical stability, all at 600 °C. Surface analysis revealed that Fe surface-segregation occurs in the single phase LSCF, while predominantly Co segregation is observed at the LSCF-GDC composite electrode surface.

Keywords: Solid oxide fuel cell, thin film electrodes, impedance spectroscopy, long-term stability, surface segregation

2.2. Introduction

The limited long-term performance and stability of solid oxide fuel cells (SOFCs) at their conventional operating temperatures of 700-800 °C hinders their viability as a viable energy conversion technology. Thus, the goal is to reduce the operating temperatures of these devices down to below 650 °C in order to avoid microstructural and chemical degradation of their components, such as microstructural coarsening in the electrodes [1,2], surface segregation in the perovskite cathode electrocatalyst [2,3] and oxidation of the stainless steel interconnects [4,5].

Since oxygen reduction, fuel oxidation, and ionic transport processes that occur at the cathode, anode and electrolyte materials, respectively, are all thermally activated processes, a decrease of the operating temperatures brings about a loss in the overall cell performance. It is now well-established that, at temperatures below 650°C, oxygen reduction at the cathode is the main contributor to the total cell resistance [6-8]. Therefore, efforts to lower the SOFC operating temperature has largely concentrated on the development of cathodes that would exhibit acceptable performance at these lowered temperatures [9-13].

The majority of the studies aiming at the development of such cathodes have been based on enhancing the electrocatalyst/gas and electrocatalyst/ionic conductor interfacial areas while using perovskite oxygen reduction electrocatalysts with mixed ionic electronic conductivity (MIEC), such as $\text{La}_{1-x}\text{Sr}_x\text{Co}_y\text{Fe}_{1-y}\text{O}_3$ (LSCF) [2,6,8,11]. For this purpose, LSCF has been fabricated both as a porous, single phase layer and in the form of a composite mixed with a chemically compatible ionic conductor, e.g., gadolinia doped ceria (GDC) [8,13].

The most straightforward approach to producing LSCF and LSCF-GDC cathodes with high electrochemical activity at ≤ 650 °C has been to sinter suspensions containing fine powders of the corresponding phases at 850-1150 °C [14-19]. This powder-based fabrication method, in general, yielded 5-60 μm -thick cathode layers, characterized by microstructures with average particle sizes in the 0.7-3 μm range [14,15]. In general, sufficiently high electrochemical activities for low-temperature operation have been achieved in the case of LSCF-GDC composites prepared by the powder-based method, while relatively poor performances were observed in the case of single phase LSCF prepared by the same route [14,15,18]. For example, Murray et al reported a polarization resistance of $0.17 \Omega\cdot\text{cm}^2$ at 600 °C for LSCF-GDC composite cathodes, indicating a high electrochemical activity, while obtaining $2 \Omega\cdot\text{cm}^2$ at the same temperature in single phase LSCF cathodes [14]. Similarly, Dusastre et al. also reported a decrease in the polarization resistance of powder derived LSCF cathodes from 4 to $0.6 \Omega\cdot\text{cm}^2$ at 590 °C upon mixing with GDC [15].

To further enhance the LSCF/gas and LSCF/ceria interfacial area and thus facilitate oxygen adsorption and oxide ion transfer, respectively, infiltration of liquid solutions containing the cations of LSCF into previously formed porous ceria scaffolds has been studied [13,20-25]. Upon heating the solution infiltrated porous ceria scaffold, nanoparticles of LSCF form, yielding porous LSCF-ceria composites with enhanced LSCF/air and LSCF/ceria interfacial areas [21,26,27]. Burye et al reported that LSCF-GDC composites, prepared by LSCF infiltration into porous GDC scaffolds, had a microstructure consisting of LSCF particles that were ca. 48 nm in diameter with a very low a polarization resistance of $0.2 \Omega\cdot\text{cm}^2$ at 600 °C [26]. Nie et al., reversed the process, i.e., infiltrated samaria doped ceria (SDC) into porous LSCF scaffolds, thus lowering the polarization resistance from $1.09 \Omega\cdot\text{cm}^2$ to $0.44 \Omega\cdot\text{cm}^2$ at 600 °C [28].

The very low polarization resistances of LSCF-GDC cathodes prepared by powder sintering and infiltration methods, obtained at ≤ 650 °C, are only meaningful when they are employed in an SOFC design that, as a whole, is designed to exhibit acceptable performances at these temperatures. SOFCs consisting of thin film electrodes and electrolytes with total thicknesses of only a few microns, i.e., micro-SOFCs, are designs that ensure short oxide ion diffusion distances both in the electrolyte and the electrodes, thus decreasing the ohmic resistances to a minimum [2,3,19,29-31]. However, powder sintering and infiltration derived LSCF-GDC cathodes are not suitable for use in micro-SOFCs, due to the high heat treatment temperatures (850-1000 °C) required in at

least one of their processing steps [8]. Cathode layers in the form of thin films, on the other hand, can be fabricated by pulsed laser deposition (PLD) [32], radio frequency (RF) magnetron sputtering [33], spray pyrolysis [34,35] and electrostatic spray deposition (ESD) methods [36-38]. Among these studies, high polarization resistances of $8 \Omega \cdot \text{cm}^2$ at $750 \text{ }^\circ\text{C}$ and $122 \Omega \cdot \text{cm}^2$ at $600 \text{ }^\circ\text{C}$ were obtained in LSCF thin film cathodes prepared by PLD [32] and RF-magnetron sputtering [33], respectively. The main reason behind these large polarization resistances is that PLD and RF magnetron sputtering derived LSCF thin films are usually dense and thus more suitable for use in mechanistic studies as model electrodes [32,33]. In addition, the high equipment costs associated with the PLD and RF magnetron sputtering methods are undesirable for SOFC fabrication purposes [32-33,39-40].

Spray pyrolysis and ESD, on the other hand, have yielded LSCF and LSCF-GDC thin film cathodes with nanoporous microstructures and thus lower polarization resistances [34-36]. Polarization resistances as low as $1 \Omega \cdot \text{cm}^2$ at $575 \text{ }^\circ\text{C}$ were obtained for spray pyrolysis derived LSCF-GDC thin films [35], while the ESD process resulted in even lower polarization resistances of $0.13 \Omega \cdot \text{cm}^2$ at $600 \text{ }^\circ\text{C}$ [36].

In this work, as an alternative to the previously discussed methods, our goal was to fabricate single-phase LSCF and LSCF-GDC composite thin film cathodes for SOFCs operating at $\leq 650 \text{ }^\circ\text{C}$ by a facile and cost effective polymeric precursor method. Our recent efforts showed that nanoscale Ni-YSZ composite anodes fabricated by this method yielded very low polarization resistances ($0.6 \Omega \cdot \text{cm}^2$ at $550 \text{ }^\circ\text{C}$), and thus a similar positive effect on the performance of the cathode was anticipated [30]. In this approach, polymeric precursors deposited onto dense GDC substrates by simple spin-on deposition undergo gelation instead of precipitation upon heat treatment, which results in good attachment to the substrate without the need for high temperature annealing. In addition, this approach yields nanoscale composites as a result of the molecular level mixing, low-temperature annealing and concurrent formation of the LSCF and GDC phases in the case of LSCF-GDC thin films.

2.3. Experimental Methods

Experimental method is explained in this section

2.3.1. Fabrication of Electrolyte Substrates

10 mol % gadolinium-doped ceria powder ($\text{Ce}_{0.9}\text{Gd}_{0.1}\text{O}_3$ (GDC), PRAXAIR >99.9%) was used for the preparation of the dense ceramic electrolyte discs. The specific surface area of the powder was $6.6 \text{ m}^2/\text{g}$, while the d_{10} , d_{50} and d_{95} values were $0.4 \mu\text{m}$, $0.6 \mu\text{m}$ and $0.9 \mu\text{m}$, respectively. The powder was compacted at 180 MPa pressure by uniaxial pressing (Carver Hydraulic Press, Wabash, IN, USA) in a cylindrical stainless steel die, producing pellets 15 mm in diameter and 1 mm thick. The pellets were then fired to densify in an electrically heated laboratory kiln (Nabertherm LHT 02/17, Germany) at $1400 \text{ }^\circ\text{C}$ for 4 hours at a heating rate of $3 \text{ }^\circ\text{C}/\text{min}$.

2.3.2. Fabrication of Electrolyte Substrates

To deposit the LSCF thin films on the GDC electrolytes, a polymeric precursor solution that contained the stoichiometric amounts of the constituent cations was prepared. Lanthanum (III) nitrate hexahydrate (ALFA-AESAR >99.99%), strontium chloride hexahydrate (ALFA-AESAR >99%), cobalt (II) nitrate hexahydrate (ALFA-AESAR >97.7% min), and iron (III) nitrate nonahydrate (ALFA-AESAR >99.99%) salts were dissolved in deionized water at a molar ratio that would produce the desired $\text{La}_{0.6}\text{Sr}_{0.4}\text{Co}_{0.8}\text{Fe}_{0.2}\text{O}_{3-\delta}$ (LSCF) stoichiometry. In the second step, the salt solution was mixed with ethylene glycol (ethylene glycol:cation molar ratio of 1:0.04) and stirred at $70 \text{ }^\circ\text{C}$ until all of the water had evaporated and polymerization took place. To lower the surface tension of the polymeric LSCF precursor and ensure good wetting of the GDC substrate upon deposition, the solution was diluted with 2-butoxyethanol (1:1 weight ratio).

For the preparation of the LSCF-GDC composite thin films, a polymeric precursor of GDC was prepared in a similar way, i.e., by adding ethylene glycol to an aqueous solution of $\text{Gd}(\text{NO}_3)_3 \cdot 6\text{H}_2\text{O}$ (Sigma-Aldrich >99.9%) and $\text{Ce}(\text{NO}_3)_3 \cdot 6\text{H}_2\text{O}$ (ALFA-AESAR >99.5%) salts and stirring at $70 \text{ }^\circ\text{C}$ until all of the water had evaporated and polymerization took place. Then, the polymeric precursors of LSCF and GDC were mixed in appropriate ratios to yield a volumetric LSCF:GDC ratio of 60:40. 2-butoxyethanol

was again added to the resultant solution to achieve good wetting of the GDC substrate upon deposition. Further details of the process are given elsewhere [30, 41, 42].

To produce the LSCF and LSCF-GDC thin films on the GDC electrolytes, the polymeric LSCF and LSCF-GDC precursors were deposited onto the 1 mm thick GDC substrates by spin coating at a rotation speed of 3000 rpm (SCS G3 Spin Coater, Indianapolis, USA). The samples were then placed on a hot plate and gradually heated to 400 °C until the solvents had evaporated and the other organic constituents had decomposed, producing uniform LSCF or LSCF-GDC layers. The spin coating/decomposition cycles were repeated 30 times in order to obtain a thin film approximately 1 μm thick on the dense GDC substrates. This coating process was applied on both sides of the GDC pellets to prepare symmetrical half-cells for electrochemical characterization. GDC pellets successfully coated with LSCF or LSCF-GDC were then annealed in air at 400-700 °C for various times for microstructural and structural characterization.

Figure 2.1 shows the temperature profile used during the EIS characterization of the thin film electrodes. This heating/cooling protocol is divided into five stages (I-V) in order to clearly describe the thermal history of the symmetrical cells at the time of the EIS measurements.

2.3.3. Structural and Microstructural Characterization

The ability of the polymeric precursor method to form the LSCF and LSCF-GDC thin films with the desired crystal structures was determined by x-ray diffraction (XRD, Panalytical X-Pert Pro). The grazing incidence mode at an angle of $\theta = 1^\circ$ was utilized to obtain more signal from the thin films and less from the GDC substrate. Cu K α radiation was selected as the x-ray source.

The microstructure and thickness of the LSCF and LSCF-GDC thin films were determined by Scanning Electron Microscopy (SEM, Philips XL 30S FEG) utilizing secondary electron (SE) imaging. More detailed microstructural/morphological analysis was carried out by Atomic Force Microscopy (AFM, Digital Instruments-MMSPM Nanoscope IV) using the non-contact mode.

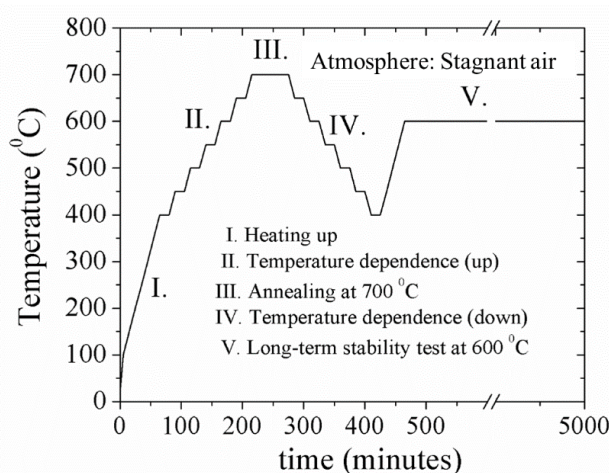


Figure 2.1. Graph showing the durations for which the LSCF and LSCF-GDC electrodes were exposed to each temperature

2.3.4. Electrochemical Performance Analysis

Symmetrical half-cells were prepared for electrochemical performance analysis. Au paste (Electroscience, King of Prussia, PA) was applied on top of the electrodes as the current collectors, which were contacted to Au wires connected to a Solatron ECS Modulab electrochemical analysis instrument. The electrochemical performance of the thin film electrodes was determined by electrochemical impedance spectroscopy measurements performed at 400-700 °C, in stagnant air, using an AC excitation voltage of 20 mV. ZView software was employed to perform the fitting of the impedance data.

2.3.5. Surface Analysis

To determine the elemental composition of the surface of the LSCF and LSCF-GDC thin film electrodes, x-ray photoelectron spectroscopy (XPS) analyses were carried out. The analysis chamber had a base pressure of 1×10^{-10} mbar and was equipped with a conventional X-ray source (Al-K α) and Phoibos 150 Specs charged particle analyzer. The survey scan of all samples showed that each sample contained only La, Sr, Co, Fe, C and O on the surface. In addition, the LSCF-GDC sample contained Ce and Gd. The elemental ratios of La, Sr, Co and Fe were calculated after a detailed scan of the main peak for each element. The background signal was subtracted using a six-degree

polynomial background function, while the La 3d, Sr 3d, Co 2p and Fe 2p peaks were fitted with a Voight function.

2.4. Results and Discussions

Results are provided in this section.

2.4.1. Phase Analysis

In order to determine the crystal structure of the coatings, thin film X-ray diffraction (XRD) studies were carried out. Glancing angle XRD patterns of the LSCF and LSCF-GDC films that were annealed either at 500 °C or at 700 °C for 2 hours in air are shown in Figure 2.2. A major disadvantage of the XRD analysis of LSCF thin films deposited on GDC electrolytes is that the peaks belonging to the rhombohedral LSCF (PDF:00-049-0283) and the cubic GDC (PDF:01-075-0161) overlap at $2\theta = 33^\circ, 48^\circ, 58^\circ, 69^\circ$ and 78° . Only the low-intensity peaks of rhombohedral LSCF at $2\theta = 23^\circ, 40.7^\circ$ do not overlap with those of cubic GDC. The fact that these peaks are present in the XRD patterns of the LSCF peaks annealed at 500 and 700 °C suggests that rhombohedral LSCF is present.

The XRD patterns obtained for the LSCF thin film annealed at 500 °C show small amounts of residual phase peaks, identified as SrCO_3 and an unidentified peak at 36° . The presence of SrCO_3 during the phase evolution of LSCF has also been observed by other research groups [19, 43-46]. The peaks belonging to SrCO_3 are observed to disappear upon annealing at 700 °C, eventually resulting in the development of the pattern for only LSCF and GDC phases, but with only one unidentified peak remaining (Figure 2.2).

The challenges associated with the overlap of the LSCF and GDC peaks are seen again and in an even more pronounced fashion in the case of LSCF-GDC composite thin films annealed at 500 and 700 °C in air (Figure 2.2). This is because the LSCF content is now lower, being 60 vol% within the thin film, as opposed to the single phase LSCF (100 vol% LSCF content), lowering the intensities of the $2\theta = 23^\circ$ and 40.7° peaks even further down to below the detection limit of the XRD. Angoua et al. also prepared LSCF-

GDC thin films, but using spray pyrolysis of the aqueous solutions on GDC electrolytes, and reported that distinct LSCF peaks can only be seen upon heat treatment at temperatures above 800 °C [47]. They also reported that LSCF was detectable as a shoulder on the GDC peaks at $2\theta = 47^\circ$ upon annealing. The same shoulders are also observed in the present case of the LSCF-GDC thin films annealed at 700 °C (Figure 2.2), suggesting the presence of the rhombohedral perovskite phase.

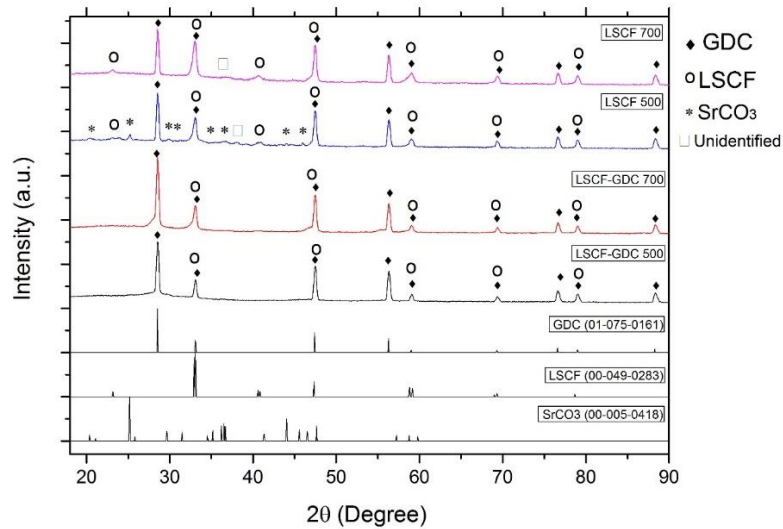


Figure 2.2. Thin film x-ray diffraction patterns of LSCF and LSCF-GDC, heat treated in air 500°C or 700°C

2.4.2. Microstructural Analysis

Electrode material coated electrolyte discs were fractured down the middle to examine the cross-sections and determine coating thickness, uniformity, porosity, the presence of cracks, and the degree of bonding to the substrate, using Scanning Electron Microscopy (SEM). A representative SEM image of the LSCF-GDC nanocomposite coating, annealed at 700 °C, is shown in Figure 2.3. A uniform film, adhering well to the dense substrate and with an approximate thickness of 2 μm , is observed. Some unexpectedly large pores, possibly related to the fast evaporation of organics, are also evident.

In order to determine the grain size and the presence of small pores, a more detailed microstructural study was performed using non-contact mode atomic force microscopy (AFM). Figure 2.4a-c shows the AFM images of LSCF thin films annealed at 500 °C for 2 hours (Stage II in Figure 2.1), 700 °C for 2 hours (Stage III in Figure 2.1),

and 500 °C then 600 °C for another 100 hours (Stage V in Figure 2.1). A uniform grain size of ca. 45 nm is observed in the LSCF thin films annealed at 500 °C for 2 hours (Figure 2.4a). Upon annealing at 700 °C for 2 hours, the grain size is seen to have increased to ca. 72 nm, with same nano-porosity of even smaller size becoming apparent (Figure 2.4b).

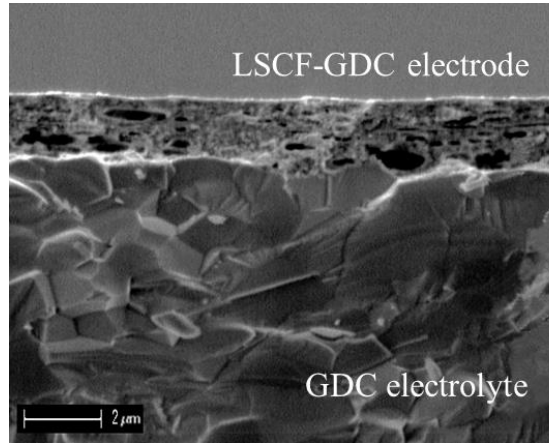


Figure 2.3. A representative scanning electron microscopy image of cross-section of LSCF-GDC nanocomposite thin film deposited onto GDC electrolyte, annealed in air at 700°C for 2 hours

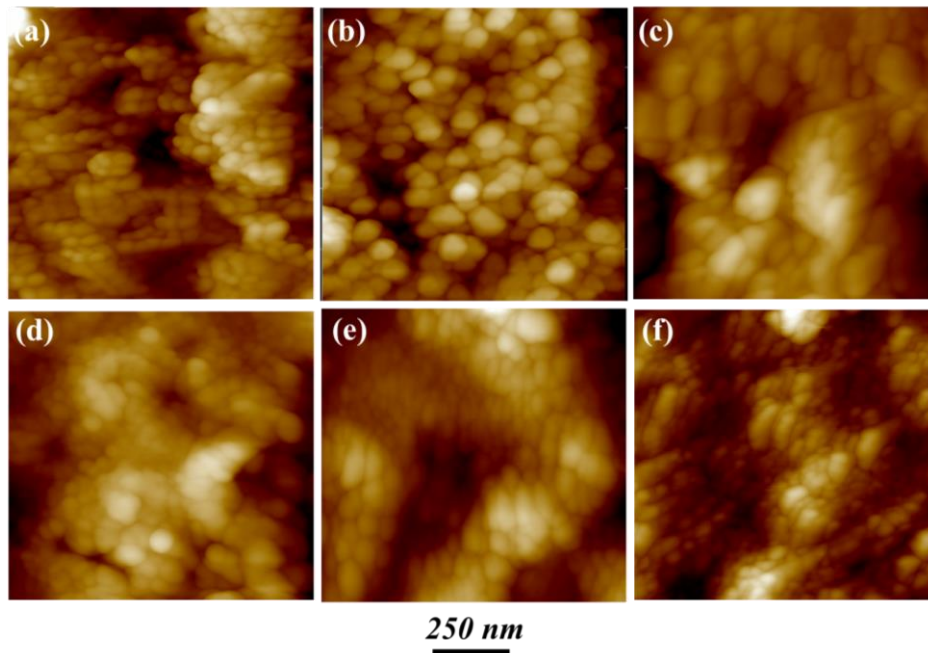


Figure 2.4. Atomic force microscopy (AFM) images of single phase LSCF, annealed at (a) 500°C (b) 700°C for 4 hours and (c) at 600°C for 80 hours following the prior heat treatments. The bottom row shows the AFM images of LSCF-GDC composite thin films, also annealed at (d) 500°C, (e) 700°C for 2 hours, and (f) at 600°C for 80 hours using the same heat treatments.

In order to assess the microstructural stability upon long-term operation at intermediate operating temperatures, the thin films were annealed at 600 °C for 100 hours

after being exposed to 700 °C for 2 hours. In this case, further grain growth to ca. 83 nm is observed by AFM analysis of the single phase LSCF thin films (Figure 2.4c). On the other hand, the LSCF-GDC coated samples showed almost no change in their average grain size, remaining at ca. 60 nm after being exposed to the same heat treatment conditions (Figures 2.4d-f). The addition of GDC, with its high sintering temperature, to the LSCF phase appears to impede grain growth, resulting in very promising morphological stability. This feature, in turn, is expected to induce electrochemical stability as well.

2.4.3. Electrochemical Analysis

Electrochemical impedance spectroscopy (EIS) analysis of the symmetrical LSCF/GDC/LSCF and LSCF-GDC/GDC/LSCF-GDC cells was performed in air. As-deposited thin films were exposed to the heating regime shown in Figure 2.1 and EIS measurements were obtained at each step in Stage IV and intermittently in Stage V.

Representative EIS spectra, obtained from symmetrical cells with single phase LSCF and nanocomposite LSCF-GDC thin film electrodes at the open circuit potential (OCP), all at 600 °C and in stagnant air, are shown in Figure 2.5. For the fitting and interpretation of the EIS data, a Gerischer element, connected in series with a resistor, was used initially, but good fittings could not be achieved. Therefore, an equivalent circuit model, consisting of a series resistance (R_s) in series with two time constants (resistor in parallel to a constant phase element), coded as (R_1Q_1) and (R_2Q_2), was used for the EIS fitting. Since a symmetrical cell configuration was used here, R_1+R_2 corresponds to the total polarization resistance of the two electrodes, with the area specific resistance (ASR) of each electrode given by $(R/2) \times \text{Area}$.

For both the LSCF and LSCF-GDC thin films, a very good fit to this equivalent circuit was achieved ($\chi^2 \sim 10^{-4}$), allowing the accurate determination of the ASR for each electrode. However, because the two time constants are very similar, it was not possible to accurately determine the R_1 and R_2 values separately. In previous work by Molero-Sanchez et al., the EIS responses of the mixed conductor, $\text{La}_{0.3}(\text{Sr or Ca})_{0.7}\text{Fe}_{0.7}\text{Cr}_{0.3}\text{O}_{3-\delta}$ (LSFCr or LCFCr), have been studied in detail to elucidate the oxygen reduction/evolution mechanisms [48-49]. In agreement with the present results, the EIS

spectra consisted of two semi-circles, but with time constants that were further apart from each other, which facilitated the determination of the respective resistance and capacitance values for the LMFCr case ($M = \text{Sr}, \text{Ca}$) [48-49]. In their work, the high frequency semi-circle of the EIS response was ascribed to oxide ion transfer at the mixed conductor/ionic conductor interface, while the low frequency semi-circle was related to oxygen adsorption/desorption, combined with electron transfer, at the mixed conductor/air interface [48-49]. Although not clearly distinguishable in the Nyquist and Bode plots shown in Figure 2.5, it is likely that the EIS responses of the LSCF and LSCF-GDC thin film electrodes, prepared here by the polymeric precursor method, also consists of these two processes.

At 600 °C, the R_s values (Figure 2.5) are 4.8 and 5.4 $\Omega\cdot\text{cm}^2$ for the LSCF and LSCF-GDC thin film electrodes, respectively. These values are in the range of what is expected for a ca. 1 mm thick GDC electrolyte (the electrical conductivity of GDC is ca. 0.025 S/cm at 600 °C [50]), with the slight differences likely due to small variations in the GDC pellet thickness. Interestingly, the single phase LSCF shows a lower ASR value of 0.72 $\Omega\cdot\text{cm}^2$ at 600 °C than that exhibited by LSCF-GDC (2.8 $\Omega\cdot\text{cm}^2$) at the same temperature (Figure 2.5).

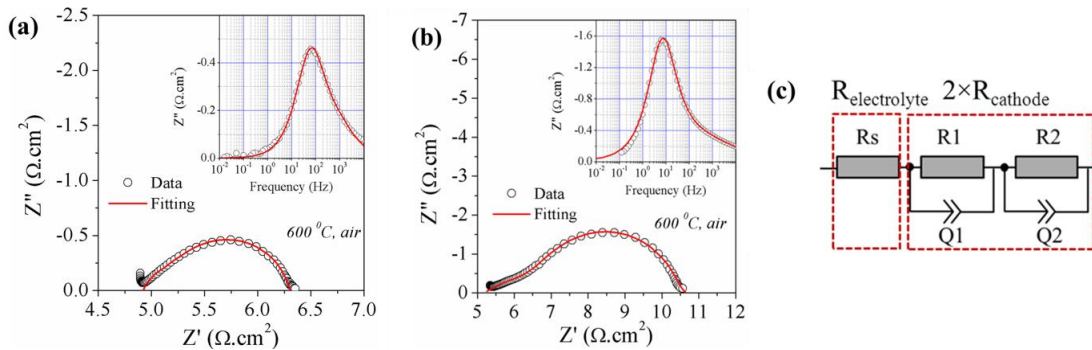


Figure 2.5. Impedance spectra obtained from (a) LSCF/GDC/LSCF and (b) LSCF-GDC/GDC/LSCF-GDC symmetrical half cells at 600°C in air, (c) the equivalent circuit model used to fit the obtained impedance data

In order to determine whether this trend persists over a wider temperature range and to obtain more information about the ORR/OER mechanism, EIS measurements were performed at 400 - 700 °C and the ASR values for each electrode were plotted versus $1000/T$ (Figure 2.6). This figure (Figure 2.6) also provides a comparison with data from the literature for thick and thin LSCF and LSCF-GDC films fabricated by other methods [14,16,28,32-36]. The activation energies associated with the $\text{ASR}_{\text{electrode}}$ of the electrode

materials under investigation here (Figure 2.6) were determined from the Arrhenius Equation (Equation 2.1),

$$ASR_{\text{electrode}} = A \exp\left(\frac{-E_a}{kT}\right) \quad (2.1)$$

where A is the pre-exponential factor, E_a is the activation energy, k is the Boltzman constant and T is the absolute temperature.

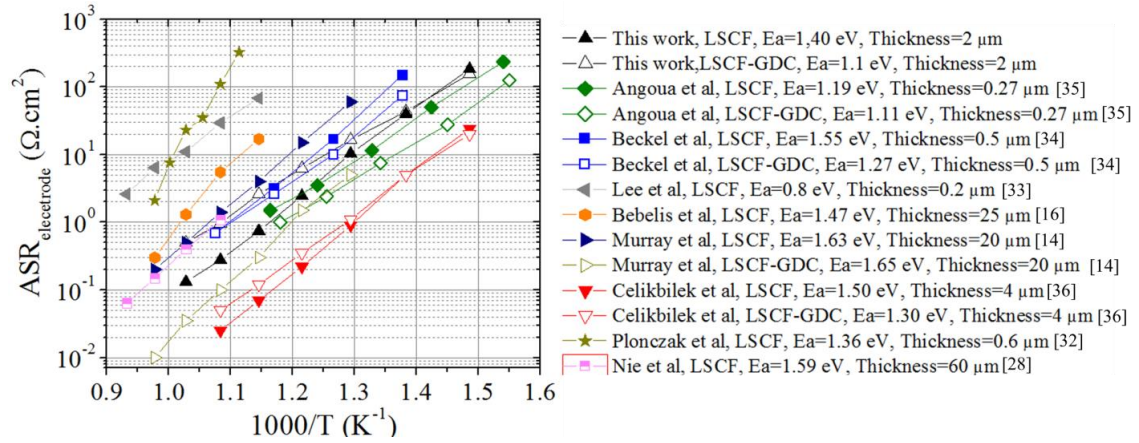


Figure 2.6. Impedance spectra obtained from the temperature dependence of the polarization resistance ($ASR_{\text{electrode}}$) values obtained from the fitting of the impedance data. The polarization resistance data, obtained other groups have been added from comparison.

In general, the LSCF thin films prepared by the polymeric precursor technique yield a very low $ASR_{\text{electrode}}$ value and an E_a of 1.40 eV, which is within the generally observed range of 1.19-1.63 eV (Figure 2.6). In comparison to the single phase LSCF electrodes, which have thicknesses varying between 20-60 μm and were fabricated by powder sintering methods, those prepared here in the form of ca. 2- μm thick films using the polymeric precursor method gave much lower $ASR_{\text{electrode}}$ values (Figure 2.6). For example, the lowest $ASR_{\text{electrode}}$ value reported for the sintered LSCF electrodes is ca 1.5 $\Omega\cdot\text{cm}^2$ at 600 $^\circ\text{C}$, corresponding to ca. five times that obtained in the present work (Figure 2.6). This difference is likely due to the nanoscale electrode morphology reported here, as opposed to the micro-scaled electrodes produced by powder sintering methods [32-35].

The LSCF thin films fabricated by the polymeric precursor method in this work also significantly outperform those prepared by PLD and RF-magnetron sputtered methods, due to the lack of porosity reported in those studies [32,33], as opposed to the

micro (Figure 2.3) and nanoscale porosity (Figure 2.4) observed here. Angoua et al [35] and Beckel et al [34] fabricated LSCF films with thicknesses of 0.27 and 0.5 μm respectively, both by spray pyrolysis. Similar microstructures, having grain sizes of the order of ca. 70 nm, were obtained for the spray pyrolysis derived cathodes [34,35] and those reported here, prepared by the polymeric precursor technique. However, the electrode polarization resistances of the polymeric precursor derived LSCF thin films are somewhat lower at temperatures above 500 $^{\circ}\text{C}$.

The lowest $\text{ASR}_{\text{electrode}}$ values reported for the single phase LSCF electrodes are those fabricated by ESD with a thickness of ca. 4 μm [36, [Figure 2.6]]. These electrodes are also the only ones that exceed the electrochemical activity of the LSCF thin films reported here [Figure 2.6]. These promising performances were achieved as a result of optimized microstructures (e.g., pore size distribution) and electrode thicknesses for the given morphology. For example, an earlier report by the same group [37] indicates an $\text{ASR}_{\text{electrode}}$ of 1.2 $\Omega\cdot\text{cm}^2$ in the case of 13 μm -thick LSCF before achieving the maximum performances given in Figure 2.6. Considering this, it is suggested that there is potential for improvement in the initial electrode performance of the LSCF thin films prepared by the polymeric precursor technique, reported for the first time here.

The LSCF-GDC thin films, prepared by the polymeric precursor technique, yield higher $\text{ASR}_{\text{electrode}}$ values than the single phase LSCF, prepared by the same method over the 500-700 $^{\circ}\text{C}$ range (Figure 2.6). These $\text{ASR}_{\text{electrode}}$ values are in the range of those reported by Beckel et al for spray pyrolysis derived LSCF-GDC thin films [34].

This decrease in performance upon the addition of the GDC phase is accompanied by a decrease in the E_a from 1.40 to 1.10 eV (Figure 2.6). The general trend in the literature, as seen in Figure 2.6, is a decrease in the activation energy, concomitant with a decrease in the $\text{ASR}_{\text{electrode}}$ values. The reason for the decrease in E_a accompanied by a decrease in E_a is explained schematically in Figure 2.7, which shows what are likely the main steps during oxygen reduction (ORR) and vice versa (in the reverse direction) during oxygen evolution (OER), with both processes being relevant during EIS measurements carried out at the OCP. It is generally accepted that, during the ORR at LSCF electrodes, oxygen is initially adsorbed on the LSCF surface (Step I), followed by its reduction to O^{2-} . While this reduction reaction likely consists of many individual steps, these are not generally apparent as separate time constants in EIS studies at LSCF. The O^{2-} ions are then transported (Step II) through the LSCF lattice due to its mixed ionic-electronic

conducting properties (MIEC) (Step III). Finally, the O^{2-} ions transfer from the electrode into the electrolyte (Step IV) (Figure 2.7a).

In Figure 2.7b, the addition of GDC to LSCF is shown to provide multiple other pathways during the ORR. Specifically, instead of the sluggish transport through the LSCF phase, which is known to be an order of magnitude lower in its ionic conductivity compared to the electrolyte material (GDC) [15,51], O^{2-} ions likely prefer to diffuse through the GDC phase, which offers much less resistance to diffusion and thus would require a smaller activation energy (Figure 2.7) than does O^{2-} transport through LSCF [14,15,51]. Hence, the overall activation energy is lowered in the case of the composite catalyst.

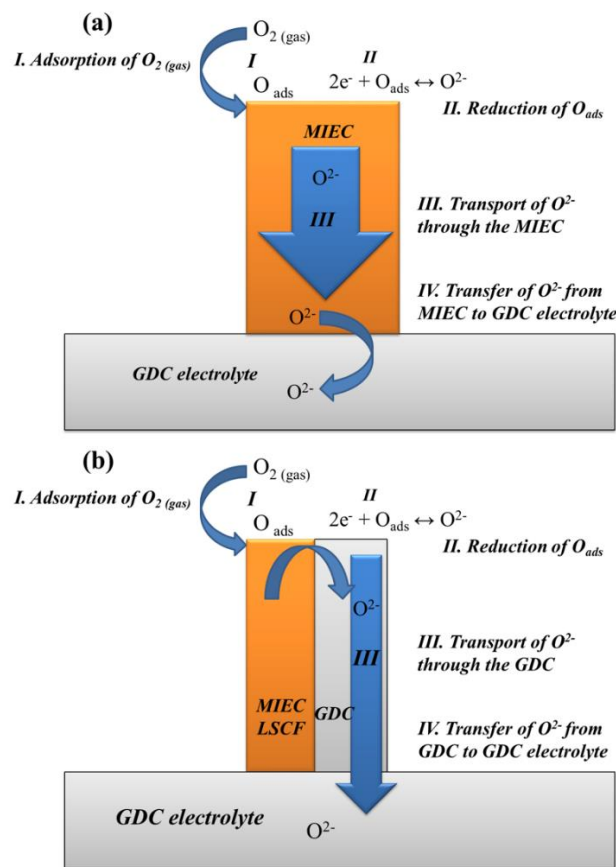


Figure 2.7. Schematic representation of the proposed oxygen pathways for (a) single phase LSCF and (b) LSCF-GDC nanocomposite cathode.

In this scheme, if the rate limiting step is oxygen exchange at the surface rather than oxygen ion transport in the LSCF lattice, although the addition of GDC may induce some reduction in E_a , it may also cause an increase in $ASR_{electrode}$ due to the LSCF/gas interfacial area lost as a result of the partial replacement of LSCF by GDC, which we propose is the case in the case of polymeric precursor driven LSCF-GDC electrodes

(Figure 2.7). Celikbilek et al [36] also observed a decrease in E_a without a decrease in the $ASR_{\text{electrode}}$ value, but attributed this to a change in porosity of the electrode layer induced by GDC addition. Here, we observe no such effect (Figure 2.4).

2.4.4. Long Term Stability Tests

The long term stability of the polymeric precursor-derived LSCF and LSCF-GDC thin films was evaluated by intermittently collecting EIS data at 600 °C in stagnant air. The long-term stability test corresponds to Stage V in the heating regime given in Figure 2.1. This means that, prior to these tests, the samples were heated to 400 °C (Stage I), then stepwise up to 700 °C (Stage II), annealed at this temperature for 2 hours (Stage III), and finally cooled down to 400 °C (Stage IV) stepwise. A comparison of the changes in the impedance spectra of the LSCF and LSCF-GDC thin film catalysts with time at 600 °C is given in Figures 2.8a and 8b. The total polarization resistance increased from ca. 2 $\Omega\cdot\text{cm}^2$ to 2.7 $\Omega\cdot\text{cm}^2$ in 42 hours at 600 °C in stagnant air in the case of the single phase LSCF thin film (Figure 2.8a). On the other hand, a much smaller increase is observed in the case of the LSCF-GDC nanocomposite thin films under the same conditions (increasing from 6.3 $\Omega\cdot\text{cm}^2$ to only 6.7 $\Omega\cdot\text{cm}^2$ in 91 hours in air). For a clearer comparison, the polarization resistances of both of these electrodes were normalized to their values at the beginning of the long-term measurement and are plotted against time in Figure 2.8c. The ASR value of the single phase LSCF thin film increased by 54% in 42 hours in air, while the LSCF-GDC nanocomposite thin film exhibited a much more stable electrochemical performance, showing an increase of only 7% in the ASR value over the same time period.

An important parameter that can be detrimental in terms of the long-term performance of thin film electrodes for SOFC applications is their microstructural stability. As discussed earlier, the single phase LSCF thin film exhibits a noticeable microstructural coarsening upon long-term annealing at elevated temperatures (Figure 2.4a-c), likely causing the electrochemically active surface area to diminish. On the other hand, the LSCF-GDC composite thin films exhibit a stable microstructure upon annealing (Figure 2.4d-f), correlated with the retention of its electrochemically active surface area, and thus, its ASR value.

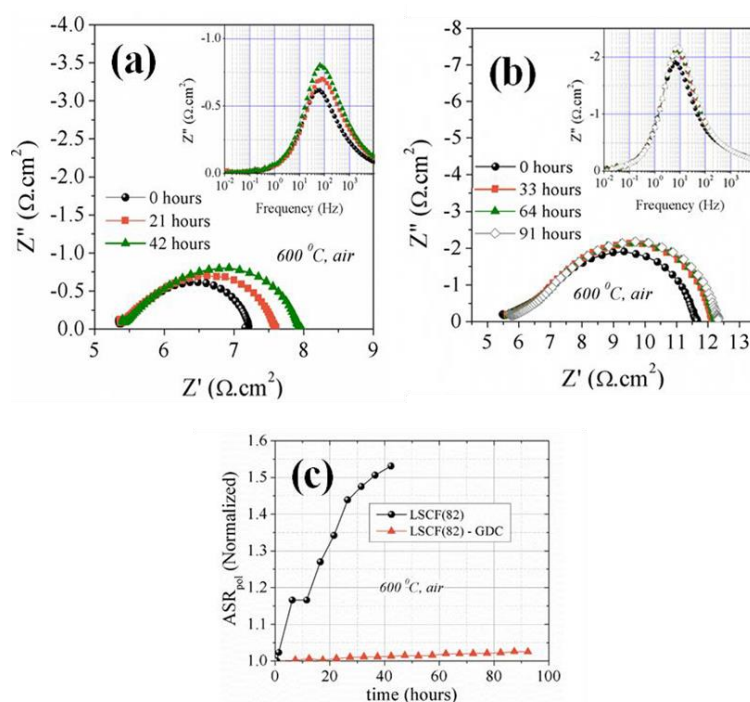


Figure 2.8. Changes in the impedance spectra obtained from (a) symmetrical LSCF/GDC/LSCF half-cells, (b) symmetrical LSCF-GDC/GDC/LSCF-GDC half-cells, and (c) the normalized polarization resistances of both the LSCF and LSCF-GDC thin film electrodes with time at 600 °C.

An important parameter that can be detrimental in terms of the long-term performance of thin film electrodes for SOFC applications is their microstructural stability. As discussed earlier, the single phase LSCF thin film exhibits a noticeable microstructural coarsening upon long-term annealing at elevated temperatures (Figure 2.4a-c), likely causing the electrochemically active surface area to diminish. On the other hand, the LSCF-GDC composite thin films exhibit a stable microstructure upon annealing (Figure 2.4d-f), correlated with the retention of its electrochemically active surface area, and thus, its ASR value.

Despite the clear correlation observed here between the microstructural and electrochemical stability of the LSCF and LSCF-GDC electrodes, we cannot rule out changes in surface chemistry and their effect on the electrochemical performance. It has been asserted in recent reports that the segregation of various species at the surface of oxide electrodes upon long-term operation in air could have detrimental effects on the stability of their electrochemical performance [15,52,53].

In order to determine if there were any changes in the surface chemistry of the LSCF and LSCF-GDC thin film electrodes upon long-term operation at 600 °C, x-ray photoelectron spectroscopy (XPS) analyses were performed. The analyses were carried

out before and after operation at 600 °C, i.e., at the beginning and end of Stage V of the heating protocol shown earlier in Figure 2.1. The corresponding survey scans provided in Figure 2.9 indicate the presence of La, Sr, Co, Fe and O, as well as some carbon at the surface of the LSCF thin films prior to and after long-term annealing at 600 °C. In the case of LSCF-GDC thin films, peaks corresponding to Ce are also apparent. The survey scans also show that the signal intensities from both the LSCF and LSCF-GDC thin films decrease after long term annealing. Therefore, the detailed analysis for each element was performed using a low scan rate (0.1 eV steps) to increase the resolution.

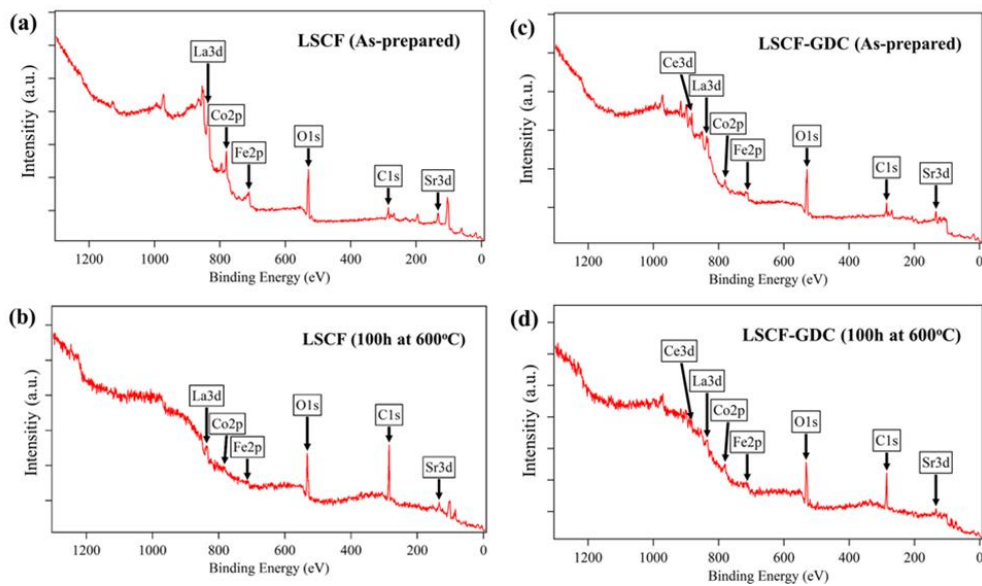


Figure 2.9. X-ray photoelectron spectroscopy survey scans of LSCF thin films a) prior to and b) after long-term annealing at 600 °C, in stagnant air, LSCF-GDC thin films c) prior to and d) after long-term annealing at 600 °C, in stagnant air.

The relative amounts of the cations at the LSCF perovskite surface were calculated from the areas of the relevant XPS peaks of the cations. Table 2.1 provides a summary of the surface composition of the LSCF and LSCF-GDC thin film materials before and after long-term exposure to 600 °C. The polymeric precursors used for the preparation of the LSCF phases in both the single phase and composite thin films had a cation ratio of La:Sr:Fe:Co = 30:20:10:40, which should equate to the cation ratios in the bulk of the films. Before annealing in air at 600 °C (at the beginning of Stage V), Table 2.1 shows that the surface of the LSCF thin films appears to contain much more Fe and much less Co than in the bulk. Upon annealing at 600 °C for 100 hours in air, the surface of the LSCF becomes even richer in Fe and slightly poorer in Co, i.e., the Fe content

increases from 28 to 44%, while the Co content decreases from 21 to 17% (Table 2.1). In addition, prior to long-term annealing, the La content at the LSCF surface is 35%, which is slightly higher than in the bulk. Upon long-term annealing at 600 °C, the La content decreases to ca. 20% at the surface. On the other hand, the Sr content is close to that expected for the bulk of the material, both before and after long-term annealing.

In the case of the LSCF-GDC nanocomposite thin films, the surface is observed to contain 33% Sr and 27% Fe at short times, while in the bulk of the LSCF-GDC film, the LSCF phase should consist of 20% Sr and 10% Fe (Table 2.1). This points to the preferential segregation of these elements at the surface. Long-term annealing at 600 °C causes a decrease in the relative amounts of La (from 26.9 to 18.6%), Sr (from 32.8 to 9.3%), and Fe (from 27.2 to 20.6 %), but an increase (from 13.1 to 51.6 %) in Co at the LSCF/air interface, pointing to Co enrichment at the surface.

A-site segregation is commonly observed at the surface of oxide perovskites, where Sr is the A site dopant and La is the A site host. For example, Lee et al. observed that the surface of $\text{La}_{0.8}\text{Sr}_{0.2}\text{MnO}_3$ (LSM) thin films, fabricated by pulsed laser deposition (PLD), became rich in SrO particles upon being annealed at 800 °C for 1 hour in air [54]. Very similar results were also obtained for PLD-derived $\text{La}_{0.6}\text{Sr}_{0.4}\text{CoO}_3$ thin films upon annealing at 650 °C in air [55]. The reason for the segregation phenomenon is due to two driving forces, the first being the elastic strain generated by the size mismatch between the larger Sr (dopant) and the La (host), causing Sr to be expelled from the lattice. A second driver is the electrostatic interactions between the negatively charged Sr'_{La} and the positively charged oxygen vacancies V_{O} that are mostly concentrated at the perovskite surface [56].

It should be noted that detailed investigations of surface segregation on oxide perovskite surfaces has been performed on thin films fabricated by pulsed laser deposition [54-56], while several studies have also examined perovskites prepared by liquid precursor based methods [57-58]. In this case, contrary to what has been reported for PLD-derived thin film perovskites, B-site surface segregation takes place at the electrode surface, instead of A-site segregation [58]. For example, Dieterle et al. observed the formation of Co_3O_4 precipitates in $\text{La}_{0.6}\text{Sr}_{0.4}\text{CoO}_3$ thin film perovskites prepared by a propionic acid-based precursor method upon long-term annealing in air at 700 and 800 °C [59].

B-site enrichment at the LSCF and LSCF-GDC nanocomposite thin film surfaces observed here is similar to what has been reported for liquid precursor derived perovskite

materials in the literature [57]. In the LSCF sample, Figure 2.9 and Table 2.1 show that Fe enrichment is observed after long-term heat treatment. In the case of the LSCF-GDC thin films, although the surface was rich in Sr and Fe initially, Co enrichment occurs upon long-term annealing. It should also be noted that, at the LSCF-GDC surface, the relative amount of Fe (20.6%) is still higher than the expected bulk value (10%) after long-term annealing, but much less pronounced in comparison to the case of long-term annealed LSCF. The reason for the different B-site cation (Fe or Co) segregation in the absence and presence of the GDC phase upon long-term annealing is likely that Fe tends to dissolve in GDC [60-61], which could have prevented its segregation to the outer surface, allowing Co to take its place.

Table 2.1. Surface cation % of LSCF and LSCF-GDC thin films annealed at 700°C for 4 hours, before and after long term annealing at 600°C, obtained from x-ray photoelectron spectroscopy analyses

	Atomic % of each element present according to XPS results			
	La	Sr	Fe	Co
Bulk	30	20	10	40
LSCF before long-term annealing at 600 °C	35.1	16.2	27.6	21.0
LSCF after long-term annealing at 600 °C	19.6	19.4	43.9	17.1
LSCF-GDC before long-term annealing at 600 °C	26.9	32.8	27.2	13.1
LSCF-GDC after long-term annealing at 600 °C	18.6	9.3	20.6	51.6

Overall, these results show that the addition of GDC to LSCF thin film cathodes influences the evolution of both the microstructure and the surface composition. The fact that the stabilization of the electrochemical performance at 600 °C is concomitant with the stabilization of the microstructural features (e.g., grain size) upon GDC addition to LSCF points to a strong correlation between these two parameters. Our XPS analyses suggest that the surface composition is dynamic, rather than stable, during exposure to air at 600 °C for both the LSCF and LSCF-GDC thin films. This is because the addition of GDC to the LSCF appears to suppress Fe segregation at the LSCF/air interface. However, the fact that Co segregates to the air/LSCF interface makes it difficult to rule out the

evolution of the surface chemistry as relevant to the long-term stability of the LSCF and LSCF-GDC thin film electrodes under study here.

2.5. Summary

In this work, our goal was to fabricate single-phase $\text{La}_{1-x}\text{Sr}_x\text{Co}_{1-y}\text{Fe}_y\text{O}_3$ (LSCF) and composite LSCF- gadolinia doped ceria (GDC) thin film electrodes for use as cathodes in intermediate temperature solid oxide fuel cell (IT-SOFC) applications by using a facile and cost effective polymeric precursor method to obtain nanoscale morphology and thus low polarization resistances in air at 600 °C. The microstructure of the LSCF thin films annealed at 700 °C consisted of particles of 72 nm average size, which increased to 83 nm upon long-term annealing at 600 °C, thus retaining their nanosizes. The LSCF-GDC composite electrodes exhibited microstructures with average particle sizes of ca. 60 nm, which remained significantly more stable upon long-term annealing at 600 °C.

The electrochemical performance of the LSCF and LSCF-GDC thin film electrodes was evaluated by electrochemical impedance spectroscopy (EIS) measurements carried out at the open circuit potential in air using symmetrical half-cells. Electrode polarization resistances of 0.72 $\Omega\cdot\text{cm}^2$ and 2.75 $\Omega\cdot\text{cm}^2$ (per electrode) were achieved in single phase LSCF and LSCF-GDC composite at 600 °C in stagnant air, respectively. This contradicts with most of the previous results in the literature, which have reported an increase in the electrochemical activity upon the addition of an ionic conductor to the LSCF perovskite.

This contradiction was explained here by the fact that the Co-rich composition of the LSCF studied in the present case exhibits high enough ionic conductivity that the introduction of another ionically conductive (but electrocatalytically inactive) phase is not necessary. Therefore, the partial replacement of the electrocatalytic LSCF that also exhibits ionic conductivity results primarily in a loss of electrocatalytically active LSCF surface area.

The longevity tests revealed that, at 600 °C, the single phase LSCF thin film exhibited a ca. 50% increase in polarization resistance in 40 hours, whereas the LSCF-GDC thin film remained very stable, showing only a ca. 3% increase. This difference

between the long-term performances of the single phase and composite electrode materials was found to be related to the differences in the evolution of their microstructure and possibly also their surface chemistry.

X-ray photoelectron spectroscopy analyses showed that Fe and Fe/Co enrichment occurs at the outer surface of the single phase LSCF and composite LSCF-GDC thin films, respectively, upon prolonged exposure to 600 °C in air, which may also have some impact on the long-term stability of these two types of electrodes. The B-site segregation observed here, as opposed to the findings in the literature that suggested the occurrence of Sr surface enrichment in similar materials, is likely due to differences in the thin film fabrication techniques used.

In conclusion, the fact that the polymeric precursor derived LSCF exhibits similar (and at certain temperatures, still lower) polarization resistances to those reported by others for spray pyrolysis derived LSCF thin film electrodes suggests that this cost-effective and facile technique can be adopted for thin film SOFC electrode fabrication. However, the addition of GDC, while useful for microstructural stabilization, must be kept to a minimum in order to ensure that not too much of the catalytically active LSCF surface is sacrificed.

Acknowledgements

AB gratefully acknowledges the Eyes High PDF program at the University of Calgary and Alberta Innovates – Technology Futures (AITF) for his financial support. The authors also thank the Natural Sciences and Engineering Research Council of Canada (NSERC) and the Izmir Institute of Technology for the overall support of this research. Thanks are also due to Dr. Orhan Ozturk for his help with the XRD measurements. This project was also partially supported by the Izmir Institute of Technology (BAP project number: 2015IYTE31).

2.6. References

- [1] Huijsmans, J.; Berkel, F. V.; Christie, G. *Journal of Power Sources* **1998**, *71* (1-2), 107–110.

- [2] Tarancón, A. *Energies* **2009**, 2 (4), 1130–1150.
- [3] Barnett, S. *Energy* **1990**, 15 (1), 1–9.
- [4] Weber, A.; Ivers-Tiffée, E. *Journal of Power Sources* **2004**, 127 (1-2), 273–283.
- [5] Stambouli, A. B.; Traversa, E. *Renewable and Sustainable Energy Reviews* **2002**, 6 (3), 295–304.
- [6] Adler, S. B. *Chemical Reviews* **2004**, 104 (10), 4791–4844.
- [7] Chen, C.; Bouwmeester, H. J. M.; Kruidhof, H.; Elshof, J. E. T.; Burggraaf, A. *J. J. Mater. Chem.* **1996**, 6 (5), 815–819.
- [8] Beckel, D.; Bieberle-Hütter, A.; Harvey, A.; Infortuna, A.; Muecke, U.; Prestat, M.; Rupp, J.; Gauckler, L. *Journal of Power Sources* **2007**, 173 (1), 325–345.
- [9] Kharton, V.; Marques, F.; Atkinson, A. *Solid State Ionics* **2004**, 174 (1-4), 135–149.
- [10] Nielsen, J.; Jacobsen, T.; Wandel, M. *Electrochimica Acta* **2011**, 56(23), 7963–7974.
- [11] Bieberle-Hütter, A.; Beckel, D.; Infortuna, A.; Muecke, U. P.; Rupp, J. L.; Gauckler, L. J.; Rey-Mermet, S.; Murali, P.; Bieri, N. R.; Hotz, N.; Stutz, M. J.; Poulikakos, D.; Heeb, P.; Müller, P.; Bernard, A.; Gmür, R.; Hocker, T. *Journal of Power Sources* **2008**, 177 (1), 123–130.
- [12] Vohs, J. M.; Gorte, R. J. *Advanced Materials* **2009**, 21 (9), 943–956.
- [13] Jiang, S. P. *International Journal of Hydrogen Energy* **2012**, 37 (1), 449–470.
- [14] Murray, E.P.; Sever, M.J.; Barnett, S.A.; *Solid State Ionics* **2002**, 148, 27–34.
- [15] Dusastre, V.; Kilner, J. *Solid State Ionics* **1999**, 126 (1-2), 163–174.
- [16] Bebelis S, Kotsionopoulos N, Mai A, Tietz F. *Journal of Applied Electrochemistry* **2006**, 37, 15–20.
- [17] Liu, M.; Ding, D.; Blinn, K.; Li, X.; Nie, L.; Liu, M. *International Journal of Hydrogen Energy* **2012**, 37 (10), 8613–8620.
- [18] Wang, W.; Mogensen, M. *Solid State Ionics* **2005**, 176 (5-6), 457–462.
- [19] Leng, Y.; Chan, S.; Liu, Q. *International Journal of Hydrogen Energy* **2008**, 33 (14), 3808–3817.
- [20] Tomov, R. I.; Mitchell-Williams, T.; Gao, C.; Kumar, R. V.; Glowacki, B. A. *Journal of Applied Electrochemistry* **2017**, 47(5), 641–651.

- [21] Chrzan, A.; Karczewski, J.; Gazda, M.; Szymczewska, D.; Jasinski, P. *Journal of the European Ceramic Society* **2017**, 37(11), 3559–3564.
- [22] Shah, M.; Barnett, S. *Solid State Ionics* **2008**, 179(35-36), 2059–2064.
- [23] Liu, Y.; Wang, F.; Chi, B.; Pu, J.; Jian, L.; Jiang, S. P. *Journal of Alloys and Compounds* **2013**, 578, 37–43.
- [24] Shah, M.; Voorhees, P. W.; Barnett, S. A. *Solid State Ionics* **2011**, 187(1), 64–67.
- [25] Kim, J. H.; Kim, H. *Ceramics International* **2012**, 38(6), 4669–4675.
- [26] Burye, T. E.; Nicholas, J. D. *Journal of Power Sources* **2015**, 276, 54–61.
- [27] Burye, T. E.; Nicholas, J. D. *Journal of Power Sources* **2016**, 301, 287–298.
- [28] Nie, L.; Liu, M.; Zhang, Y.; Liu, M. *Journal of Power Sources* **2010**, 195(15), 4704–4708.
- [29] Gauckler, L. J.; Beckel, D.; Buergler, B. E.; Jud, E.; Muecke, U. P.; Prestat, M.; Rupp, J. L.; Richter, J. *CHIMIA International Journal for Chemistry* **2004**, 58 (12), 837–850.
- [30] Buyukaksoy, A.; Birss, V. I. *Journal of Power Sources* **2016**, 307, 449–453.
- [31] Ralph, J. M.; Rossignol Cécile; Kumar, R. *Journal of The Electrochemical Society* **2003**, 150 (11).
- [32] Plonczak, P.; Søgaard, M.; Bieberle-Hütter, A.; Hendriksen, P. V.; Gauckler, L. J. *Journal of The Electrochemical Society* **2012**, 159(5).
- [33] Lee, J. W.; Liu Z.; Yang, L.; Abernathy, H.; Choi, S. H.; Kim, H. E.; Liu, M. *Journal of Power Sources* **2009**, 190, 307.
- [34] Beckel, D.; Muecke, U.; Gyger, T.; Florey, G.; Infortuna, A.; Gauckler, L. *Solid State Ionics* **2007**, 178 (5-6), 407–415.
- [35] Angoua, B. F.; Slamovich, E. B. *Solid State Ionics* **2012**, 212, 10–17.
- [36] Celikbilek, O.; Jauffrès, D.; Siebert, E.; Dessemond, L.; Burriel, M.; Martin, C. L.; Djurado, E. *Journal of Power Sources* **2016**, 333, 72–82.
- [37] Marinha, D.; Dessemond, L.; Djurado, E. *Journal of Power Sources* **2012**, 197, 80–87.
- [38] Celikbilek, O.; Jauffres, D.; Dessemond, L.; Burriel, M.; Martin, C. L.; Djurado, E. *ECS Transactions* **2016**, 72 (7), 81–92. 18157–18165.

- [39] Prestat, M.; Koenig, J.-F.; Gauckler, L. J. *Journal of Electroceramics* **2007**, *18* (1-2), 87–101.
- [40] Prestat, M.; Infortuna, A.; Korrodi, S.; Rey-Mermet, S.; Mural, P.; Gauckler, L. J. *Journal of Electroceramics* **2007**, *18* (1-2), 111–120.
- [41] Anderson, H U.; Chen, C. C.; Nasrallah, M. M. *U.S. Patent 5* **1996**, 494, 700
- [42] Buyukaksoy, A.; Kammampata, S. P.; Birss, V. I. *Journal of Power Sources* **2015**, *287*, 349–358.
- [43] Darbandi, A. J.; Hahn, H. *Solid State Ionics* **2009**, *180* (26-27), 1379–1387.
- [44] Mineshige, A.; Izutsu, J.; Nakamura, M.; Nigaki, K.; Abe, J.; Kobune, M.; Fujii, S.; Yazawa, T. *Solid State Ionics* **2005**, *176* (11-12), 1145–1149.
- [45] Zhou, W.; Ran, R.; Shao, Z.; Zhuang, W.; Jia, J.; Gu, H.; Jin, W.; Xu, N. *Acta Materialia* **2008**, *56*(12), 2687–2698.
- [46] Gordes, P.; Christiansen, N.; Jensen, E. J.; Villadsen, J. *Journal of Materials Science* **1995**, *30* (4), 1053–1058.
- [47] Angoua, B. F.; Cantwell, P. R.; Stach, E. A.; Slamovich, E. B. *Solid State Ionics* **2011**, *203* (1), 62–68.
- [48] Molero-Sánchez, B.; Addo, P.; Buyukaksoy, A.; Birss, V. *Journal of The Electrochemical Society* **2017**, *164* (10).
- [49] Molero-Sánchez, B.; Addo, P.; Buyukaksoy, A.; Paulson, S.; Birss, V. *Faraday Discussions* **2015**, *182*, 159–175.
- [50] Reddy, K. R.; Karan, K. *Journal of Electroceramics* **2005**, *15* (1), 45–56.
- [51] Murray, E. P.; Barnett, S. A. *Solid State Ionics* **2001**, *143* (3-4), 265–273.
- [52] Simner, S. P.; Anderson, M. D.; Engelhard, M. H.; Stevenson, J. W. *Electrochemical and Solid-State Letters* **2006**, *9* (10).
- [53] Vovk, G.; Chen, X.; Mims, C. A. *The Journal of Physical Chemistry B* **2005**, *109* (6), 2445–2454.
- [54] Lee, W.; Yildiz, B. *ECS Transactions* **2013**, *57* (1), 2115–2123.
- [55] Cai, Z.; Kubicek, M.; Fleig, J.; Yildiz, B. *Chemistry of Materials* **2012**, *24* (6), 1116–1127.
- [56] Lee, W.; Han, J. W.; Chen, Y.; Cai, Z.; Yildiz, B. *Journal of the American Chemical Society* **2013**, *135* (21), 7909–7925.

- [57] Liu, Y.; Chen, J.; Wang, F.; Chi, B.; Pu, J.; Jian, L. *International Journal of Hydrogen Energy* **2014**, *39* (7), 3404–3411.
- [58] Liu, Y.; Wang, F.; Chi, B.; Pu, J.; Jian, L.; Jiang, S. P. *Journal of Alloys and Compounds* **2013**, *578*, 37–43.
- [59] Dieterle, L.; Bockstaller, P.; Gerthsen, D.; Hayd, J.; Ivers-Tiffée, E.; Guntow, U. *Advanced Energy Materials* **2011**, *1* (2), 249–258.
- [60] Zhang, T.; Ma, J.; Kong, L.; Chan, S.; Kilner, J. *Solid State Ionics* **2004**, *170* (3-4), 209–217.
- [61] Mazan, M. O.; Marrero-Jerez, J.; Soldati, A.; Núñez, P.; Larrondo, S. A. *International Journal of Hydrogen Energy* **2015**, *40* (10), 3981–3989.

CHAPTER 3

ELECTROCHEMICAL PERFORMANCE OF $\text{La}_{0.6}\text{Sr}_{0.4}\text{Co}_{0.2}\text{Fe}_{0.3}\text{O}_3\text{-Ce}_{0.9}\text{Gd}_{0.1}\text{O}_{2-\delta}$ COMPOSITE SOFC CATHODES FABRICATED BY ELECTROCATALYST AND/OR ELECTROCATALYST-IONIC CONDUCTOR INFILTRATION

Can Sındıraç¹, Aligül Büyükaksoy^{2,3*}, Sedat Akkurt¹,

¹ Izmir Institute of Technology, Department of Mechanical Engineering, Urla, İzmir, 35433 Turkey

² Gebze Technical University, Department of Materials Science and Engineering, Gebze, Kocaeli 41400, Turkey

³ Gebze Technical University, Institute of Nanotechnology, Gebze, Kocaeli 41400, Turkey

*Corresponding Author:

E-mail: sedatakkurt@iyte.edu.tr (S.Akkurt) Ph: +90 (262) 750 6705

This chapter is published in Journal of Sol-Gel Science and Technology

(DOI: 10.1007/s10971-019-05073-5)

3.1. Abstract

Infiltration of electrocatalyst precursor solutions into previously sintered porous ionic conductor scaffolds has been used recently as an alternative method to the conventional co-sintering route to fabricate electrocatalyst-ionic conductor composites for solid oxide fuel cell (SOFC) cathode applications. However, the aqueous nitrate solutions generally used to perform the infiltration process results in electrocatalyst precipitates that are disconnected from each other, yielding poor electrode performance. In this work, polymeric electrocatalyst ($\text{La}_{0.6}\text{Sr}_{0.4}\text{Co}_{0.2}\text{Fe}_{0.8}\text{O}_3$ - LSCF) precursors that produce interconnected thin films upon heat treatment were used to infiltrate porous ionic conductor $\text{Ce}_{0.9}\text{Gd}_{0.1}\text{O}_{2-\delta}$ (GDC) scaffolds to overcome these issues. In addition, for the first time in the literature, a mixture of LSCF and GDC polymeric precursors, which would yield LSCF+GDC nanocomposite coatings on the grains of the porous GDC

scaffold were used as the infiltration solution. Thus, further enhancement of the electrocatalyst/ionic conductor interfacial area and achievement of improved electrode performance was aimed. As a result of the optimization studies, the lowest measured area specific polarization resistance (ASR_{cathode}) values of 0.47 and 0.73 $\Omega\cdot\text{cm}^2$ were obtained for polymeric LSCF+GDC and LSCF precursor infiltrations respectively at 700 °C, in air. In addition, LSCF+GDC infiltration yielded electrodes with much improved long-term stability in comparison to those obtained by LSCF infiltration.

Keywords: SOFC, GDC, LSCF, impedance, infiltration, electrochemical performance

3.2. Introduction

Solid oxide fuel cells (SOFC) have attracted attention due to their potential for clean energy generation via conversion of chemical energy directly into electrical energy without being restricted by Carnot efficiency [1-2]. SOFCs allow the use of different fuels such as hydrocarbons, coal syngas and pure hydrogen [3]. Despite the significant progress that has been made, the cost and durability still remains a major barrier to the commercialization of SOFC technology [4]. High operating temperatures of traditional SOFCs (800-1000°C) need to be lowered to reduce the cost of both materials and the electricity production [5, 6]. For example, if the SOFCs can be operated below 700 °C (intermediate temperatures), running costs may be reduced by allowing the use of cost-effective steel interconnects instead of expensive ceramic ones. The diffusion controlled chemical and microstructural degradation observed at high operating temperatures can also be prevented this way [7]. Moreover, lowering the operating temperatures can lead to shorter startup/shutdown time and enhanced SOFC system durability [8].

On the other hand, any reduction of the operation temperature has significant negative effects on SOFC performance due to lowered electrocatalytic activity of the electrodes [9] and increased ohmic losses [10]. As far as the electrolyte performance is concerned, the use of a thin electrolyte layer and/or an electrolyte with a higher ionic conductivity are proposed as alternatives to avoid performance loss in intermediate temperature (IT) SOFCs [11-14]. Improvements in the electrolyte layer are helpful but there is still room for further enhancement in performance of SOFCs for operation in the

IT range. Studies have shown that as the operating temperature is reduced, cathode polarization resistance becomes the dominant factor limiting the SOFC performance [15-17]. Therefore, enhancement of the cathode performance for IT-SOFCs has been rigorously investigated [15-19]. Especially perovskite electrocatalysts that exhibit mixed ionic-electronic conductivity (MIEC) along with electrocatalytic activity for oxygen reduction, for example; $\text{La}_{1-x}\text{Sr}_x\text{Co}_{1-y}\text{Fe}_y\text{O}_3$ (LSCF), has shown promise, both as a single phase porous electrode and in the form of a perovskite-ionic conductor composite [16-20]. In the latter case, the main advantage of the ionic conductor addition has been to facilitate the oxygen ion transfer from the electrocatalyst to the ionic conductor by enhancing the interfacial area between these two phases [16,20]. In addition to the choice of material, the process selected to fabricate the cathode layer is especially crucial to obtain low polarization resistances at the IT range, since it determines the microstructure of the cathode.

Conventional composite SOFC cathodes are prepared by co-firing of a mixture of powders of different particle sizes, surface areas and melting points which lead to different sintering temperatures and eventually uneven sintering. In addition, the relatively high sintering temperatures (1100-1300°C) required to ensure bonding between i) the cathode particles themselves, and ii) the cathode-electrolyte interface yield large electrocatalyst particle sizes. This leads to diminished electrocatalyst-gas and electrocatalyst-ionic conductor interfacial areas and hence high cathode polarization resistances. Moreover, formation of undesired phases with high resistivity, such $\text{La}_2\text{Zr}_2\text{O}_7$, has been reported under these processing conditions [21]. As an alternative strategy, infiltration (or wet impregnation) method has been proposed as an effective method to prepare electrocatalyst-ionic conductor composite cathodes [19-20,22]. In general, a liquid solution, typically composed of metal nitrates of the electrocatalyst cations dissolved in water, is introduced into a previously sintered porous ionic conductor scaffold layer formed on the electrolyte [23,24]. Upon heating to 300-500 °C, salts are precipitated inside the pores and are subsequently calcined in order to form the desired oxide. This process is repeated several times to achieve the desired electrocatalyst loading within the pores of porous ionic conductor scaffold [23,25]. The main advantage of the infiltration method is that it allows relatively low heat treatment temperatures (300-500 °C) which provide i) large electrocatalyst/gas and electrocatalyst/ionic conductor interfacial areas, and ii) minimized reactions between the infiltrated and scaffold phases and potentially high cathode performance [26].

Many researchers have studied the infiltration of aqueous solutions containing the nitrate salts of the cations constituting the MIEC perovskites [23-25]. It has been reported that LSCF infiltration into porous ionic conductor scaffold (e.g. GDC) results in improved performances over those fabricated by co-firing [20,27,28]. For example, an aqueous nitrate LSCF solution infiltration into porous GDC scaffolds was studied by Kim et al. who reported a polarization resistance of $1.7 \Omega \cdot \text{cm}^2$ at 600°C [29]. In the reverse case, Chen et al. indicated that infiltration of GDC into screen printed LSCF scaffold significantly reduced the polarization resistances down to $1.6 \Omega \cdot \text{cm}^2$ from $5.4 \Omega \cdot \text{cm}^2$ for pure LSCF cathode at 600°C [30].

Despite these promising results reported in the literature, the potential of the infiltration approach cannot be fulfilled when aqueous nitrate solutions are used to infiltrate the porous scaffolds, as they yield segregated and disconnected particles, leading to poor current collection and hence, insufficient performance. To address these issues, the use of polymeric precursors, which can form interconnected films upon decomposition, has been proposed as a more effective infiltration method [31, 32]. For example, $\text{La}_{0.8}\text{Sr}_{0.2}\text{MnO}_3\text{-Zr}_{0.84}\text{Y}_{0.16}\text{O}_2$ (LSM-YSZ) cathodes prepared by the infiltration of a polymeric LSM precursor into a porous YSZ scaffold has resulted in a polarization resistance as low as ca. $0.030 \Omega \cdot \text{cm}^2$ at 800°C [31]. This approach has also proven effective in the SOFC anode applications as polymeric Ni infiltration into porous YSZ scaffolds also exhibited very low polarization resistance of $0.1 \Omega \cdot \text{cm}^2$ at the same temperature [33]. Obviously, the LSM-YSZ and Ni-YSZ systems are generic examples of composite SOFC electrode materials, both of which hosting the electrochemical reactions exactly at their electrocatalyst-ionic conductor-gas triple phase boundaries. Meanwhile, the formation of MIEC-ionic conductor composites using the polymeric precursor method has the potential to yield electrodes with electrochemical performances exceeding those of the above-mentioned generic composites prepared by the same method. Nonetheless, this direction has not been thoroughly explored to date, i.e., only one paper reporting polymeric LSCF precursor infiltration into porous GDC scaffolds exists [24].

In the present work, we propose to fabricate two types of LSCF-GDC composite cathodes by making use of the polymeric precursor method. The first type of composite is prepared by infiltrating a polymeric LSCF precursor into a porous GDC scaffold to obtain an interconnected LSCF film with high surface area over the scaffold particles. In this case, due to the MIEC nature of the LSCF film, the oxygen reduction reaction is

considered to proceed in four steps, as depicted in Figure 3.1a. These steps are: adsorption of oxygen to the LSCF surface (Step I), reduction of adsorbed oxygen into oxygen ion and its insertion into the LSCF lattice (Step II), the transport of the oxygen ion through the LSCF lattice to the LSCF/GDC interface (Step III) and the transfer of the oxygen ion from the LSCF to the GDC lattice (Step IV). Similar oxygen reduction schemes have been proposed in the literature for MIEC cathodes, such as LSCF [34].

The second type of LSCF-GDC composite is proposed to be fabricated by infiltrating a mixture of polymeric LSCF and GDC precursors again into a porous GDC scaffold, for the first time in the literature. We anticipate that, upon heating, the ions present in the polymeric precursor mixture will segregate preferentially to form the LSCF and GDC phases. In this case, as depicted schematically in Figure 3.1b, an LSCF-GDC nanocomposite film will be formed on the grains of the porous GDC scaffold. A performance enhancement with respect to single phase GDC infiltration is expected due to the enhancement of the LSCF/GDC interfacial area and the consequent facilitation of oxygen ion transfer between the MIEC and the ionic conductor phases (Step IV). For both types of infiltration, the number of infiltration cycles were optimized to achieve the lowest polarization resistance possible at 700 °C.

3.3. Experimental

Experimental method is explained in this section.

3.3.1. Fabrication of the Dense GDC Electrolytes and Porous GDC Scaffold

10 mol% gadolinium-doped ceria powders ($\text{Ce}_{0.9}\text{Gd}_{0.1}\text{O}_{2-\delta}$, Praxair, >99.9%, with 6.5 m²/g specific surface area) were used in the manufacture of the dense ceramic electrolyte by uniaxial pressing (Carver Hydraulic Press, Wabash, IN, USA) at 180 MPa in a cylindrical stainless steel die with 15 mm diameter and approximately 1.5 mm height. The pellets were fired at 1400 °C for 4 hours at a heating rate of 3°C/min in a laboratory kiln (Nabertherm LHT02/17, Germany).

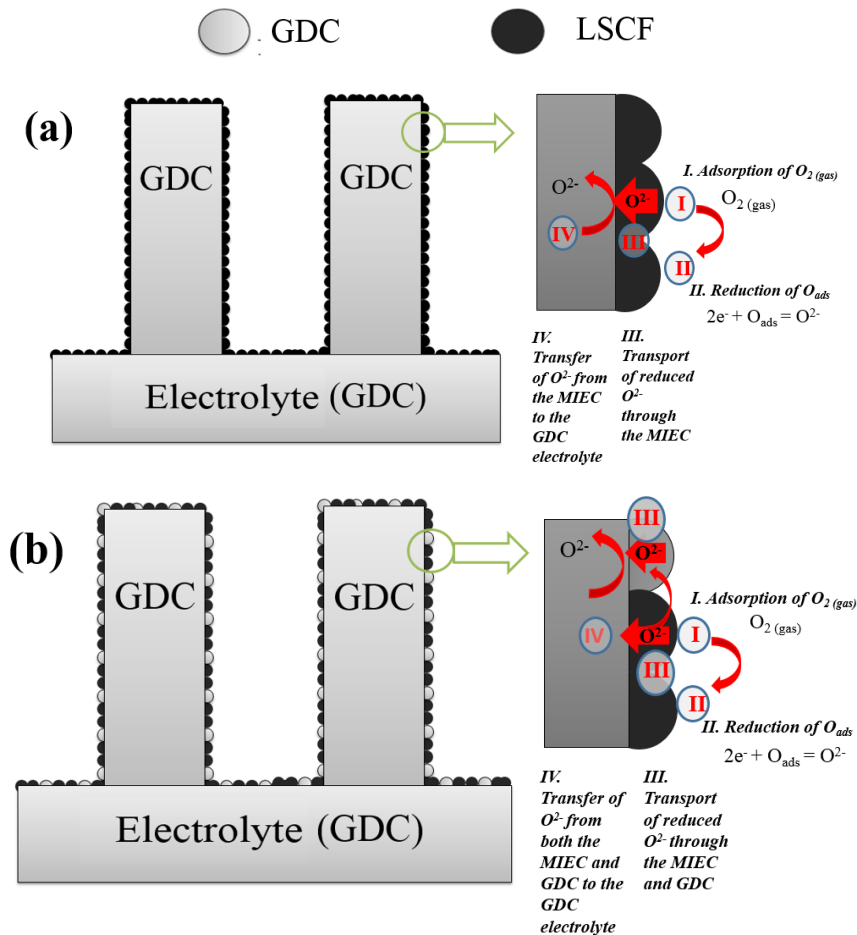


Figure 3.1. Schematic representation of proposed pathways of oxygen ions at cathode layers prepared by (a) single phase LSCF and (b) LSCF+GDC polymeric precursor solution infiltration into porous GDC scaffolds

3.3.2. Preparation of Polymeric Precursors and the Infiltration Process

Precursor solution of LSCF was prepared by dissolving proper amounts of lanthanum (III) nitrate hexahydrate (ALFA-AESAR >99.99%), strontium chloride hexahydrate (ALFA-AESAR >99%), cobalt (II) nitrate hexahydrate (ALFA-AESAR >97.7% min), iron (III) nitrate nonahydrate (ALFA-AESAR >99.99%) salts in deionized water at a molar ratio that would yield the of LSCF 6428 stoichiometry. The solutions were then mixed with ethylene glycol, ensuring that the molar ratio of the total metal salts to ethylene glycol was 0.02. Upon stirring at 70°C, all water evaporated, leaving a non-aqueous and more viscous solution which was then diluted by the addition of 2-butoxyethanol solution in 1:1 weight ratio, aiming to enhance the wetting properties of the precursor. A polymeric GDC precursor was also prepared from cerium nitrate

hexahydrate (ALFA-AESAR >99.5%) and gadolinium nitrate hexahydrate (Sigma-Aldrich >99.9%) salts following the same procedures. For LSCF+GDC infiltration, the polymeric LSCF and GDC precursor solutions were mixed in appropriate amounts that would yield a 60:40 volumetric LSCF to GDC ratio upon heat treatment.

Figure 3.2 summarizes the infiltration process. To form the porous GDC scaffold layer on the dense GDC electrolyte, a slurry consisting of GDC powder dispersed in α -terpineol and 2-butoxyethanol was prepared. The slurry was deposited on both sides of the dense GDC electrolyte by brush-painting before being partially sintered at 1000°C for 2 hours. The polymeric precursor solution of LSCF/LSCF+GDC was infiltrated into the previously formed porous GDC scaffold layers by brushing on both sides of the electrolyte. Heat treatment at 400°C on hot plate drove off volatiles thus completing one infiltration cycle. Different number of infiltration cycles (10-50) were carried out in this study to determine optimum loadings. Samples were encoded according to the infiltration precursor type and number of infiltration cycles. For example, LSCF 40X denotes 40 cycles of LSCF infiltration, while LSCF+GDC 30X represents 30 cycles of infiltration using a mixture of polymeric LSCF and GDC precursors.

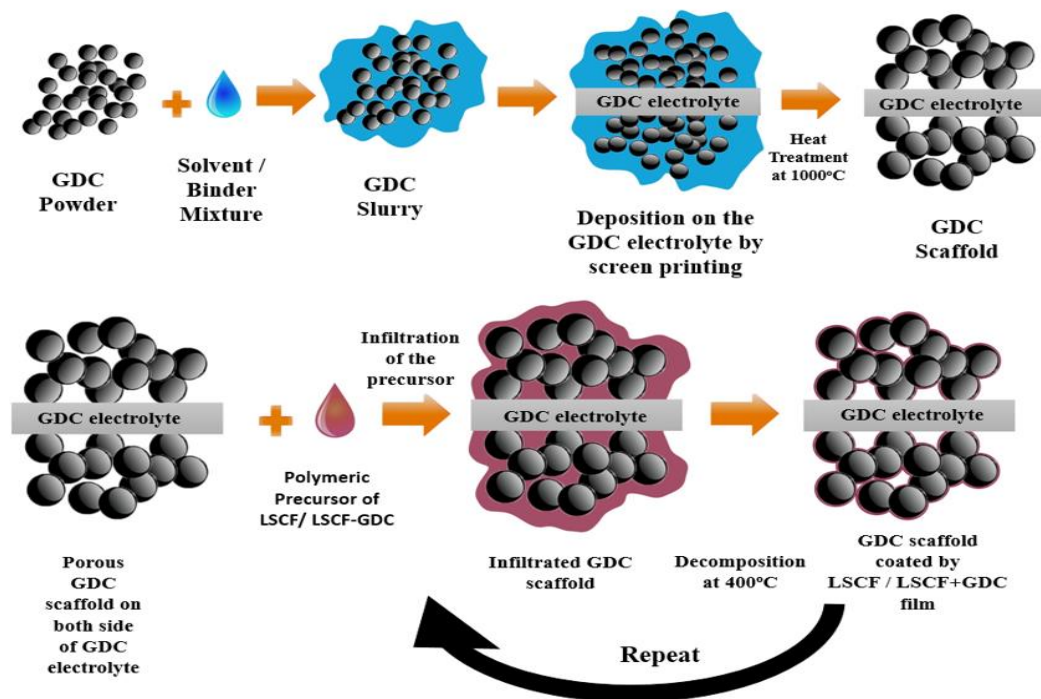


Figure 3.2. Schematic representation of experimental flow chart depicting the formation of the porous scaffold, and the infiltration of the scaffold multiple times to deposit nano sized LSCF or LSCF+GDC

3.3.3. Crystal Structure and Microstructure Analyses

Crystal structures of the composite cathodes were determined by x-ray diffraction (XRD- Panalytical X'Pert Pro, CuK α radiation). However, the interpretation of the composite cathodes, especially those prepared by LSCF+GDC infiltration into porous GDC scaffold is quite difficult, as it cannot be decided with acceptable certainty whether any cubic GDC peaks that are likely to appear, originate from the substrate, the porous scaffold or from the infiltrated polymeric precursor. To avoid such complications, the XRD analyses were performed on dried gels of LSCF and LSCF+GDC polymeric precursors calcined at 700 °C.

The microstructures and morphologies of the LSCF and LSCF+GDC infiltrated and non-infiltrated porous GDC scaffolds were examined by scanning electron microscope (SEM, Philips XL 30S FEG) using secondary electron imaging and the elemental compositions of the cathode layers were determined by energy dispersive x-ray spectroscopy (EDX) analysis.

3.3.4. Electrochemical Performance Analysis

For the evaluation of the electrochemical performance of the fabricated cathodes, an in-house Ag paste was brush-painted onto the cathode surfaces in order to form current collecting layers which were connected to Ag lead wires. Autolab (Metrohm M204 PGSTAT) instrument was used to analyze the electrochemical performance of the symmetrical half-cells by electrochemical impedance spectroscopy (EIS) at 500-700 °C, in stagnant air with an AC amplitude of 15 mV excitation voltage amplitude. Nova 2.1 software was used to fit the collected EIS data.

3.4. Results and Discussions

To determine the phases that the infiltration solutions form within the porous GDC scaffold, the dried gels of the LSCF and LSCF+GDC polymeric precursors were calcined at 700 °C and were subjected to x-ray diffraction (XRD) analyses. XRD patterns of these

powders show the presence of rhombohedral LSCF phase (PDF: 01-089-1268) in both cases (Figure 3.3). LSCF+GDC powder, also contains cubic GDC phase (PDF: 01-075-0161), as expected (Figure 3.3). Unidentified peaks with low intensities at $2\theta=25.3$, 35, 39 and 44° are also observed, indicating the presence of small amounts of impurity phases (Figure 3.3). In the literature, LSCF and LSCF-GDC thin films prepared by spray pyrolysis were also reported to have similar unidentified peaks [35-41]. For example, unidentified peaks were observed at $2\theta=35^\circ$ by Haider et al. [41], at $2\theta=25.5$ and 44° by Muller et al [35]. These peaks were, however, found to disappear upon thermal treatment above 700°C . Darbandi et al. [39] reported extra peaks at $2\theta=25.5$, 36, 44° which are traces of SrNO_3 which is commonly observed by other groups during LSCF formation [40].

As mentioned before, two different polymeric precursor solutions were used to infiltrate the porous GDC scaffold. Different numbers of infiltration cycles have been performed to ensure continuous coverage of the GDC particle surfaces of the porous scaffold with interconnected films of LSCF and LSCF+GDC, as opposed to discrete particles. Figure 3.4(a) depicts a representative cross-sectional scanning electron microscopy (SEM) image of a selected infiltrated sample (LSCF 40X), revealing the GDC electrolyte, porous GDC scaffold and Ag current collector layers. A good adherence between the porous GDC scaffold and the dense GDC electrolyte can be clearly observed with an approximate thickness of $65\text{-}75\ \mu\text{m}$. The SEM image of the non-infiltrated porous GDC scaffold layer is shown in Figure 3.4(b). Evidently, the porous GDC layer consists of grains and pores with uniformly distributed sizes, originating from partial sintering of the as-received GDC powder.

The microstructural characterization of the infiltrated composite cathodes were also performed in more detail before and after long-term (i.e., 100 hours) testing at 700°C to i) ensure that interconnected films are formed on the grains of the porous GDC scaffold, not discrete particles and ii) observe any significant microstructural changes that may take place upon prolonged exposure to the operating temperature (700°C). Both the LSCF and the LSCF+GDC infiltrated cathodes resemble the blank GDC scaffold microstructure and appear to be free of discrete particles (Figure 3.4 c, d). This suggests that the polymeric precursor infiltration results in interconnected film formation on the scaffold grains (Figure 3.4c, d). After long term stability test, microstructures do not appear to be significantly changed in LSCF (Figure 3.4e) and LSCF+GDC (Figure 3.4f) samples i.e. grain size, porosity and agglomeration.

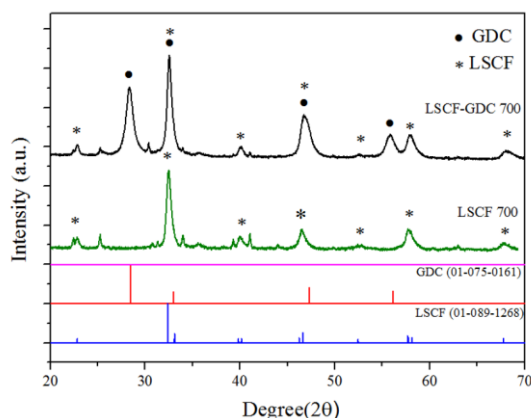


Figure 3.3. Schematic representation of experimental flow chart depicting the formation of the porous scaffold, and the infiltration of the scaffold multiple times to deposit nano sized LSCF or LSCF+GDC

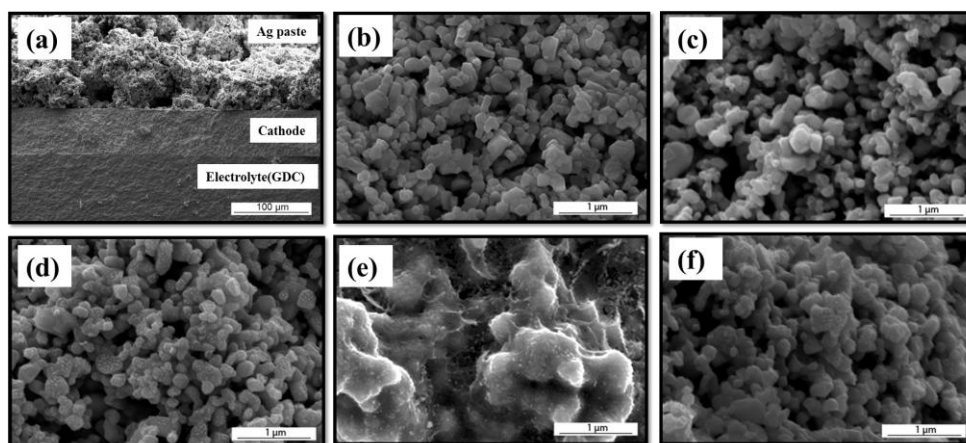


Figure 3.4. Scanning electron microscopy (SEM) images of fractured cross sections of (a) a representative LSCF+GDC infiltrated cathode (40x) also including the Ag current collector and the electrolyte, (b) a previously sintered porous GDC scaffold layer without any infiltration, (c) porous GDC scaffold infiltrated 45 times with LSCF precursor solution after annealing at 700°C for 2h, (d) porous GDC scaffold infiltrated 45 times by LSCF precursor solution and heat treated at 700°C for 100 hours, (e) porous GDC scaffold infiltrated 30 times with LSCF+GDC solution after annealing at 700°C for 2h, (f) porous GDC scaffold infiltrated 30 times by LSCF+GDC precursor solution and heat treated at 700°C for 100 hours.

Energy dispersive x-ray spectroscopy (EDX) analyses over the fractured cross section of samples were performed to track the variation of elemental concentration within the cathode layer after different infiltration cycles (Figure 3.5). As stated above, the infiltration solutions were prepared to yield the exact stoichiometries of $\text{La}_{0.6}\text{Sr}_{0.4}\text{Co}_{0.2}\text{Fe}_{0.8}\text{O}_{3-\delta}$ and $\text{Ce}_{0.9}\text{Gd}_{0.1}\text{O}_{2-\delta}$. Figure 3.5a shows the elemental percentage change of LSCF infiltrated cathode with increasing number of infiltration cycles. The relative amounts of Ce and Gd decreases while those of La, Sr, Co and Fe increases with

increasing number of infiltration cycles, which is expected (Figure 3.5a) Increasing the number of infiltration cycles cause a fast increase in the Fe content, and a slower increase in the relative amounts of other elements (i.e. La, Sr, Co), as dictated by the LSCF stoichiometry.. In the case of LSCF+GDC infiltration (Figure 3.5b), increasing the number of infiltration cycles leads to an enrichment of the electrocatalyst elements as expected, but this time to a lesser extent due to the GDC content of infiltrating solution.

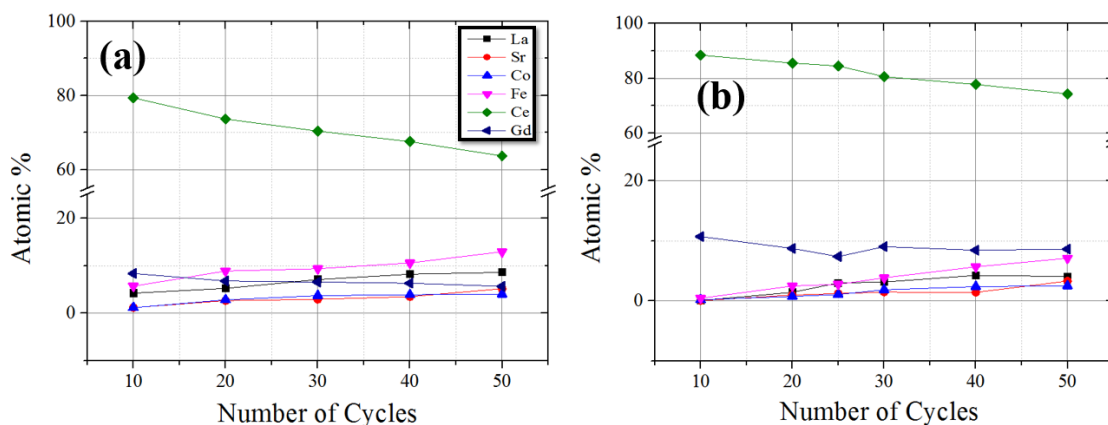


Figure 3.5. Relative amounts of La, Sr, Co, Fe, Ce and Gd elements determined by energy dispersive X-ray spectroscopy (EDX) measurements performed at the middle part of the cathode layers prepared by (a) LSCF and (b) LSCF+GDC infiltration into porous GDC scaffolds.

The electrochemical performance of the infiltrated electrodes were determined by electrochemical impedance spectroscopy (EIS) measurements of the symmetrical half-cells at 500-700 °C, in stagnant air. Since the thermal history of the infiltrated electrodes may have a significant impact on the electrochemical performance, the heat treatments that the infiltrated cathodes had been subjected to at the time of measurement are described in detail in Figure 3.6. Here, the heating regime consists of five stages and the EIS measurements are collected at every 50 °C when cooling down from 700 °C (Stage IV) and intermittently upon long-term exposure to 700 °C (Stage V).

Nyquist and Bode plots of the EIS data collected at 700°C from the cathodes prepared by 10-50 cycles of polymeric precursor infiltration are shown in Figure 3.7. The equivalent circuit models used to fit the EIS data are also provided as insets in the Nyquist plots (Figure 3.7). Curve fits using the related equivalent circuits were achieved with negligible error ($\chi^2 \sim 10^{-4}$). The series resistances present in the equivalent circuits are denoted as “Rs” and are obtained from the intercept of the impedance response at high frequency. This contribution is related to the electrolyte resistance and is slightly variable

from sample to sample due to the variations in the thickness of the electrolyte substrate. The size of the impedance arc (R_1 or the sum of R_1 and R_2 in one case) refers to the polarization resistances of the two identical electrodes. Hence, the polarization resistance value should be divided by two to find the area specific polarization resistance per each infiltrated cathode (ASR_{cathode}).

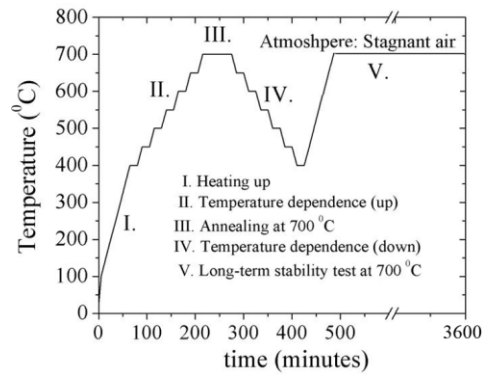


Figure 3.6. Heating/cooling schedule followed during impedance spectroscopy measurements

Measured impedance data for samples infiltrated 10 to 45 times show a similar type of EIS response, i.e., a single semi-circle which corresponds to an equivalent circuit consisting of electrolyte resistance (R_s) coupled in series with a polarization resistance connected in parallel to a constant phase element unit (R_1/Q_1) (Figures 3.7a-f). Evidently, the general tendency is that an increase in the number of LSCF infiltration cycles brings about reductions in the polarization resistance (Figures 3.7a-f). For example, the polarization resistance per electrode decreases from $9.04 \Omega \cdot \text{cm}^2$ down to $0.71 \Omega \cdot \text{cm}^2$ at 700°C upon an increase in the number of LSCF infiltration cycles from 0 to 40 (Figures 3.7a-f). This is expected since the increased number of LSCF infiltration cycles enhances the coverage of the GDC grain surfaces of the porous scaffold with the electrocatalytic LSCF film providing more LSCF/gas and LSCF/GDC interfacial area. On the other hand, no further reductions in the polarization resistance is observed when the number of infiltration cycles is increased from 40 to 45 (Figures 3.7e, f and g). Furthermore, an increase in the polarization resistance up to $1.57 \Omega \cdot \text{cm}^2$ concomitant with the appearance of a low frequency semi-circle represented with another resistor/constant phase element in the equivalent circuit diagram (R_2/Q_2) in the 50x LSCF electrode is evident (Figure 3.7g).

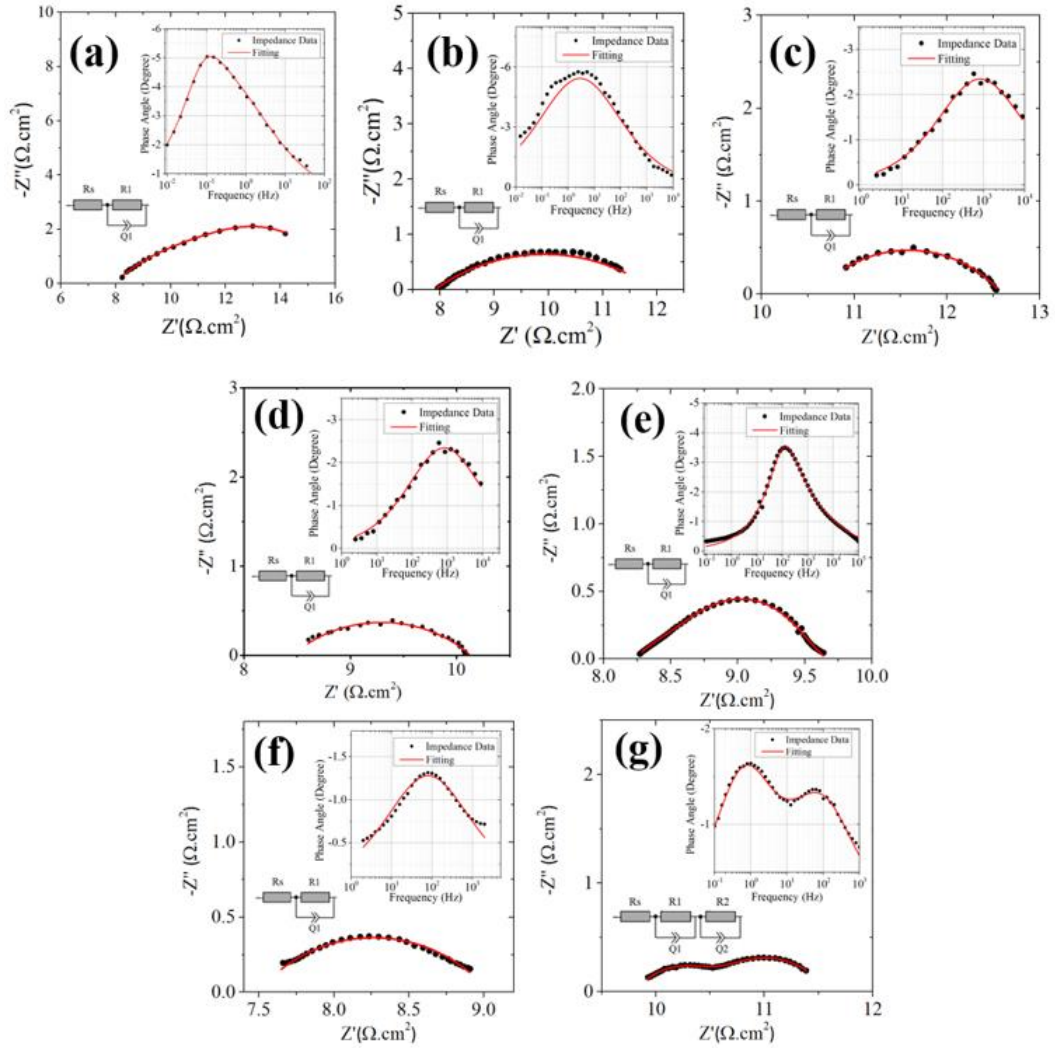


Figure 3.7. Impedance spectra obtained from cathodes prepared by a) 10x b) 20x c) 30x d) 35x e) 40x f) 45x g) 50x LSCF infiltration into porous GDC scaffolds. Measurements were conducted on symmetrical half cells at 700°C, in air. The equivalent circuit models used to fit the obtained impedance data are provided in insets.

In the literature the low frequency semi-circle has been attributed either to concentration polarization resulting from the insufficient porosity [42,43], or to the chemical capacitance originating from the oxygen insertion into the MIEC lattice and the consequent changes in the oxidation states of the transition metal cations within the perovskite structure [42-47]. Since it is well known that the latter process is temperature dependent and the former is not [42,45], the EIS measurements of the symmetrical cell with 50x LSCF electrodes have been carried out at different temperatures to determine the physical cause of the low-frequency arc observed in these cathodes. The EIS data obtained at 600, 650 and 700 °C are represented in the form of a Bode plot in Figure 3.8a to clearly show the effect of temperature on the high and low frequency processes. Here,

the imaginary part of the impedance remains unchanged at low-frequency range (at around 0.4 Hz) but is found to increase with decreasing temperature at high frequencies (at around 30 Hz, Figure 3.8a). The temperature dependence of the area specific resistances of the high and low frequency processes (denotes as R1 and R2 respectively), their sum (total polarization resistance) determined from the equivalent circuit fitting of the EIS response of LSCF 50x ($R_1 + R_2$) are given in Figure 3.8b. Evidently, R1 obtained from LSCF 50x has a strong dependence on temperature, while R2 remains nearly unchanged (Figure 3.8b). The temperature independent nature of R2 suggests that the low frequency process is concentration polarization, likely caused by the overloading of the porous GDC scaffold with infiltrated LSCF, thereby eliminating porosity required for the transport of oxygen gas to the electrochemically active surfaces.

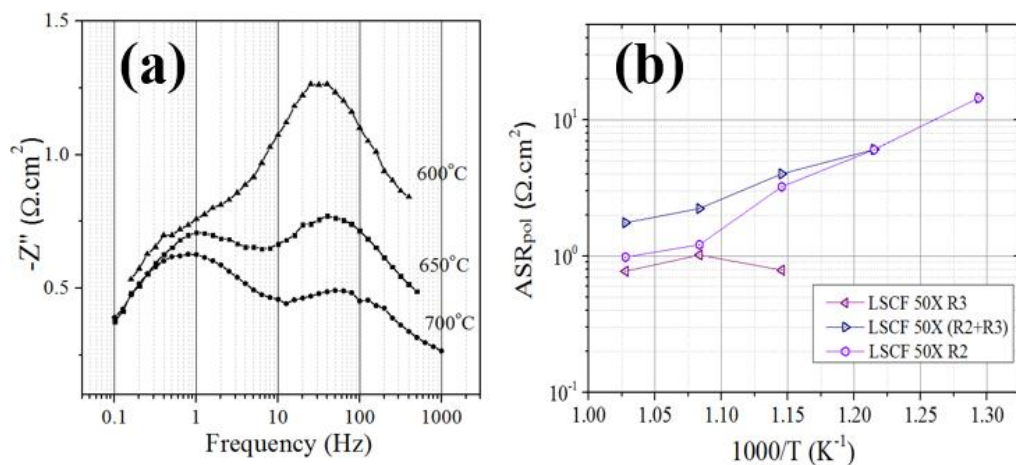


Figure 3.8. a) Bode plots showing the impedance response of LSCF (50x) infiltrated symmetrical half-cell measured at 600, 650 and 700°C. (b) Temperature dependence of the cathode polarization resistance of infiltrated LSCF (50x) sample, also showing the individual contributions of the high and low frequency resistance components (i.e., R2 and R3) to total resistance. Impedance spectroscopy measurements were performed on symmetrical half-cells cells, in air.

In order to examine the performance of the LSCF infiltrated cathodes at intermediate temperatures (500-700°C), EIS measurements were performed in the range of 500-700°C temperature range. Temperature dependences of the total area specific polarization resistance (ASR) values of infiltrated LSCF+GDC cathodes are plotted as $ASR_{cathode}$ vs $1000/T$ (Figure 3.9).

The data collected from the symmetrical half-cells with blank porous scaffold layers with only Ag current collectors is also included to serve as a reference (Figure 3.9).

$ASR_{cathode}$ consistently increases with decreasing measurement temperature (700 down to 500°C) and decreases with increasing the number of LSCF infiltration cycles. Similar slopes referring to similar activation energies in the range of 0.81-1.08 eV are visible for all samples, except for LSCF 50x, which exhibits a weaker temperature dependence due to the presence of the temperature independent low frequency process attributed to concentration polarization herein (Table 3.1).

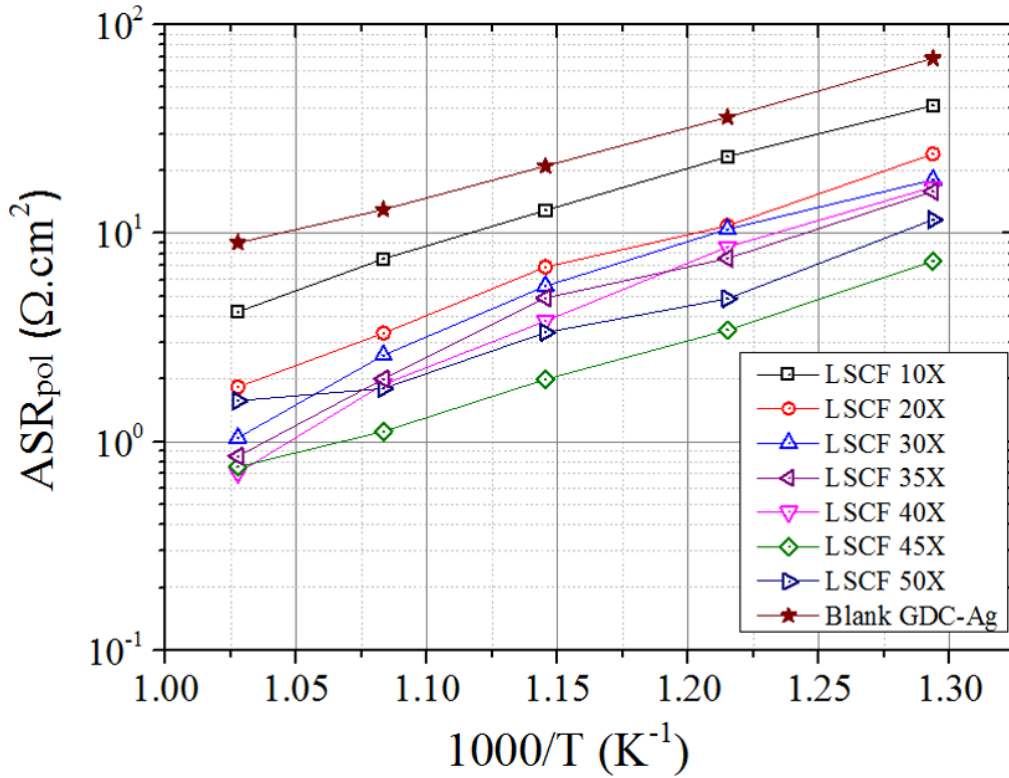


Figure 3.9. (a) Bode plots showing the impedance response of LSCF (50x) infiltrated symmetrical half-cell measured at 600, 650 and 700°C. (b) Temperature dependence of the cathode polarization resistance

Su et al [48] defined a promotion factor for infiltrated electrodes as $\epsilon = R_{p_{blank}}/R_{p_{inf}}$ where $R_{p_{blank}}$ is the polarization resistance of the non-infiltrated cathode and $R_{p_{inf}}$ is the polarization resistance of infiltrated cathode to examine the success of infiltration. Tomov et al [43] systematically grouped different studies [49-51] based on their promotion factor (ϵ) which varies from 1.30 to 3.66 for GDC infiltration into LSCF scaffold of different loadings. The ϵ values measured in this study varies between 1.99 and 12.3 for the LSCF infiltrated cathodes, suggesting that the polymeric precursor method is very effective for infiltration purposes

Table 3.1. Cathode polarization resistance values (per electrode) and the corresponding activation energies of LSCF infiltrated cathodes for prepared by different number of infiltration cycles measured at 700 °C

Sample Name	Ea (eV)	Rp at 700° C (per electrode) ($\Omega\cdot\text{cm}^2$)
Blank GDC -Ag Collector	0.74	9.04
LSCF 10x	0.81	4.2
LSCF 20x	0.89	1.83
LSCF 30x	0.99	1.04
LSCF 35x	1.00	0.85
LSCF 40x	1.08	0.71
LSCF 45x	0.95	0.73
LSCF 50x	0.73	1.57

Evolution of the EIS response of the polymeric LSCF+GDC precursor infiltrated composite cathodes with varying number of infiltration cycles is shown in Figure 3.10. Only one depressed semi-circle is observed in the Nyquist plots of all samples. Thus, the proposed equivalent circuit used for fitting the curve has two resistance components R_s (electrolyte resistance) and R_1 (polarization resistance). In the circuit, R_s represents the ohmic resistance of the GDC electrolyte and R_1/Q_1 elements represent electrode processes. Resembling the case of LSCF infiltration, increasing the number of LSCF+GDC infiltration cycles from 10x to 30x brings about a significant reduction in the polarization resistance values, while further increasing the number of infiltration cycles has negative effect on the electrochemical performance at 700 °C. Polarization resistances as low as $\sim 0.47 \Omega\cdot\text{cm}^2$ per electrode at 700 °C are obtained in the case of 30x LSCF+GDC infiltration (Figure 3.10c). The ϵ values varying between 3.72 and 19.23 obtained in the case of LSCF+GDC infiltrated samples reflect the superiority of these cathodes over those prepared by LSCF infiltration. The reason for the lower value of the lowest possible polarization resistance value obtained in the case of LSCF+GDC infiltration in comparison to that obtained by LSCF infiltration is the enhancement of the electrocatalyst/ionic conductor interfacial area and thus facilitated oxygen ion transfer to the electrolyte, as proposed in Figure 3.1b. The increase in the polarization resistance observed upon exceeding the optimum number of infiltration cycles (evidently 30X in this case) is not accompanied by the appearance of a concentration polarization related low-frequency semi-circle (Figure 3.10d). A possible explanation lies in the formation of a very thick LSCF+GDC coating on the GDC grains, which increases the oxygen ion transport distances, leading to increased resistances. After excessive loading via

infiltration similar performance losses were also observed in other studies which attributed the losses to the formation of clusters and thick coating that reduced the number of active sites [52,53].

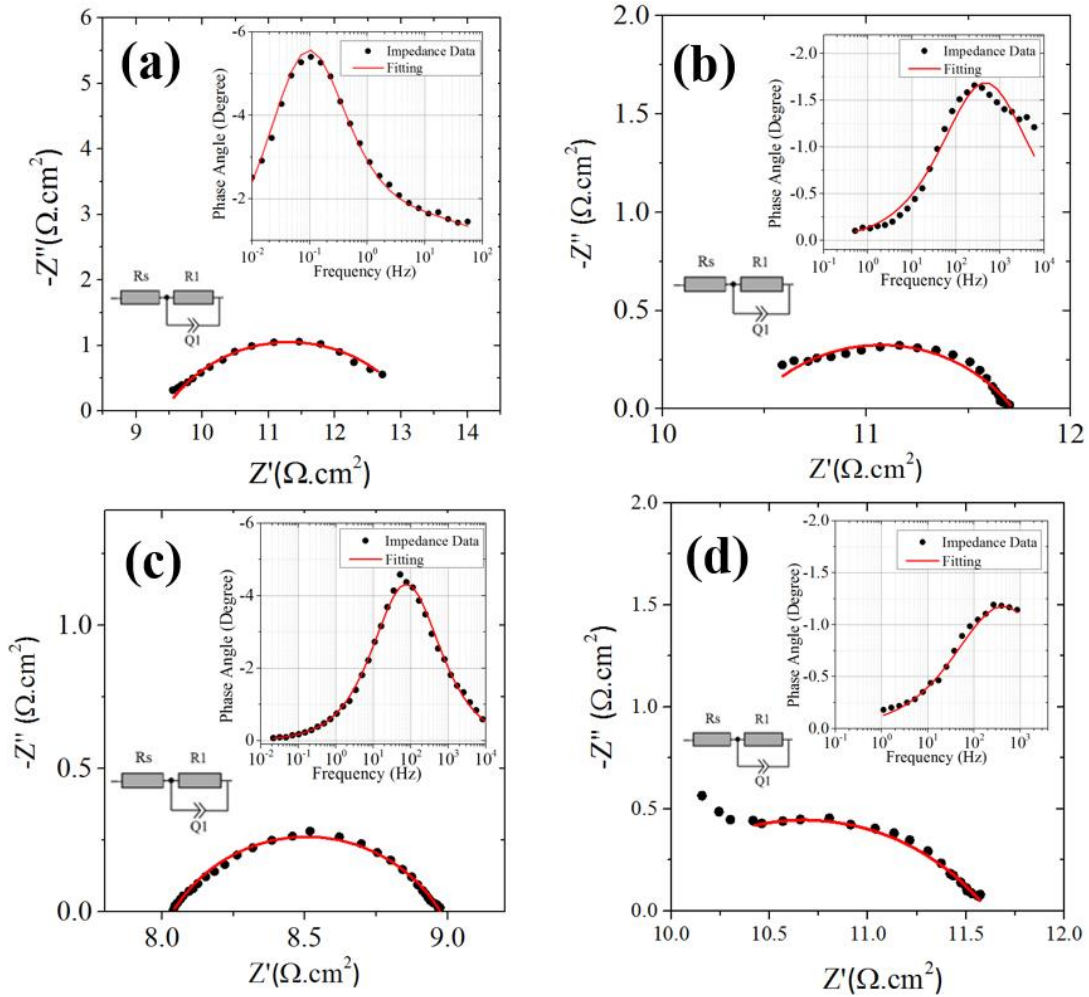


Figure 3.10. Impedance spectra obtained from cathodes prepared by a) 10x b) 20x c) 30x d) 40x LSCF+GDC infiltration into porous GDC scaffolds. Measurements were conducted on symmetrical half cells at 700°C in air. The equivalent circuit models used to fit the obtained impedance data are provided in insets.

The variation of the area specific resistances (ASR) of LSCF+GDC infiltrated cathode samples with temperature for different number of infiltration cycles are shown in Figure 3.11. Ag current collector data are included for comparison. These results revealed that increasing the LSCF+GDC infiltration cycles from 10x to 30x, the electrochemical performances of cathodes was enhanced regardless of measurement temperature. Similar activation energies in the range of 0.86-0.91 eV are visible for all samples (Table 3.2).

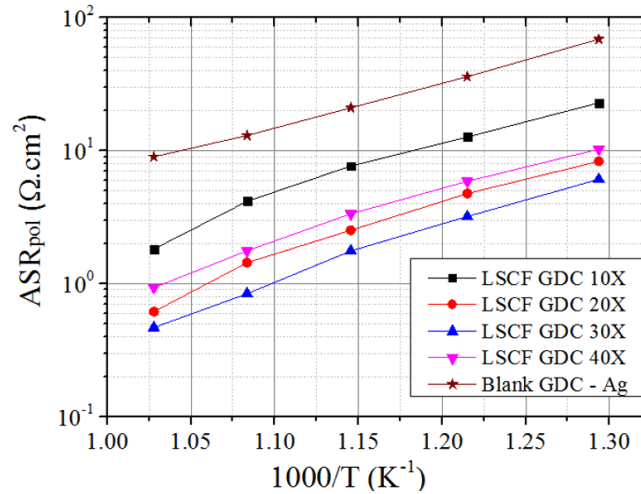


Figure 3.11. Temperature dependence of the cathode polarization resistances obtained from the impedance spectroscopy measurements of symmetrical half-cell with cathodes prepared by different amounts of (from 10x to 40x) LSCF+GDC infiltration into porous GDC scaffolds. Cathode polarization resistance of blank porous GDC layer brushed with silver current collector was also added for comparison.

Table 3.2. Cathode polarization resistance values (per electrode) and the corresponding activation energies of LSCF infiltrated cathodes for prepared by different number of infiltration cycles measured at 700 °C

Sample Name	Ea (eV)	Rp at 700° C (per electrode) (Ω.cm ²)
Blank GDC -Ag Collector	0.74	9.04
LSCF GDC 10x	0.86	1.82
LSCF GDC 20x	0.90	0.61
LSCF GDC 30x	0.91	0.47
LSCF GDC 40x	0.88	0.93

The long-term stability of the electrochemical performances of SOFC cathodes prepared by LSCF and LSCF+GDC infiltration into porous GDC scaffolds is tested by intermittently performing EIS measurements upon long-term exposure to 700 °C, which corresponds to the Stage V in Figure 3.6. As shown in Figure 3.12, a significant increase in the $ASR_{cathode}$ (from 0.73 $\Omega.cm^2$ to 2.3 $\Omega.cm^2$) takes place with time for single phase LSCF infiltrated cathode. The preliminary 60 hours of tests indicate a significantly improved longevity in the case of LSCF+GDC infiltrated cathodes (Figure 3.12). In the literature, it has been reported that the addition of a secondary phase has been reported to inhibit the grain growth and hence the loss of the MIEC/gas interfacial area in the case of conventionally prepared samples [54,55]. The addition of GDC to the LSCF coatings

formed on the grains of the porous GDC scaffolds is considered to induce such a microstructural stabilization in the present case as well. More detailed microstructural analyses via transmission electron microscopy required to test this hypothesis are currently underway.

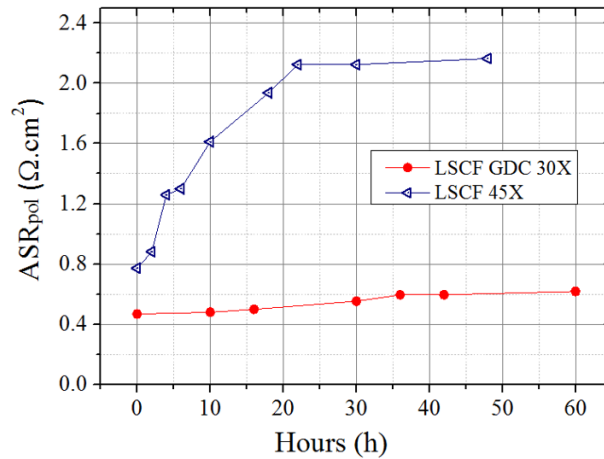


Figure 3.12. Long term stability test results (polarization resistance measured at 700°C) of the symmetrical cells with LSCF 45x and LSCF+GDC 30x infiltrated as a function of dwell time

3.5. Conclusion

Dense GDC electrolyte pellets fired to sufficiently high density were coated by screen printing to form a porous GDC layer on both sides to provide a porous GDC scaffold into which polymeric precursor solutions of LSCF and LSCF+GDC were successfully infiltrated by a multistep process. SEM analysis showed that, after infiltration, no agglomerates formed in any of the samples, suggesting that polymeric LSCF and LSCF+GDC precursors could coat the GDC particles in a uniform and effective manner. EIS measurements of the samples between 500 and 700°C clearly showed that increasing the amount of infiltration cycles enhanced the electrochemical performance up until 45x for LSCF and 30x for LSCF+GDC infiltration. Any further LSCF infiltration cycle only degraded the ASR manifesting itself by a low frequency arc in the Nyquist diagrams, interpreted as a result of slowed mass transport of oxygen gas within the porous electrode. Loss of electrochemical performance after excessive LSCF+GDC infiltration was attributed to the formation of relatively thicker LSCF+GDC coatings on the grains of the porous GDC scaffold that brings about longer pathway for

reduced oxygen ion transport from cathode to electrolyte. Comparison of the long-term electrochemical testing of the LSCF and LSCF+GDC infiltrated cathodes revealed that LSCF+GDC infiltration resulted in i) a higher electrochemical performance, attributed to enhanced LSCF/GDC interfacial area and ii) a more stable polarization resistance at 700°C, likely originating from the inhibition of the grain growth in the LSCF phase by the GDC particles formed within the infiltrated coating. These results proved that precursor infiltration method is a very promising approach for the fabrication of high performance cathodes for SOFC applications in intermediate temperatures.

Acknowledgements

Authors would like to thank different labs in both Izmir Institute of Technology and Gebze Technical University for their helps during analysis of samples. This project is supported by Izmir Institute of Technology (BAP project numbers: 2016IYTE01 and 2017IYTE08).

3.6. References

- [1] Kalinci, Y.; Dincer, I. *International Journal of Hydrogen Energy* **2018**, *43*(11), 5795–5807.
- [2] Sındıraç, C.; Akkurt, S. *International Journal of Hydrogen Energy* **2016**, *41*(40), 18157–18165.
- [3] Yildiz, B.; Kazimi, M. *International Journal of Hydrogen Energy* **2006**, *31*(1), 77–92.
- [4] Perry, M. L.; Fuller, T. F. *Journal of The Electrochemical Society* **2002**, *149*(7), 569-567.
- [5] Nie, L.; Liu, Z.; Liu, M.; Yang, L.; Zhang, Y.; Liu, M. *Journal of Electrochemical Science and Technology* **2010**, *1*(1), 50–56.
- [6] Buyukaksoy, A.; Birss, V. *ECS Transactions* **2015**, *66*(2), 267–274.
- [7] Chen, C.; Bouwmeester, H. J. M.; Kruidhof, H.; Elshof, J. E. T.; Burggraaf, A. *J. J. Mater. Chem.* **1996**, *6*(5), 815–819.
- [8] Bohac, P.; Gauckler, L. *Solid State Ionics* **1999**, *119*(1-4), 317–321.

- [9] Sun, C.; Hui, R.; Roller, J. *Journal of Solid State Electrochemistry* **2009**, *14*(7), 1125–1144.
- [10] Steele, B. C. H. *Solid State Ionics* **2000**, *129*, 95–110.
- [11] Li, Z.-P.; Toshiyuki, M.; Auchterlonie, G. J.; Zou, J.; John, D. *ACS Applied Materials & Interfaces* **2011**, *3*(7), 2772–2778.
- [12] Steele, B. C. H.; Heinzl, A. *Nature* **2001**, *414*(6861), 345–352.
- [13] Buyukaksoy, A.; Birss, V. I. *Journal of Power Sources* **2016**, *307*, 449–453.
- [14] Wang, W.; Mogensen, M. *Solid State Ionics* **2005**, *176*(5-6), 457–462.
- [15] Steele, B. *Solid State Ionics* **1995**, *75*, 157–165.
- [16] Gauckler, L. J.; Beckel, D.; Buegler, B. E.; Jud, E.; Muecke, U. P.; Prestat, M.; Rupp, J. L.; Richter, J. *CHIMIA International Journal for Chemistry* **2004**, *58*(12), 837–850.
- [17] Murray, E. P.; Sever, M J.; Barnett, S. A. *Solid State Ionics* **2002**, *148*(1-2), 27–34.
- [18] Barfod, R.; Hagen, A.; Ramousse, S.; Hendriksen, P. V.; Mogensen, M. *Fuel Cells* **2006**, *6*(2), 141–145.
- [19] He, H.; Huang, Y.; Regal, J.; Boaro, M.; Vohs, J. M.; Gorte, R. J. *Journal of the American Ceramic Society* **2004**, *87*(3), 331–336.
- [20] Shah, M.; Barnett, S. *Solid State Ionics* **2008**, *179*(35-36), 2059–2064.
- [21] Jiang, S. P. *Journal of Material Science* **2008**, *43*, 6799–6833.
- [22] Murray, E. P.; Barnett, S. A. *Solid State Ionics* **2001**, *143*(3-4), 265–273
- [23] Gorte, R. J.; Park, S.; Vohs, J. M.; Wang, C. *Advanced Materials* **2000**, *12*(19), 1465–1469.
- [24] Chrzan, A.; Karczewski, J.; Gazda, M.; Szymczewska, D.; Jasinski, P. *Journal of the European Ceramic Society* **2017**, *37*(11), 3559–3564.
- [25] Jiang, S. P. *International Journal of Hydrogen Energy* **2012**, *37*(1), 449–470.
- [26] Samson, A.; Søgaard M.; Knibbe, R.; Bonanos, N. *Journal of The Electrochemical Society* **2011**, *158*(6), B650–B659.
- [27] Liu, Y.; Wang, F.; Chi, B.; Pu, J.; Jian, L.; Jiang, S. P. *Journal of Alloys and Compounds* **2013**, *578*, 37–43.

- [28] Shah, M.; Voorhees, P. W.; Barnett, S. A. *Solid State Ionics* **2011**, *187*(1), 64–67.
- [29] Kim, J. H.; Kim, H. *Ceramics International* **2012**, *38*(6), 4669–4675.
- [30] Chen, J.; Liang, F.; Chi, B.; Pu, J.; Jiang, S. P.; Jian, L. *Journal of Power Sources* **2009**, *194*(1), 275–280.
- [31] Buyukaksoy, A.; Petrovsky, V.; Dogan, F. *Journal of The Electrochemical Society* **2012**, *159*(6), B666-B669
- [32] Lou, X.; Liu, Z.; Wang, S.; Xiu, Y.; Wong, C.; Liu, M. *Journal of Power Sources* **2010**, *195*(2), 419–424.
- [33] Buyukaksoy, A.; Kammampata, S. P.; Birss, V. I. *Journal of Power Sources* **2015**, *287*, 349–358.
- [34] Wang, Z.; Peng, R.; Zhang, W.; Wu, X.; Xia, C.; Lu, Y. *Journal of Materials Chemistry A* **2013**, *1*(41), 12932.
- [35] Muller, G.; Ringuede, A.; Laberty-Robert, C. *Journal of Materials Chemistry A* **2014**, *2*(18), 6448.
- [36] Xi, X.; Kondo, A.; Kozawa, T.; Naito, M. *Advanced Powder Technology* **2016**, *27*(2), 646–651.
- [37] Ghosh S; Dasgupta S. *Materials Science-Poland* **2010**, *28*(2)
- [38] Leng, Y.; Chan, S.; Liu, Q. *International Journal of Hydrogen Energy* **2008**, *33*(14), 3808–3817.
- [39] Darbandi, A. J.; Hahn, H. *Solid State Ionics* **2009**, *180*(26-27), 1379–1387.
- [40] Beckel, D.; Dubach, A.; Grundy, A. N.; Infortuna, A.; Gauckler, L. J. *Journal of the European Ceramic Society* **2008**, *28*(1), 49–60.
- [41] Haider, M. A.; McIntosh, S. *Journal of The Electrochemical Society* **2011**, *158*(9).
- [42] Molero-Sánchez, B.; Addo, P.; Buyukaksoy, A.; Paulson, S.; Birss, V. *Faraday Discussions* **2015**, *182*, 159–175.
- [43] Tomov, R. I.; Mitchell-Williams, T.; Gao, C.; Kumar, R. V.; Glowacki, B. A. *Journal of Applied Electrochemistry* **2017**, *47*(5), 641–651.
- [44] Dusastre, V.; Kilner, J. *Solid State Ionics* **1999**, *126*(1-2), 163–174.
- [45] Molero-Sánchez, B.; Addo, P.; Buyukaksoy, A.; Birss, V. *Journal of The Electrochemical Society* **2017**, *164*(10).

- [46] Wei, B.; Lü, Z.; Wei, T.; Jia, D.; Huang, X.; Zhang, Y.; Miao, J.; Su, W. *International Journal of Hydrogen Energy* **2011**, 36(10), 6151–6159.
- [47] Liu, J.; Co, A. C.; Paulson, S.; Birss, V. I. *Solid State Ionics* **2006**, 177(3-4), 377–387.
- [48] Su, F.; Zhang, Y.; Ni, M.; Xia, C. *International Journal of Hydrogen Energy* **2014**, 39(6), 2685–2691.
- [49] Chen, J.; Liang, F.; Chi, B.; Pu, J.; Jiang, S. P.; Jian, L. *Journal of Power Sources* **2009**, 194(1), 275–280.
- [50] Nie, L.; Liu, M.; Zhang, Y.; Liu, M. *Journal of Power Sources* **2010**, 195(15), 4704–4708.
- [51] Zhao, E.; Jia, Z.; Zhao, L.; Xiong, Y.; Sun, C.; Brito, M. E. *Journal of Power Sources* **2012**, 219, 133–139.
- [52] Liu, M.; Ding, D.; Blinn, K.; Li, X.; Nie, L.; Liu, M. *International Journal of Hydrogen Energy* **2012**, 37(10), 8613–8620.
- [53] Barbucci, A.; Carpanese, M.; Reverberi, A. P.; Cerisola, G.; Blanes, M.; Cabot, P. L.; Viviani, M.; Bertei, A.; Nicoletta, C. *Journal of Applied Electrochemistry* **2008**, 38(7), 939–945.
- [54] Chen, J.; Liang, F.; Yan, D.; Pu, J.; Chi, B.; Jiang, S. P.; Jian, L. *Journal of Power Sources* **2010**, 195(16), 5201–5205.
- [55] Fu, C.; Sun, K.; Zhang, N.; Chen, X.; Zhou, D. *Electrochimica Acta* **2007**, 52(13), 4589–4594.

CHAPTER 4

LOWERING THE SINTERING TEMPERATURE OF SOLID OXIDE FUEL CELL ELECTROLYTES BY INFILTRATION

Can Sındıraç¹, Seda Çakırlar², Aligül Büyükaksoy^{3,4*}, Sedat Akkurt¹,

¹ Izmir Institute of Technology, Department of Mechanical Engineering, Urla, İzmir, 35433 Turkey

² Izmir Institute of Technology, Department of Chemical Engineering, Urla, İzmir, 35433 Turkey

³ Gebze Technical University, Department of Materials Science and Engineering, Gebze, Kocaeli 41400, Turkey

⁴ Gebze Technical University, Institute of Nanotechnology, Gebze, Kocaeli 41400, Turkey

*Corresponding Author:

E-mail: sedatakkurt@iyte.edu.tr (S.Akkurt) Ph: +90 (262) 750 6705

This chapter is published in Journal of the European Ceramic Society

(DOI: 10.1016/j.jeurceramsoc.2018.09.029)

4.1. Abstract

A dense electrolyte with a relative density of over 95% is vital to prevent gas leakage and thus the achievement of high open circuit voltage in solid oxide fuel cells (SOFCs). The densification process of ceria based electrolyte requires high temperatures heat treatment (i.e. 1400-1500 °C). Thus, the minimum co-sintering temperatures of the anode-electrode bilayers are fixed at these values, resulting in coarse anode microstructures and consequently poor performance. The main purpose of this study is to densify gadolinia doped ceria (GDC), a common SOFC electrolyte, at temperatures lower than 1400°C. By this aim, an approach involving the infiltration of polymeric precursors

into porous electrolyte scaffolds, a method commonly used for composite SOFC electrodes, is proposed. By infiltrating polymeric precursors of GDC into porous GDC scaffolds, a reduction in the sintering temperature by at least 200°C is achieved with no additives that might affect the electrical properties. Energy dispersive x-ray spectroscopy line scan analyses performed on porous GDC scaffolds infiltrated by a marker solution (polymeric FeOx precursor in this case) reveals a homogeneous infiltrated phase distribution, demonstrating the effectiveness of polymeric precursors.

Keywords: SOFC, GDC, electrolyte, microstructure, densification, infiltration

4.2. Introduction

Excessive use of fossil fuels and their effect on global warming requires the search for clean alternative energy sources [1-2]. Solid oxide fuel cells (SOFCs) have been attracting attention from researchers because of their ability to convert chemical energy into electrical energy without combustion [3-4]. Although SOFCs are one of the cleanest and most efficient power sources, the maximum power density achievable by these devices must be enhanced. This way their cost per power generated can be minimized. [5-8]

SOFCs are operated at high temperatures (600-1000 °C) by having a constant supply of hydrogen and oxygen at the anode and cathode sides, respectively. Obviously, the two gases should not be intermixed to i) obtain high open circuit voltage and ii) avoid violent burn out [9-13]. This is achieved by having a dense gas tight ceramic electrolyte. In order to be perfectly gas leak-free, a 95% relative density is the generally accepted target. To achieve this relative density value, the most commonly used electrolytes, i.e., yttria stabilized zirconia (YSZ) and gadolinia doped Ceria (GDC) must be sintered at temperatures exceeding 1400°C [14-16]. This is problematic because the manufacturing process of SOFC requires that both electrolyte and electrode layers be sintered together while in contact which is known as co-sintering [17].

Consequently, the sintering temperature of the anode is set at the densification temperature of the electrolyte. The high co-sintering temperatures result in coarse anode

microstructures, which correspond to short triple phase boundary length and thus, poor anode performance [16-20].

Another drawback related to the sintering of gadolinium doped ceria specifically, at high temperatures is the reduction of CeO_2 to Ce_2O_3 due to unstable valance states of cerium from Ce^{+4} to Ce^{+3} which may cause the formation of micro-cracks [21-25]. Also, sintering the SOFC electrolytes at temperatures lower than 1400°C is also beneficial due to energy savings from lower temperature kiln heating.

The infiltration method has previously been proposed to form composite anode and cathode layers [25-29]. Use of polymeric $\text{La}_{0.8}\text{Sr}_{0.2}\text{MnO}_3$ (LSM) [25] and Ni [26, 27] precursors to infiltrate porous yttria stabilized zirconia (YSZ) scaffolds yielded LSM-YSZ and Ni-YSZ composite cathodes and anodes respectively with microstructures consisting of interconnected infiltrated films on the surfaces of YSZ particles. This, in turn, resulted in very promising electrode polarization resistances of $0.030 \Omega\cdot\text{cm}^2$ [25] and $0.1 \Omega\cdot\text{cm}^2$ [26, 27] at 800°C in the cathode and anode cases respectively.

In the present study, the use of the infiltration technique is proposed for low temperature densification of GDC electrolytes, for the first time in the literature. Here, a three-stage process is proposed, as depicted in Figure 4.1. First, a GDC pellet is pre-sintered at a low temperature (1000°C) to allow for the neck formation among the particles and obtain just enough strength for handling while retaining a large amount of porosity. The pre-sintered porous GDC ceramic will be referred to as the “porous scaffold” from now on. In the second stage, a polymeric precursor solution carrying fixed proportions of Ce^{4+} and Gd^{3+} ions is infiltrated into the pores of the scaffold and heated at 400°C to drive off the solvent and the organics. This yields interconnected films of GDC on the particle surfaces. In the third stage, the infiltrated scaffold is subjected to a final sintering procedure at 1000 to 1200°C to allow for solid-state diffusion to take place and to produce the final densified ceramic.

The GDC films formed on the GDC particles of the porous scaffolds by infiltration is considered to enhance the sintering rate for three reasons. First, they fill some of the porosity and cause an increase in the density even before the final heat treatment process (Figure 4.1). Second, they increase the coordination number of the scaffold particles that, i.e., form necks between particles were otherwise not in contact with each other (e.g., coordination of particles 2 and 3 in Figure 4.1 upon infiltration). Finally, the amorphous nature of the films at the surface of the GDC particles provide a fast diffusion pathway and thus allow for activated sintering. The major advantage of the

infiltration aided sintering process is the fact that the infiltrated solution contains the same cations as the host, i.e., no additives that may influence the electrical properties (as reported in Refs [9,15]) is required.

In the proposed lower temperature sintering process, it is obviously crucial that the infiltration of the GDC precursor is carried out effectively and homogeneously throughout the whole volume of the porous GDC scaffold. Only then, differential sintering and consequent cracking may be avoided. In order to be able to track the distribution of the infiltrated phase within the porous scaffold by chemical analyses, i.e., to test the effectiveness of the infiltration process, polymeric precursors that contain cations other than Gd^{3+} and Ce^{4+} must be infiltrated into porous GDC scaffolds. Therefore, the use of an Fe bearing polymeric precursor solution (which will be referred to as polymeric FeOx precursor from then on) as an infiltrating liquid to serve as a marker is also planned (Figure 4.1). The selection of Fe cation as an infiltration marker originates from the fact that oxides of Fe is a common GDC sintering aid and thus, the results obtained here can be compared to the reports in the literature [9, 20, 30, 31].

4.3. Experimental Methods

Experimental method is explained in this section.

4.3.1. Fabrication of Porous GDC Scaffold Electrolyte

10 mol % gadolinium-doped ceria powder (denoted as GDC, $Ce_{0.9}Gd_{0.1}O_3$, PRAXAIR >99.9%) was used for preparing the porous ceramic scaffolds. Specific surface area of this powder was $6.5 \text{ m}^2/\text{g}$ while the d_{10} , d_{50} and d_{95} values were $0.4 \mu\text{m}$, $0.5 \mu\text{m}$ and $0.9 \mu\text{m}$, respectively. The powder was pressed in a 15 mm diameter cylindrical stainless steel die by uniaxial pressing (Carver Hydraulic Press, Wabash, IN, USA) with 180 MPa pressure. The pellets were then fired to obtain a porous scaffold in an electrically heated laboratory kiln (Nabertherm LHT 02/17, Germany) at 1000°C with 6 hours of soaking time at a heating/cooling rate of $3^\circ\text{C}/\text{min}$.

4.3.2. Polymeric Precursor Solution Preparation and Infiltration Process

To densify porous GDC scaffolds polymeric GDC or Fe-oxide polymeric precursor infiltration was envisioned. To prepare the polymeric GDC precursor; $\text{Ce}(\text{NO}_3)_3 \cdot 6\text{H}_2\text{O}$ (ALFA-AESAR >99.5%) and $\text{Gd}(\text{NO}_3)_3 \cdot 6\text{H}_2\text{O}$ (Sigma-Aldrich >99.9%) salts were dissolved in deionized water at a cation molar ratio to obtain the $\text{Ce}_{0.9}\text{Gd}_{0.1}\text{O}_{1.95}$ (GDC) stoichiometry. In the next step, the salt solution was mixed with ethylene glycol in different molar ratios i.e. cation/ethylene glycol molar ratios = (0.020 to 0.080) and stirred at $\sim 80^\circ\text{C}$ until all water evaporated and polymerization took place. The determination of these ratios have been purely empirical. To avoid excessive infiltration/decomposition steps to achieve an acceptable amount of infiltrant loading, efforts were made to maximize the cation molarity which could be chelated to the polymeric chains, without increasing the viscosity to an extent that could inhibit the penetration of the final precursor into the porous scaffold. The solution was diluted with 2-butoxyethanol in order to ensure good wetting properties of GDC scaffold and for reducing the surface tension of the polymeric solutions.

Iron bearing polymeric precursor solution was prepared following a similar procedure but this time an aqueous solution of iron (III) nitrate nanohydrate (ALFA-AESAR >99.99%) salt was used. Further details of the process are given elsewhere [32-34].

Figure 4.1(a)-(b) shows schematically the infiltration process of porous GDC by GDC and iron bearing precursor solutions, respectively. Porous GDC pellet that was pre-sintered at 1000°C for 6 hours, was immersed in the infiltration solution in a beaker before being placed in a desiccator which was evacuated by a laboratory vacuum pump (Lanphan 2XZ-2, Zhengzhou, Henan, China). Thereby, most of the bubbles entrapped in open pores were forced to leave the specimen and be placed by the polymeric solution. Next, the surface of the pellets were wiped with a paper towel, placed onto a hot plate and gradually heated to 400°C until all solvent evaporated and organics burnt out. This procedure was repeated 25 or 35 times before the samples were subjected to a secondary heat treatment in an electrically heated kiln at different temperatures (e.g. 1000 - 1100 - 1200°C) for 8 hours.

4.3.3. Density Measurement

Bulk densities of the pellets were measured by Archimedes method according to ASTM C-20 standard [35]. After the density measurement of samples, relative density was estimated by using the equation (4.1):

$$\% \text{ Relative Density (\%RD)} = (d_s/d_{th}) \times 100 \quad (4.1)$$

where d_s is the measured bulk density of sample and d_{th} is the theoretical density of GDC. Theoretical density of 10 mol% gadolinium doped ceria is taken as 7.2 g/cm^3 [36,38];

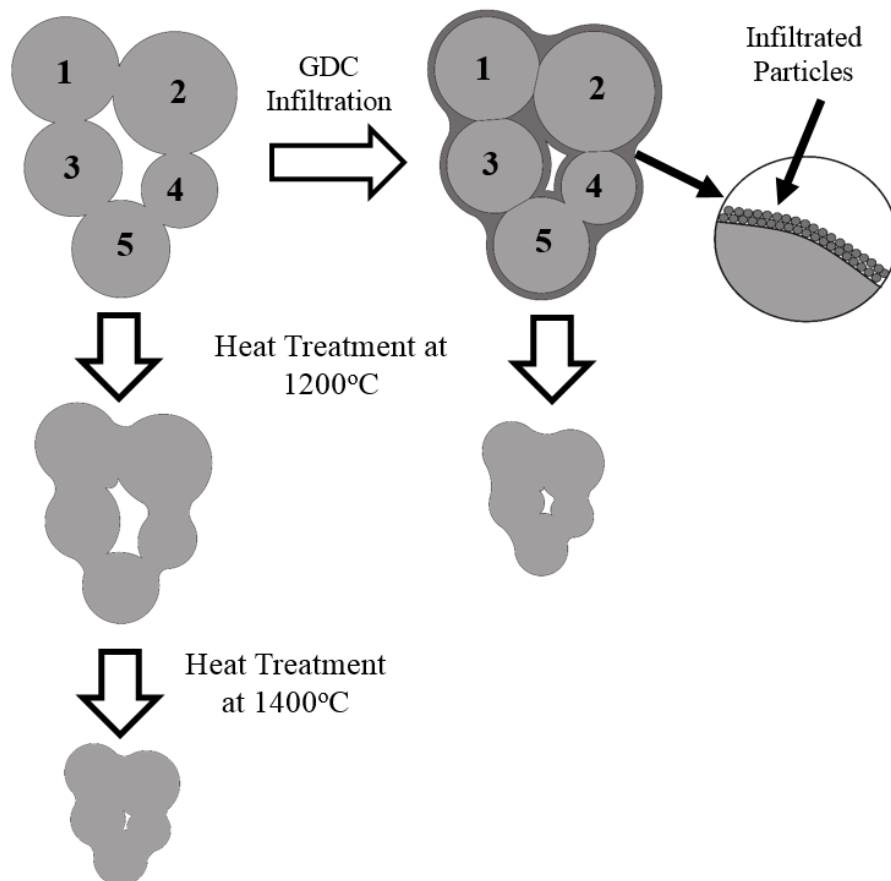


Figure 4.1. Schematic representation of the sintering behavior of the consolidated gadolinia doped ceria (GDC) ceramic particles with and without polymeric GDC precursor infiltration. Here, the infiltrated GDC phase serves to i) form connections between particles that are otherwise uncoordinated (e.g., between particles 2 and 3), ii) increase the overall solids loading of the green body and iii) provide fast diffusion routes through its amorphous volume.

4.3.4. Structural and Microstructural Characterization

The crystal structures of samples were studied by X-Ray Diffraction (XRD, Panalytical X-Pert Pro). Cu K α radiation was used as the x-ray source. Both the microstructural and compositional analysis of the non-infiltrated GDC and infiltrated GDC electrolyte samples were analyzed by Scanning Electron Microscopy (SEM, Philips XL 30S FEG) utilizing secondary electron (SE) imaging and Energy Dispersive X-Ray Spectroscopy (EDX).

4.3.5. Coding of Samples

A coding scheme was used to help the reader better follow the manuscript. For example, the sample code 35-G-80-1200 represents a porous pellet that was infiltrated 35 times by a solution bearing 0.080 molar GDC before being sintered again at 1200°C for 8 hours. This coding scheme was explained in Table 4.1.

Table 4.1. Table showing the processing parameters and the corresponding sample code numbers.

Code Number	Infiltration			Final Sintering
	Number of Cycles	Solution Type	Concentration (M)	Temperature (°C)
25-G-40-1000	25	GDC	0.040	1000
25-G-40-1200	25	GDC	0.040	1200
35-G-40-1200	35	GDC	0.040	1200
35-G-80-1200	35	GDC	0.080	1200
25-F-15-1000	25	Fe	0.015	1000
25-F-15-1200	25	Fe	0.015	1200
25-F-20-1200	25	Fe	0.020	1200
35-F-20-1200	35	Fe	0.020	1200

4.4. Results and Discussions

4.4.1. Crystal Structure Analyses

The crystal structure of the gadolinia doped ceria (GDC) ceramics sintered conventionally or by using an infiltration-assisted approach were analyzed by x-ray diffraction (XRD), as shown in Figures 4.2a-c. In the conventionally sintered GDC ceramics, all collected patterns appear to match well with the reference pattern for cubic GDC numbered JCPDF 01-075-0161 (Figure 4.2a).

Porous GDC scaffolds infiltrated with different amounts of GDC, sintered at either 1000°C or 1200°C consisted of the same GDC phase $\text{Ce}_{0.9}\text{Gd}_{0.1}\text{O}_{1.95}$ with JCPDF number 01-075-0161, i.e., no new compound formation after infiltration and sintering is observed, as expected (Figure 4.2b). When the porous GDC scaffolds are infiltrated by different amounts of polymeric FeO_x precursor and heat treated at 1000 or 1100 °C, the second highest peak of the Fe_2O_3 peak at $2\theta=35.6^\circ$ appears (PDF: 01-089-2810, Figure 4.2c). When the sintering temperature is raised to 1200 °C, peaks belonging to the compound $\text{Fe}_5\text{Gd}_3\text{O}_{12}$ (PDF:00-013-0327) is also observed (Figure 4.2c). Upon the introduction of a higher amount of FeO_x into the porous GDC scaffold by infiltration, a higher amount of $\text{Fe}_5\text{Gd}_3\text{O}_{12}$ phase is observed (Figure 4.2c).

4.4.2. Weight and Density Measurements

For a clear analysis of the impact of the application of the infiltration method on the densification rate of GDC ceramics, a set of reference data on the conventional solid-state sintering behavior of the GDC ceramics is collected. The relative densities of the sintered GDC pellets, calculated using Equation 4.1, are plotted as a function of sintering temperature in Figure 4.3. As expected, the relative bulk density increases as the sintering temperature is increased. Only a slight difference in relative densities is observed upon sintering at the 800-1100°C temperature range. However, significant increase in the density takes place when sintering is performed at temperatures between 1100 and 1400°C, indicating a typical solid-state sintering behavior. In this same range,

densification rate was higher as well. Highly dense (>95% RD) GDC ceramics that are directly applicable as SOFC electrolytes is obtained upon sintering at temperatures over 1400°C.

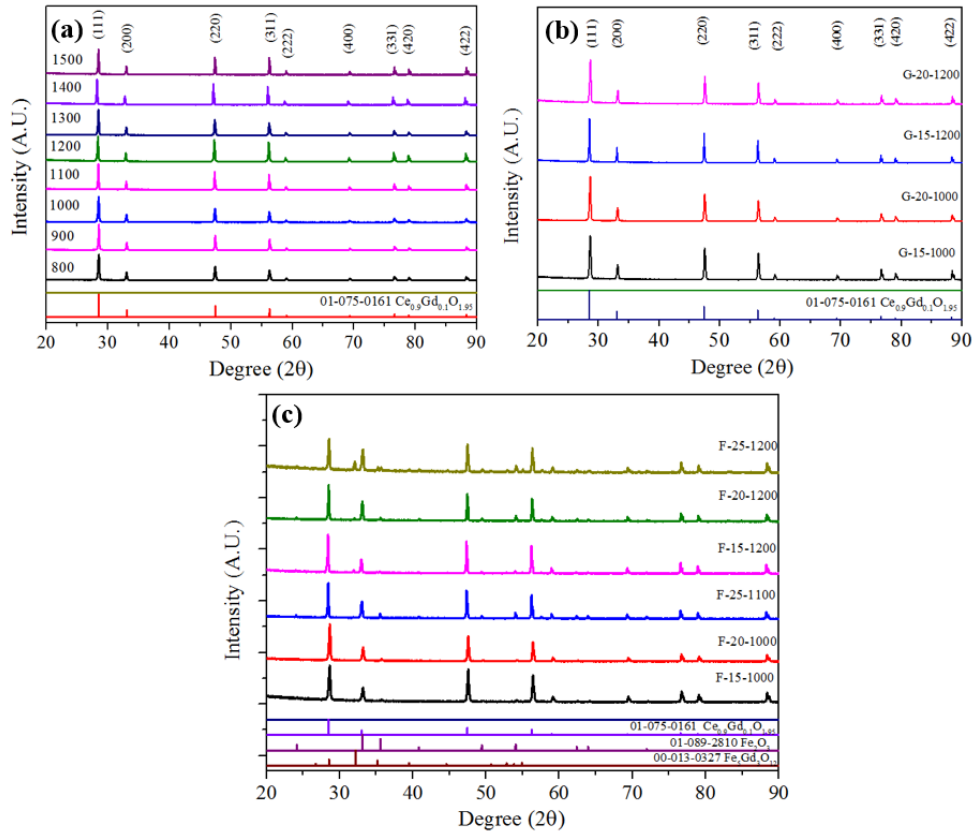


Figure 4.2. X-ray diffraction patterns of a) blank, b) 15 or 20 times gadolinia doped ceria (GDC) infiltrated and c) 15, 20 or 25 times FeOx infiltrated GDC pellets sintered at 800-1500 °C (a) or 1000-1200 °C (b and c).

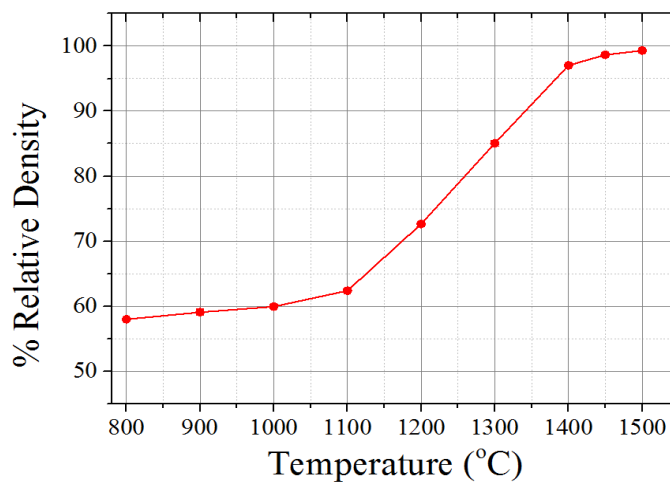


Figure 4.3. Effect of the sintering temperature on the relative density of the gadolinia doped ceria pellets. The sintering procedure was performed for 8 hours in stagnant air

Infiltration of polymeric GDC precursors into porous GDC pellets were performed to enhance the coordination among the GDC particles and increase the solids loading to maximize the green density and thus reduce the sintering temperature at which at least 95% relative density is achieved. The purpose was obviously to minimize the diffusion distances necessary for densification. The infiltration of polymeric GDC precursors were performed into porous GDC pellets with approximately 40% porosity (i.e., 60% density), obtained by pre-sintering at 1000°C for 6 hours.

GDC infiltration parameters, such as; the molarity of infiltration solutions, the number of infiltration cycles and the final sintering temperature were varied to observe their effect on the sintering behavior and finally achieve high relative final density at lower sintering temperatures (Figure 4.4). Each experimental run was replicated three times to weigh the error of the density measurement, which turned out to be very low (less than 0.8%). After each polymeric GDC infiltration and decomposition at 400 °C (i.e., one complete infiltration cycle) the weight of the porous scaffold was measured in order to determine the amount of GDC formed inside the porous scaffold and the rate at which the pores are being filled. Figure 4.4a depicts that all pellets consistently gained weight as the number of infiltration cycles increased (Figure 4.4a). As expected, when the polymeric GDC precursors with higher molarity of cations are used for infiltration, the weight increases with a more steep slope with increasing number of infiltration cycles (Figure 4.4a). It is also worth noting that the weight gain followed a somewhat linear trend in all cases, suggesting that neither clogging of the pores, nor reaching the maximum possible infiltration amount is taking place.

At the core of this study is an effort to maximize the density of GDC pellets by sintering at temperatures lower than the convention suggests. Therefore, the effects of the sintering temperature, number of infiltration cycles and the molarity of the infiltrating solution on final sintered density were studied. The relative densities of the porous GDC scaffolds infiltrated by polymeric GDC precursors with molarities ranging from 0.040 to 0.080 M for 25 or 35 cycles, subjected to a final sintering procedure at 1000 or 1200 °C are provided in Figure 4.4b. GDC infiltrated porous GDC scaffolds reached relative density values ranging from ca. 73% to 84%, depending on the number of GDC infiltration cycles and the polymeric precursor solution molarity upon being subjected to a final sintering procedure at 1000 °C for 8 hours. Increasing the amount of infiltration cycles and the polymeric precursor molarity, in other words, increasing the infiltrated GDC content appears to increase the obtained relative density upon final sintering at 1000

°C. Raising the final sintering temperature to 1200 °C results in a further increase in the final relative density in all samples, allowing the achievement of a relative density value in excess of 95% in the case of the sample infiltrated by a polymeric GDC precursor with a molarity of 0.080 M for 35 cycles (35-G-80). It should be noted that by conventional solid-state sintering at 1200 °C, a relative density value of only 75% was achieved and a 95% relative density was possible only when sintering temperatures exceeding 1400 °C were used (Figure 4.3). Therefore, significant savings in final sintering temperatures were successfully achieved.

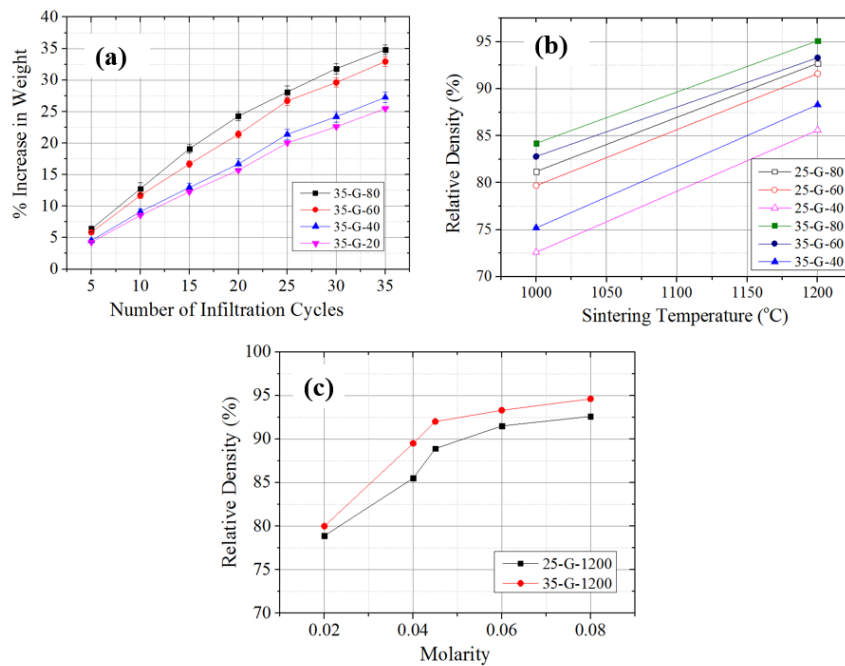


Figure 4.4. a) Effect of polymeric gadolinia doped ceria (GDC) precursor infiltration cycles on the % weight increase of the porous GDC scaffolds when 0.02 (35-G-20), 0.04 (35-G-40), 0.06 (35-G-60) and 0.08 M (35-G-80) solutions are used, b) effect of the secondary heat treatment temperature on the final relative density of the GDC infiltrated porous GDC scaffolds when the infiltration was carried out for 25 or 35 cycles using polymeric precursor solutions with 0.04, 0.06 or 0.08 M concentrations and c) impact of solution molarity on the final relative density of the 25 or 35 times GDC infiltrated porous GDC scaffolds when the final heat treatment was carried out at 1200 °C.

Figure 4.4c more clearly shows the effect of precursor solution molarity on the final density. In the case of samples subjected to a final sintering procedure at 1200 °C infiltrated by polymeric GDC precursors for 25 or 35 cycles, the final relative densities increase significantly when the solution molarity is increased from 0.020 to 0.080 M. In both cases of 25 or 35 cycles of infiltration, a plateau is almost reached at 0.080 M. Since, on the other hand, the weight gain still continues linearly at precursor molarities of 0.080

M even after 25 cycles of infiltration (Figure 4.4a), it can be suggested that although further GDC infiltration can still fill the pores of the scaffold, it can no longer connect the uncoordinated GDC particles of the porous GDC scaffold (Figure 4.4c).

The same parameters used in GDC infiltration were also investigated for FeOx infiltration. Figure 4.5a shows that increasing the number of infiltration cycles leads to a linear weight increase with no apparent saturation trend. Also, the use of polymeric FeOx precursor solution with a higher molarity results in a steeper weight gain, in a similar trend observed in GDC infiltration (Figure 4.5a).

FeOx infiltrated ceramics densified at even lower temperatures than the GDC infiltrated samples did (Figure 4.5b). For example, densities higher than 96% could be easily reached even after heat treating at 1100°C (Figure 4.5b). The reason for the faster densification observed in the FeOx infiltrated GDC ceramics than those infiltrated with GDC lies in the difference between the densification mechanisms GDC and FeOx infiltrations have to offer. The infiltrated FeOx phase forms films on the particles of the GDC scaffolds and functions as a sintering aid by viscous sintering [39-40]. Efforts to load more FeOx inside the pores by employing higher concentrations or number of cycles of solution resulted in almost no change in the relative density after sintering (Figures 4.5b and c). As reported in other studies, there is a maximum amount of iron addition that is beneficial and any further additions are useless to enhance the sintering rates and may even produce microcracks in specimens [36, 39-41].

4.4.3. Microstructural Analyses

Scanning electron microscopy (SEM) images of the fracture surfaces of the conventionally sintered GDC pellets, given in Figure 4.6, clearly shows that the amount of porosity decreases with increasing sintering temperature which is also consistent with the measured bulk densities (see Figure 4.3). As can be seen in Figure 4.6 (g-i) almost no open porosity remains upon sintering at temperatures above 1400 °C, agreeing well with the measured relative densities exceeding 97.0%. As a typical trait of solid-state sintering, densification in the present case is also accompanied by a significant grain growth (insets in Figure 4.6). The average grain size (determined by the lineal intercept method) increases from 164 to 765 nm when the sintering temperature is raised from 800 to 1500

°C, consistent with conventional solid-state sintering (Table 4.2). Note that much of the grain growth occurs between 1200 and 1400 °C.

The impact of the number of infiltration cycles, the concentration of the polymeric GDC precursor solution and the final heat treatment temperature on the microstructure of the GDC infiltrated porous GDC scaffolds is shown in the scanning electron microscopy (SEM) images (Figure 4.7). Overall, similar microstructures are observed in the SEM images taken from the upper, middle and bottom parts of the fractured pellets, suggesting that the infiltration solution penetrated equally well to all parts of the sample (Figure 4.7). As the heat treatment temperature of the porous GDC scaffold infiltrated by a 0.040 M polymeric GDC precursor solution for 25 cycles is increased from 1000 (Figures 4.7a-c) to 1200 °C (Figures 4.7d-f) a decrease in the porosity is observed. In this case, the faster diffusion rates enabled by a higher temperature is responsible for denser microstructure. Increasing the number of infiltration cycles contributes little to the resulting sintered density (Figures 4.7g-i). Concentration of infiltrating solution is, however, more effective in obtaining higher density after sintering at 1200°C (Figures 4.7j-l).

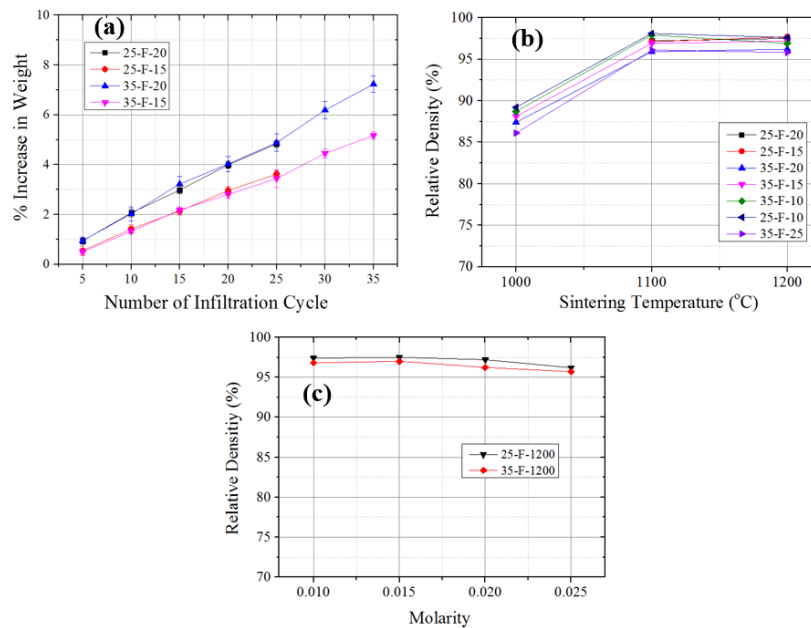


Figure 4.5. a) Effect of polymeric FeOx precursor infiltration cycles on the % weight increase of the porous GDC scaffolds when 0.015 or 0.020 M solutions are used, b) effect of the secondary heat treatment temperature on the final relative density of the FeOx infiltrated porous GDC scaffolds when the infiltration was carried out for 25 or 35 cycles using polymeric precursor solutions with 0.01, 0.015 or 0.020 M concentrations and c) impact of solution molarity on the final relative density of the 25 or 35 times FeOx infiltrated porous GDC scaffolds when the final heat treatment was carried out at 1200 °C.

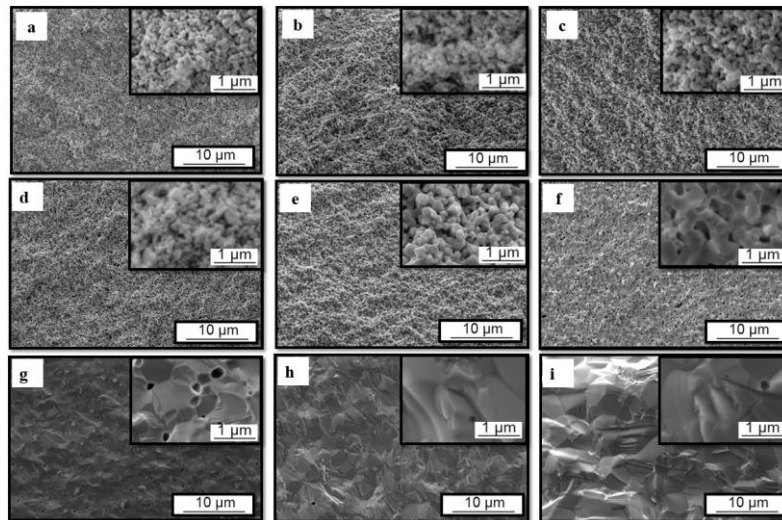


Figure 4.6. Scanning electron microscopy images of the fracture surfaces of the gadolinia doped ceria pellets a) 800 b) 900 c) 1000 d) 1100 e) 1200 f) 1300 g) 1400 h) 1450 and i) 1500 for 8 hours in air. The insets provide higher magnification images.

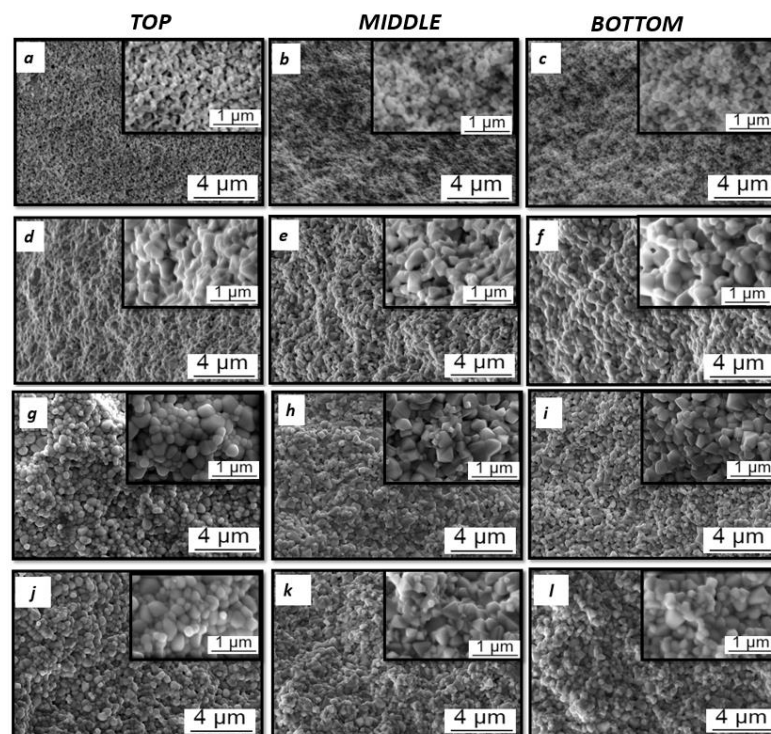


Figure 4.7. Scanning electron microscopy images of the fractured surfaces of porous gadolinia doped ceria (GDC) scaffolds infiltrated for 25 cycles using a 0.04 M polymeric GDC precursor and heat treated at a-c) 1000 °C (25-G-40-1000) and d-f) 1200 °C (25-G-40-1200) for 8 hours in air, of porous GDC scaffolds infiltrated for 35 cycles using a g-i) 0.04 M (35-G-40-1200) and j-l) 0.08 M (35-G-80-1200) polymeric GDC precursor solution both sintered at 1200 °C for 8 hours in air. The images in the same row were taken from the top, middle and bottom sections (from left to right) of the same sample to observe the uniformity of the microstructure. The insets show higher magnification images.

Table 4.2. Effect of sintering temperature on gadolinia doped ceria (GDC) grain size and relative density

Sintering Temperature (°C)	Grain Size (nm)	Relative Density (%)
800	164 (30)	58.2
900	163 (15)	59.0
1000	168 (14)	60.0
1100	196 (21)	63.0
1200	217 (25)	72.0
1300	348 (22)	85.5
1400	727 (50)	97.0
1450	741 (66)	98.7
1500	765 (47)	99.3

Higher magnification SEM images showing the resultant grain size are given as insets in Figure 4.7. The measured average grain size values in the top, middle and bottom parts of the GDC infiltrated GDC ceramics are quite similar (Table 4.3), indicating a homogeneous distribution of the infiltrated GDC phase. An increase in the relative density from 72.6% to 95.5% corresponds to an average grain size increase from 247 to only 432 nm (Table 4.3). Conventionally sintered GDC pellets sintered at 1400 °C have similar density with those GDC infiltrated GDC ceramics sintered at 1200 °C, but at roughly twice as much grain size, thus making the latter a still more attractive process. Some groups, reported that the grain boundaries act as barriers to oxygen ion transport and hence, increasing grain size tends to enhance the electrical conductivity of GDC [45-48]. On the other hand, some groups find contradicting results, suggesting an increase in the electrical conductivity of GDC with smaller grain size [49-52]. To clarify this issue, further investigations on the effect of microstructure on the electrical conductivity of GDC ceramics is required.

To be able to track the distribution of the infiltrated phase within the porous GDC scaffold, microstructural evolution of the polymeric FeOx precursor infiltrated GDC ceramics has been investigated via SEM (Figure 4.8). Similar to GDC infiltrated samples, SEM images were collected from top, middle and bottom parts of the fracture surfaces of the pellets. The microstructure appears denser when the sintering temperature of the FeOx infiltrated GDC ceramics were raised from 1000 (Figures 4.8a-c) to 1200 °C (Figures 4.8d-f). The achievement of dense GDC ceramics at low sintering temperatures (1000-1200 °C) in the presence of FeOx has also been reported in the literature [30, 31, 42-44].

No significant changes in the microstructure are observed when the molarity of the infiltration solution is raised from 0.015 (Figures 4.8d-f) to 0.020 M (Figures 4.8g-i) or when the number of infiltration cycles were increased from 25 (Figures 4.8g-i) to 35 (Figures 4.8j-l).

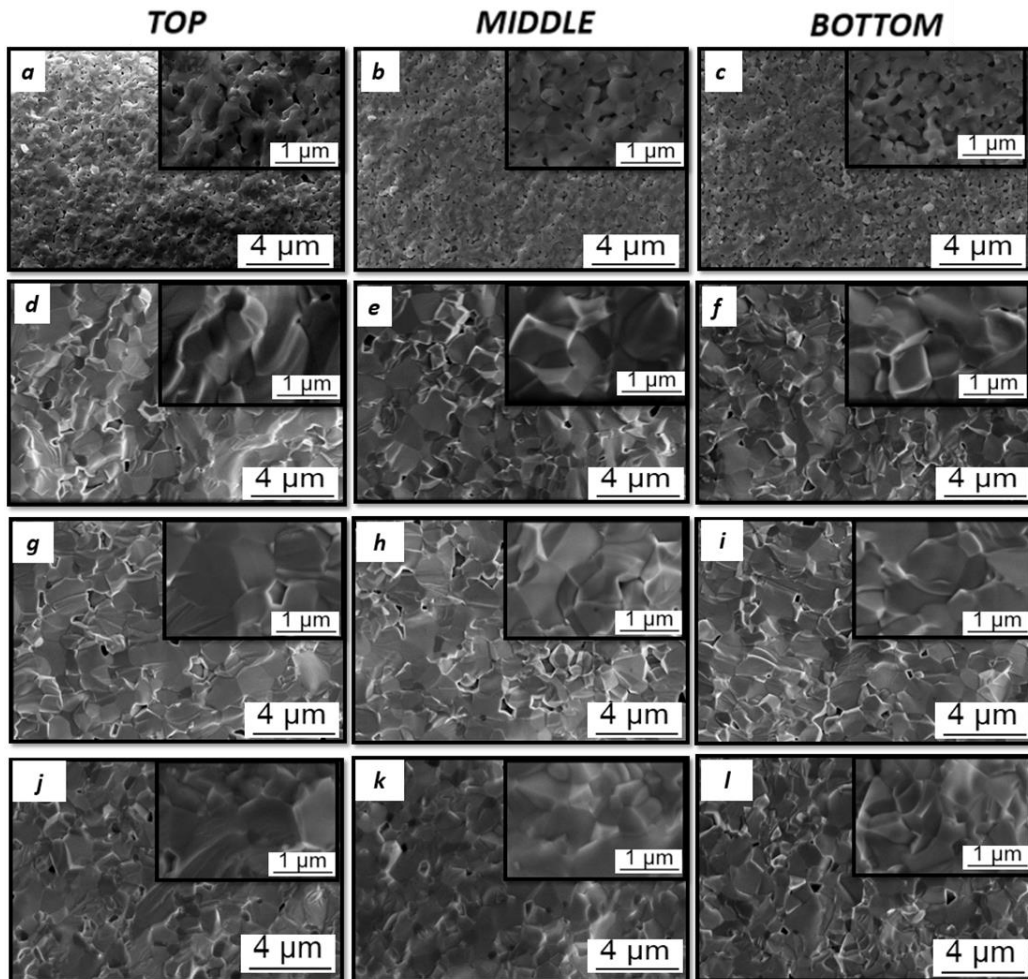


Figure 4.8. Scanning electron microscopy images of the fractured surfaces of porous gadolinia doped ceria (GDC) scaffolds infiltrated with a polymeric FeOx precursor solution with a molarity of 0.015 M for 25 cycles, sintered at a-c) 1000 °C (25-F-15-1000) and d-f) 1200 °C (25-F-15-1200), porous GDC scaffolds infiltrated with a polymeric FeOx precursor with a molarity of 0.020 M for g-i) for 25 (25-F-20-1200) and j-l) 35 cycles (35-F-20-1200), sintered at 1200 °C for 8 hours in air. The images in the same row were taken from the top, middle and bottom sections (from left to right) of the same sample to observe the uniformity of the microstructure. The insets show higher magnification images.

Grain sizes measured via lineal intercept method suggest a significant grain growth with increased density. The average grain size increases from 324 to 738 nm when the samples are densified from 89.9 to 97.7% relative density (Table 4.3). The difference in the grain growth regimes of the GDC and FeOx infiltrated samples accompanying

densification is notable. As mentioned earlier in the text, GDC infiltration into porous GDC scaffolds promote low temperature densification by i) filling some of the pores prior to heat treatment, ii) increasing the coordination numbers of the particles and iii) providing fast diffusion pathways through the amorphous infiltrated GDC film. On the other hand, the addition of FeOx to GDC acts as a sintering aid by promoting viscous-flow sintering [53-55].

Table 4.3. Grain size and relative densities of the gadolinia doped ceria (GDC) and the FeOx infiltrated porous GDC scaffolds.

Sample Code	Grain Size (nm)				Relative Density (%)
	Upper	Middle	Bottom	Ave.	
25-G-40-1000	243 (27)	249 (12)	252 (24)	247 (21)	72.6
25-G-40-1200	351 (58)	343 (21)	363 (48)	352 (43)	86.7
35-G-40-1200	376 (87)	382 (73)	367 (90)	375 (84)	87.5
35-G-80-1200	442 (56)	434 (37)	421 (21)	432 (39)	95.5
25-F-15-1000	321 (21)	318 (20)	333 (32)	324 (25)	89.9
25-F-15-1200	705 (63)	706 (101)	704 (53)	705 (72)	97.4
25-F-20-1200	729 (99)	751 (114)	735 (107)	738 (106)	97.7
35-F-20-1200	750 (71)	740 (69)	735 (62)	741 (68)	96.6

Infiltration aided-sintering at reduced temperatures may be a feasible processing technique only if the infiltrated phase is distributed homogeneously throughout the porous scaffold. Since GDC infiltration into porous GDC scaffolds would not allow the tracking of the infiltrated phase distribution by chemical analysis, polymeric FeOx precursors were used instead. The SEM-EDX line scan results shown in Figure 4.9 describes the dependence of the atomic ratios of Ce, Fe and Gd cations on the distance from the top surface of the specimen encoded as 25-F-20-1200. By infiltration, Fe cation almost in the same amount of Gd has been introduced to the porous GDC scaffold (Figure 4.9). It is evident that the Fe content remains unchanged throughout the ceramic, suggesting that GDC infiltration using the same type of precursor likely results in a similar infiltrated phase distribution.

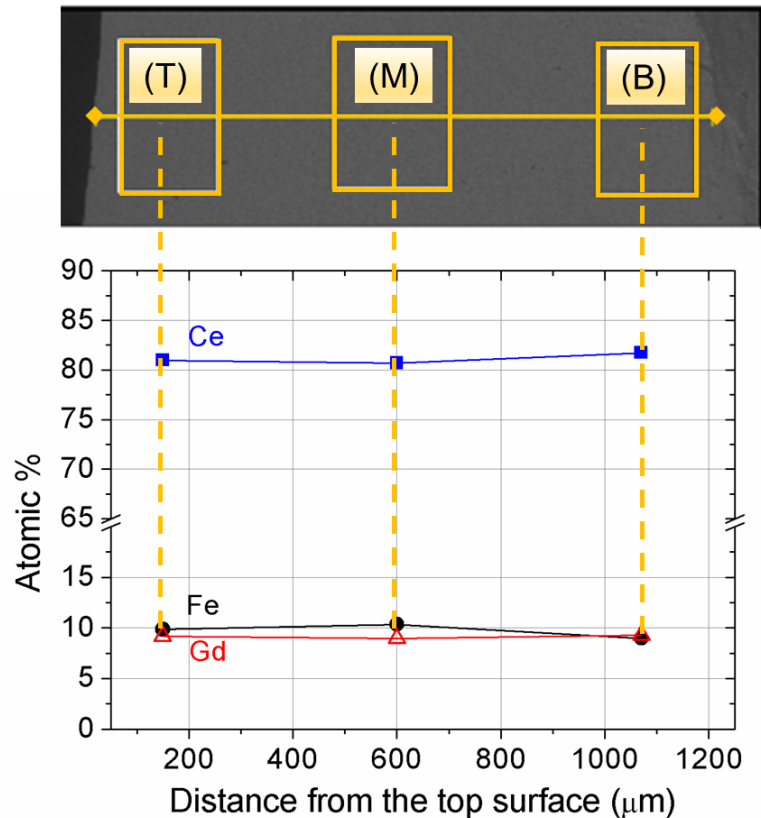


Figure 4.9. Change in the atomic ratios of Fe, Ce and Gd cations in the FeOx infiltrated gadolinia doped ceria (GDC) ceramic which yielded a highest relative density of 97% (sample code: 25-F-15-1100-8) with distance from the top surface, obtained from energy dispersive x-ray spectroscopy (EDX) analyses. The regions where EDX measurements were collected are labelled as the «T», «M» and «B» on the scanning electron microscopy image of the cross-section of the sample and denote top, middle and bottom sections respectively.

4.5. Summary

Gadolinia doped ceria (GDC) electrolytes need to be fully dense (>95% relative density) in order to ensure a gas tight solid oxide fuel cell (SOFC) and thus, high open circuit voltage. GDC is traditionally sintered above 1400 °C, setting the anode sintering temperature at the same value for anode-supported cells. This results in coarse anode microstructures and thus poor SOFC performance. However, in this study, we offered and successfully demonstrated a method by which densification can be achieved at significantly lower sintering temperatures down to 1200°C with no additives that might influence the electrical properties. First a porous scaffold of GDC was produced by sintering at 1000°C before infiltration was performed in order to fill these pores by a

polymeric precursor that contains Ce and Gd cations. This way, formation of an amorphous film on the particles of GDC and thus, i) partial filling of the pores prior to sintering, ii) increasing the coordination number of the scaffold particles and formation of fast diffusion routes were aimed. As far as infiltration by Ce and Gd is concerned, the use of enriched infiltrating solution and increased number of cycles both enhanced densification, yielding a relative density of 95.5% after sintering at 1200°C. Due to the lowered sintering temperatures, the dense microstructure consisted of grains with an average diameter of 432 nm – a much smaller value than observed in the conventionally sintered GDC ceramics with a similar density (727 nm).

FeOx infiltration into porous GDC scaffolds were also performed to be able to track the distribution of the infiltrated phase within the ceramic. FeOx, as reported in the literature [9,36,39-41,44], acted as a sintering aid which allowed densification at temperatures as low as 1100°C (relative density>97.7%). The scanning electron microscopy-energy dispersive x-ray spectroscopy line scan analyses showed that the Fe distribution within the GDC ceramic was very uniform, suggesting a similar situation in the case of GDC infiltration.

Acknowledgements

This project is supported by TUBITAK (The Scientific Research Council of Turkey) through project no. 116R072. Authors would like to thank different labs in both Izmir Institute of Technology and Gebze Technical University for their helps during analysis of samples.

4.6. References

- [1] Morales, M.; Roa, J.; Tartaj, J.; Segarra, M. *Journal of the European Ceramic Society* **2016**, *36*(1), 1–16.
- [2] Sındıraç, C.; Akkurt, S. *International Journal of Hydrogen Energy* **2016**, *41*(40), 18157–18165.
- [3] Wang, X.; Chen, Z.; Atkinson, A. *Journal of the European Ceramic Society* **2013**, *33*(13-14), 2539–2547.

- [4] Singhal, S. C.; Kendall, K. *High Temperature and Solid Oxide Fuel Cells* **2003**,
- [5] Minh, N. Q. *Journal of the American Ceramic Society* **1993**, 76(3), 563–588.
- [6] Tarancón, A. *Energies* **2009**, 2(4), 1130–1150.
- [7] Basu, R. N.; Blass, G.; Buchkremer, H. P.; Stöver, D.; Tietz, F.; Wessel, E.; Vinke, I. C. *Journal of the European Ceramic Society* **2005**, 25(4), 463–471.
- [8] Badwal, S. *Solid State Ionics* **1992**, 52(1-3), 23–32.
- [9] Zhang, T.S.; Ma, J.; Leng, Y. J.; Chen, S.H.; Hing, P.; Kilner, J. A. *Solid State Ionics* **2004**, 168, 187-195.
- [10] Fagg, D. P.; Kharton, V. V.; Frade, J. R. *Journal of Electroceramics* **2002**, 9, 199-207.
- [11] Steele B.C.H. *Journal of Materials Science* **2001**, 36(5), 1053–1068.
- [12] Blumenthal, R. N.; Brugner, F. S.; Garnier, J. E. *Journal of The Electrochemical Society* **1973**, 120(9), 1230.
- [13] Selçuk, A.; Atkinson, A. *Journal of the European Ceramic Society* **1997**, 17(12), 1523–1532.
- [14] Gerhardt-Anderson, R.; Nowick, A. *Solid State Ionics* **1981**, 5, 547–550.
- [15] Kilner, J. *Solid State Ionics* **1983**, 8(3), 201–207.
- [16] Taub, S.; Williams, R. E.; Wang, X.; McComb, D. W.; Kilner, J. A.; Atkinson, A. *Acta Materialia* **2014**, 81, 128–140.
- [17] Inaba, H.; Nakajima, T.; Tagawa, H. *Solid State Ionics* **1998**, 106(3-4), 263-268.
- [18] Torrens, R.; Sammes, N.; Tompsett, G. *Solid State Ionics* **1998**, 111(1-2), 9–15.
- [19] Reddy, K. R.; Karan, K. *Journal of Electroceramics* **2005**, 15(1), 45–56.
- [20] Kleinlogel, C.; Gauckler, L. J. *Solid State Ionics* **2000**, 135, 567.
- [21] Mori, M.; Suda, E.; Pacaud, B.; Murai, K.; Moriga, T. *Journal of Power Sources* **2006**, 157(2), 688–694.
- [22] Zhou, Y.; Rahaman, M. N. *Acta Materialia* **1997**, 45(9), 3635–3639.
- [23] Prasad, D. H.; Lee, J. H.; Lee, H. W.; Kim, B. K.; Park, J. S. *Journal of Ceramic Processing Research* **2010**, 11(5), 523-526.
- [24] Sato, K. *Japanese Journal of Applied Physics* **2012**, 51(7R), 077301.

- [25] Buyukaksoy, A.; Petrovsky, V.; Dogan, F. *Journal of the Electrochemical Society* **2012**, *159*(12), B67-B71.
- [26] Vohs, J. M.; Gorte, R. J. *Advanced Materials* **2009**, *21*(9), 943–956.
- [27] Park, S.; Gorte, R. J.; Vohs, J. M. *Journal of The Electrochemical Society* **2001**, *148*(5).
- [28] Sholklapper, T. Z.; Lu, C.; Jacobson, C. P.; Visco, S. J.; Jonghe, L. C. D. *Electrochemical and Solid-State Letters* **2006**, *9*(8).
- [29] Jiang, S. P. *International Journal of Hydrogen Energy* **2012**, *37*, 449-470.
- [30] Nicholas, J.; Dejonghe, L. *Solid State Ionics* **2007**, *178*(19-20), 1187–1194.
- [31] Zhang, T.; Ma, J.; Leng, Y.; He, Z. *Journal of Crystal Growth* **2005**, *274*(3-4), 603–611.
- [32] Buyukaksoy, A.; Birss, V. I. *Journal of Power Sources* **2016**, *307*, 449–453.
- [33] Anderson, H U.; Chen, C. C.; Nasrallah, M. M. *U.S. Patent 5* **1996**, *494*, 700
- [34] Buyukaksoy, A.; Kammampata, S. P.; Birss, V. I. *Journal of Power Sources* **2015**, *287*, 349–358.
- [35] ASTM C20-00(2015), Standard Test Methods for Apparent Porosity, Water Absorption, Apparent Specific Gravity, and Bulk Density of Burned Refractory Brick and Shapes by Boiling Water, *ASTM International*, West Conshohocken, PA, **2015**, www.astm.org.
- [36] Zhang, T.; Ma, J.; Huang, H.; Hing, P.; Xia, Z.; Chan, S.; Kilner, J. *Solid State Sciences* **2003**, *5*(11-12), 1505–1511.
- [37] Chourashiya, M.; Patil, J.; Pawar, S.; Jadhav, L. *Materials Chemistry and Physics* **2008**, *109*(1), 39–44.
- [38] Badwal, S. P. S.; Fini, D.; Ciacchi, F. T.; Munnings, C.; Kimpton, J. A.; Drennan, J. *Journal of Materials Chemistry A* **2013**, *1*(36), 10768.
- [39] Zhang, T. S.; Ma, J.; Kong, L. B.; Chan, S. H.; Hing, P.; Kilner, J. A. *Solid State Ionics* **2004**, *167*, 203-207.
- [40] Tianshu, Z.; Hing, P.; Huang, H.; Kilner, J. *Journal of Materials Science* **2002**, *37*(5), 997–1003.
- [41] Zhang, T.; Kong, L.; Zeng, Z.; Huang, H.; Hing, P.; Xia, Z.; Kilner, J. *Journal of Solid State Electrochemistry* **2003**, *7*(6), 348–354.
- [42] Dong, Q.; Du, Z.; Zhang, T.; Lu, J.; Song, X.; Ma, J. *International Journal of Hydrogen Energy* **2009**, *34*(19), 7903–7909.

- [43] Limthonghul, P.; Jivaganent, P.; Loyma, W.; Pannaram N.; Charojrochkul, S. *ECS Transactions* **2009**, *25*(2), 1555-1563.
- [44] Zhang, T. S.; Ma, J; Chan S. H.; Kilner, J. A. *Solid State Ionics* **2005**, *176*, 377-384.
- [45] Hara, A.; Hirata, Y.; Sameshima, S.; Matsunaga, N.; Horita, T. *Journal of the Ceramic Society of Japan* **2008**, *116*(1350), 291–297.
- [46] Christie G. M.; van Berkel, F. P F. *Solid State Ionics* **1996**, *83*, 17-27.
- [47] Tschöpe, A.; Sommer, E.; Birringer, R. *Solid State Ionics* **2001**, *139*, 255-265.
- [48] Tschöpe, A.; Birringer, R. *Journal of Electroceramics* **2001**, *7*(3), 169–177.
- [49] Pandiyan, A.; Moorthy, S. B. K. *Nanomaterials and Energy* **2012**, *1*, 288-305.
- [50] Singh, V.; Babu, S.; Karakoti, A. S.; Agarwal, A.; Seal, S. *Journal of Nanoscience and Nanotechnology* **2010**, *10*(10), 6495–6503.
- [51] Baldinozzi, G.; Simeone, D.; Gosset, D.; Dollé, M.; Petot-Ervas, G. *Materials Research Society Symposium Proceedings* **2008**.
- [52] Zhou, X.-D.; Huebner, W.; Kosacki, I.; Anderson, H. U. *Journal of the American Ceramic Society* **2004**, *85*(7), 1757–1762.
- [53] Bonnet, J.; Dolet, N.; Heintz, J. *Journal of the European Ceramic Society* **1996**, *16*(11), 1163–1169.
- [54] Varela, J. A. *Journal American Ceramic Society* **1996**, *79*, 789.
- [55] Lewis, G. S.; Atkinson, A. Steele, B. C. H.; Drennan J. *Solid State Ionics* **2002**, *152-153*,567.

CHAPTER 5

ELECTRICAL PROPERTIES OF GADOLINIA DOPED CERIA ELECTROLYTES FABRICATED BY INFILTRATION-AIDED SINTERING

Can Sındıraç¹, Aligül Büyükaksoy^{2,3*} Sedat Akkurt¹,

¹ Izmir Institute of Technology, Department of Mechanical Engineering, Urla, İzmir, 35433 Turkey

² Gebze Technical University, Department of Materials Science and Engineering, Gebze, Kocaeli 41400, Turkey

³ Gebze Technical University, Institute of Nanotechnology, Gebze, Kocaeli 41400, Turkey

*Corresponding Author:

E-mail: sedatakkurt@iyte.edu.tr (S.Akkurt) Ph: +90 (262) 750 6705

- *This chapter is published in Solid State Ionics*
- (DOI: 10.1016/j.ssi.2019.115020)

5.1. Abstract

Common solid oxide fuel cell (SOFC) electrolyte materials (e.g., gadolinia doped ceria – GDC) demand temperatures exceeding 1400°C for densification by conventional solid state sintering. It is very desirable to reduce the densification of the SOFC electrolytes to i) avoid microstructural coarsening of the composite anode layers, which are co-sintered with the electrolyte layer in the anode supported SOFC fabrication scheme and ii) reduce energy consumption during SOFC manufacturing. We have recently demonstrated a novel infiltration-aided sintering route to densify GDC ceramics at 1200 °C. In the present work, for the first time in the literature, we present the electrical properties of GDC ceramics fabricated thusly. Comparison of high density ($\geq 95\%$) samples fabricated by conventional or infiltration-aided sintering reveal that at 700 °C, similar total electrical conductivities are obtained, while at 300 °C, specific grain boundary resistivity is smaller in the latter. Bulk (grain) conductivity is higher in porous GDC ceramics (relative density $\leq 90\%$) fabricated by infiltration-aided sintering than the

conventionally sintered ones with similar porosities. Finally, open circuit voltage of 0.84 V at 700 °C, obtained under dilute hydrogen and stagnant air conditions suggests that GDC ceramics densified by infiltration-aided sintering are suitable for use as SOFC electrolytes.

Keywords: solid oxide fuel cell, electrolyte, microstructure, densification, infiltration, conductivity, open circuit voltage

5.2. Introduction

Oxygen ion conducting ceramic electrolytes form the basis of solid oxide fuel cells (SOFCs), which are a very promising energy conversion technology, as an alternative to the conventional, combustion-based ones. Ceramic electrolytes used in SOFCs must be dense in order to deny the mixing of oxygen and fuel gases purged from the cathode and anode sides respectively and thusly avoid violent burnout and short-circuit [1-5]. An electrolyte layer with a relative density (R.D.) of ca. 95% is generally necessary to achieve a gas-tight cell [2,6].

The extensively used SOFC electrolytes such as yttria stabilized zirconia (YSZ) [5,7] and gadolinia doped ceria (GDC) [1,2,6,8] require heat treatments at relatively high temperatures ($T \geq 1400^\circ\text{C}$) to achieve high density via conventional solid-state sintering. The high sintering temperature of the electrolyte brings about major issues during the processing of SOFCs. For example, since the conventional anode supported SOFC fabrication method involves the co-sintering of the tape-cast anode and electrolyte layers, high sintering temperatures yield coarse anode microstructures with short triple phase boundary (TPB) lengths and thus, low electrochemical activity [9,10,11]. In addition, high sintering temperatures add to the manufacturing cost of SOFCs, which render these devices economically less attractive [11]. Hence, it is very desirable to reduce the sintering temperatures of SOFC electrolytes down to $\leq 1200^\circ\text{C}$.

Among the possible ways to reduce the sintering temperature, the use of nano-scaled powders with extremely high surface areas is known to work well [8,12]. For example Kleinlogel et al. obtained a relative density of 98% upon sintering the 20 nm

sized-GDC powders at 1200 °C [13]. Yet, manufacturing such powders is expensive and hard to implement [12,14].

Another route to reduce the sintering temperature of SOFC electrolyte materials has been spark plasma sintering (SPS) or alternatively known as field assisted sintering technique (FAST), which is based on the application of a high DC current along with uniaxial pressure, generating sparks between the particles and thus very high local temperatures [15]. However, this process is limited by the high costs of equipment required to maintain the high DC current and pressure [16].

To reduce the sintering temperature of SOFC electrolyte materials, addition of transition metal oxides (TMOs), as sintering aids has been reported in the literature. For example, to reduce the sintering temperature of GDC, addition of CoO [17,18], CuO [18], Fe₂O₃ [19], MnO₂ [3] to initiate liquid phase sintering have been reported in the literature. Despite the achievement of RD values higher than 95% around 1100 °C [18], enhancement of the electronic conductivity of GDC which would reduce the open circuit potential of the SOFC is highly probable in the case of TMO sintering aids, due to the variable oxidation states of these additives [18,20]. Consequently, when lowering the sintering temperature of the SOFC electrolyte materials, utilization of a simple, low-cost and additive-free method is highly preferred.

As an alternative, we have recently proposed the infiltration-aided sintering method to densify the GDC electrolytes at reduced temperatures [21]. This process involves the utilization of the polymeric precursor infiltration approach, previously used to form electrocatalyst– ionic conductor composites which exhibited quite impressive electrochemical activity [22,23]. The infiltration-aided sintering, on the other hand, is performed by the infiltration of a polymeric GDC solution into a porous GDC scaffold that has been formed by partially sintering a die-pressed pellet at 1000 °C. By the infiltration process, an amorphous GDC coating on the GDC grains of the porous scaffold is formed and thus, i) partial filling of the pores prior to sintering, ii) enhancement of the coordination of the GDC particles within the porous scaffold and iii) generation of a fast diffusion pathway is ensured (Figure 5.1, [21]). Upon the application of a final heat treatment at temperatures as low as 1200 °C, GDC electrolytes with ca. 95% relative densities are achieved [21]. As expected, the tremendous amount of surface area provided by the nano-sized GDC infill helped boost the sintering rate early during heating. As a result of the low sintering temperatures, the dense GDC ceramics fabricated by infiltration-aided sintering had much smaller average grain size than those fabricated by

conventional sintering [21]. A similar approach to the infiltration-aided sintering has also been used by Jasinski et al [24], but to densify thin coatings of YSZ powders, which prevented detailed demonstration of densification and usability as an SOFC electrolyte.

In this study, the electrical properties of the GDC electrolytes fabricated by infiltration-aided sintering are investigated for the first time in the literature. More specifically, differences in the electrical conductivity, grain/grain boundary contributions to the total electrical conductivity of the GDC electrolytes fabricated by i) conventional solid-state sintering and ii) infiltration-aided sintering are determined by electrochemical impedance spectroscopy (EIS) measurements. To test the gas-tightness and thus the usability of the GDC ceramics fabricated by infiltration-aided sintering as SOFC electrolytes, open circuit voltage (OCV) measurements are also performed.

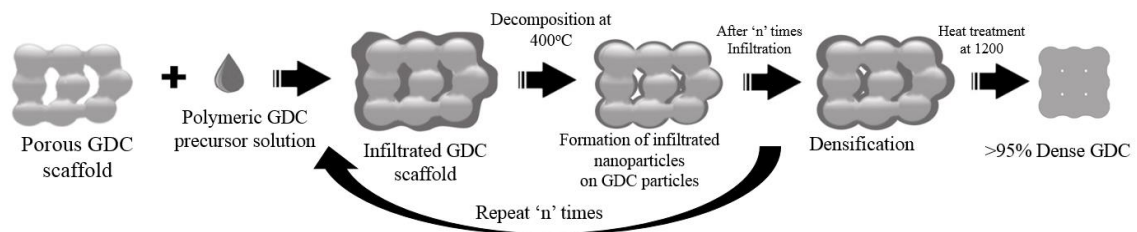


Figure 5.1. Schematic representation of the infiltration-aided sintering process

5.3. Experimental Methods

Dense 10 mol % gadolinium-doped ceria GDC electrolytes were prepared by two different techniques in the present work, namely; conventional sintering and infiltration-aided sintering. The former method was based on the high-temperature firing of the consolidated (die-pressed in this case) powders, while in the latter, the die pressed powder was only partially sintered at reduced temperatures to form a porous scaffold, followed its infiltration by polymeric GDC precursor. Then, finally, a second reduced temperature sintering process is realized. In both types of electrolytes, GDC ($\text{Ce}_{0.9}\text{Gd}_{0.1}\text{O}_3$, PRAXAIR >99.9%) powders with a specific surface area of $6.5 \text{ m}^2/\text{g}$ and a particle size distribution defined by the d_{10} , d_{50} and d_{95} values of $0.4 \text{ }\mu\text{m}$, $0.5 \text{ }\mu\text{m}$ and $0.9 \text{ }\mu\text{m}$, respectively, was used to prepare the ceramic disks. The as-received powder was uniaxially pressed (Carver Hydraulic Press, Wabash, IN, USA) under 180 MPa pressure in a 15 mm diameter cylindrical stainless steel die. Afterwards, for conventional sintering, the pellets were

fired in an electrically heated laboratory kiln (Nabertherm LHT 02/17, Germany) at temperatures between 1200 and 1400°C with 8 hours of soaking time. For the preparation of porous GDC scaffolds to be infiltrated with polymeric GDC precursors, the die-pressed samples were fired at 1000°C for 6 hours. In both cases, heating/cooling rate was fixed to 3 °C/min.

For the fabrication of dense GDC ceramics via infiltration-aided sintering, the obtained porous scaffolds were loaded with GDC infiltration solution. A polymeric GDC precursor solution was used to ensure that an interconnected film, rather than disconnected precipitates on the grains of the GDC scaffold is formed.

To prepare the polymeric GDC precursor solution, $\text{Ce}(\text{NO}_3)_3 \cdot 6\text{H}_2\text{O}$ (ALFA-AESAR >99.5%) and $\text{Gd}(\text{NO}_3)_3 \cdot 6\text{H}_2\text{O}$ (Sigma-Aldrich >99.9%) salts were mixed in the $\text{Ce}_{0.9}\text{Gd}_{0.1}\text{O}_{2-\delta}$ (GDC) stoichiometry, then, dissolved in deionized water and ethylene glycol at different cation molar ratios (i.e., 0.040 to 0.080). This was followed by sintering at ~80°C until all water had evaporated. The solution is diluted with 2-butoxyethanol to ensure good wetting properties and to reduce the surface tension of polymeric solutions. This is similar to the procedure followed in our earlier work [21].

Figure 5.1 shows schematically the infiltration process of precursor salts in porous GDC scaffold. Partially sintered porous GDC scaffold (with approximately 40% porosity) is immersed in the precursor solution in a beaker placed in a desiccator under vacuum (Lanphan 2XZ-2, Zhengzhou, Henan, China) to induce the removal of air bubbles trapped in pores and the penetration of the polymeric precursors. Afterwards, the surfaces of the pellets were wiped with a paper towel dry and heated gradually to 400°C until all solvents and organics decomposed. This infiltration process was repeated 25 or 35 times followed by a secondary sintering process at 1000 or 1200°C for 8 hours.

In this work, for convenience, a code number is assigned to every sample. These codes and the corresponding processing steps along with RD values are summarized Table 5.1. For example, the sample coded as “4” indicates that porous GDC scaffold partially sintered at 1000°C and infiltrated 25 times by a 0.040 molar GDC solution. Thereafter, infiltrated pellet undergoes a final sintering at 1000°C for 8 hours.

Bulk densities of the fabricated GDC ceramics pellets were measured by the Archimedes method according to ASTM C20 standard [25]. Relative densities were calculated by dividing the measured bulk densities by 7.2 g/cm^3 which is the theoretical density of 10 mol% Gd_2O_3 doped CeO_2 [26,27].

The microstructural analyses of the directly-sintered and infiltration-aided sintered GDC electrolytes were performed by Scanning Electron Microscopy (SEM, Philips XL 30S FEG) utilizing secondary electron (SE) imaging. Average grain sizes of samples were determined from the SEM images of fractured surfaces of the pellets via linear intercept method as described by Mendelson [28]. More specifically, the average grain size (D) was calculated by multiplying L by 1.56 where L is the average length of several random lines drawn in measuring the grain-boundary intercept length.

For the electrochemical impedance spectroscopy (EIS) analysis, silver paste was brush-painted onto both sides of the electrolyte so it can behave as an electrode and current collector layer. The Ag coated pellets were connected with Ag wires in alumina specimen holder inside the horizontal tubular furnace (Protherm, PTF 16/50/450, Ankara, Turkey). These cells were attached to Autolab (Metrohm) instrument to perform EIS analyses of the electrolyte in the range 250-700°C in stagnant air with an excitation voltage amplitude of 15 mV in the frequency range 10^{-2} - 10^5 Hz. Nova 2.1 software was used to fit the impedance data in Nyquist plot.

The open circuit voltage (OCV) measurements were performed at 450-700 °C using a Gamry Reference 3000 potentiostat/galvanostat/EIS analyzer. For these experiments, this time, NiO and Ag pastes were used for current collection from the fuel (a humidified mixture of 10% hydrogen – 90% argon) and air sides, respectively. The effective electrode areas were 0.5 cm². To ensure gas-tightness, pellets were fixed on alumina tubes by Ceramabond ceramic adhesive and glass sealant.

5.4. Results and Discussions

Scanning electron microscopy (SEM) images of the fracture surfaces of the gadolinia doped ceria (GDC) ceramics fabricated by conventional and infiltration-aided sintering are shown in Figure 5.2. Notice here that the code numbers for all seven images refer to those in Table 5.1. Figures 5.2 (1-3) depict the SEM images of GDC samples fabricated by conventional sintering at 1200, 1300 and 1400 °C for 8 h, respectively. Evidently, increasing the temperature brings about an enhancement in the relative density (RD- Figure 5.2, samples 1-3), consistent with the Archimedes measurements, which indicate an increase from 72.6% to 97% (Table 5.1). In the case of GDC ceramics

fabricated by infiltration-aided sintering, this time, achievement of high density (RD: 95%) is possible upon heat treatment at 1200 °C (Figure 5.2, sample 7). The obtained RD value increases as the number of infiltration cycles, the molarity of the infiltration solution and the secondary heat treatment temperature increases (Figure 5.2, samples 4-7 and Table 5.1).

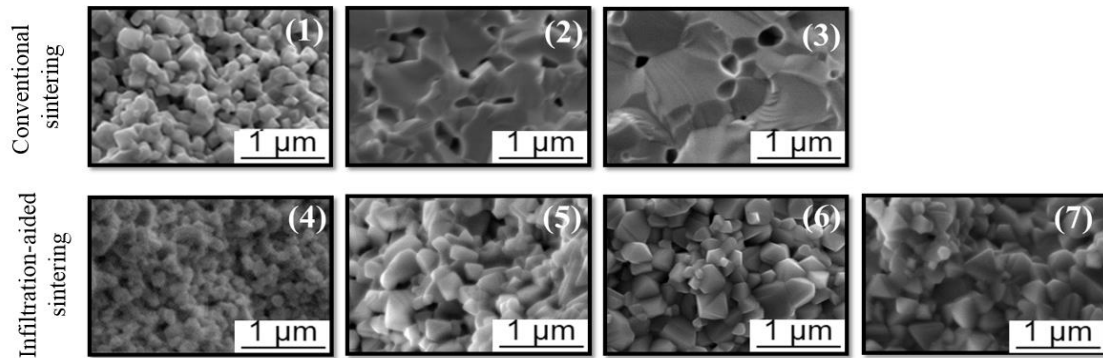


Figure 5.2. The Scanning electron microscopy images of the fracture surfaces of all seven samples obtained in the secondary electron mode.

Table 5.1. The sample code numbers and related infiltration process parameters. Relative density and grain size values of final ceramics are also listed with the standard deviations in paranthesis. Note that 1-3 are not infiltrated.

Code Number	Infiltration			Final Sintering	Relative Density (%)
	Number of Cycles	Concentration (M)	Weight Percent Infiltrated (%)	Temp. (°C)	
1	-	-	-	1200	71.8 (1.27)
2	-	-	-	1300	84.2 (0.95)
3	-	-	-	1400	97.5 (0.39)
4	25	0.040	19	1000	76.6 (2.10)
5	25	0.040	20	1200	85.6 (1.95)
6	35	0.040	27	1200	88.0 (1.80)
7	35	0.080	35	1200	95.0 (0.65)

Although no abnormal grain growth is observed in any of the samples, the grain growth behavior differs significantly depending on the densification route (Figure 5.3). The increase in RD from 71.8 to 97.5% is accompanied by an increase in the average grain size from 220 to 727 nm (Figure 5.3). In the case of GDC ceramics fabricated by infiltration-aided sintering, on the other hand, the grain growth concomitant to densification is much less pronounced. Upon densification from 76.6% to 95.0% the grain size increases from 247 to only 450 nm (Figure 5.3).

To determine the total electrolyte conductivity and to separate the contributions from bulk (grain) and grain boundaries to the oxygen ion transport resistance, electrochemical impedance spectroscopy is preferred in this work. The impedance spectroscopy measurement were performed on samples 1-7 at 250-700 °C, in air. For the sake of brevity, only measurements at 300 °C are shown in the Nyquist plots, in Figure 5.4 which electrolyte and electrode polarization arcs, all normalized to the electrode (current collector) area. Symbols and solid lines represent the measured data and the fitting curves, respectively. The equivalent circuit model used to perform the impedance fitting consists of one series area specific resistance (ASR1), corresponding to the non-zero high frequency intercept at the horizontal axis and two more area specific resistances (ASR2 and ASR3), each connected in parallel to a constant phase element (Q2 and Q3), defining the two semi-circles observed in Figure 5.4. Fit lines represent the collected EIS data, which is also reflected by the χ^2 values in the range of 10^{-4} obtained in each fitting.

The ASR and capacitance values obtained from the EIS fittings are given in Table 5.2. The capacitance and frequency values are good indicators of the electrochemical processes the resistance values correspond to [29,30]. In the present case, the capacitance values extracted from the Q2 element are in the range of $10^{-9} - 10^{-10}$ Farads/cm², indicative of the grain boundary impedance in oxygen ion conducting ceramics [31,32]. The capacitance values in the 10^{-7} - 10^{-5} Farad/cm² range suggest an electrochemical process at the Ag electrode/GDC electrolyte contact, such as oxygen reduction/evolution [31-33]. For all GDC samples, at 300 °C, the summit frequency for the bulk contribution to the ionic conduction remains higher than the maximum measurable frequency range of 10^5 Hz., and hence, this process is manifested as a series ASR in the impedance spectra (Figure 5.4).

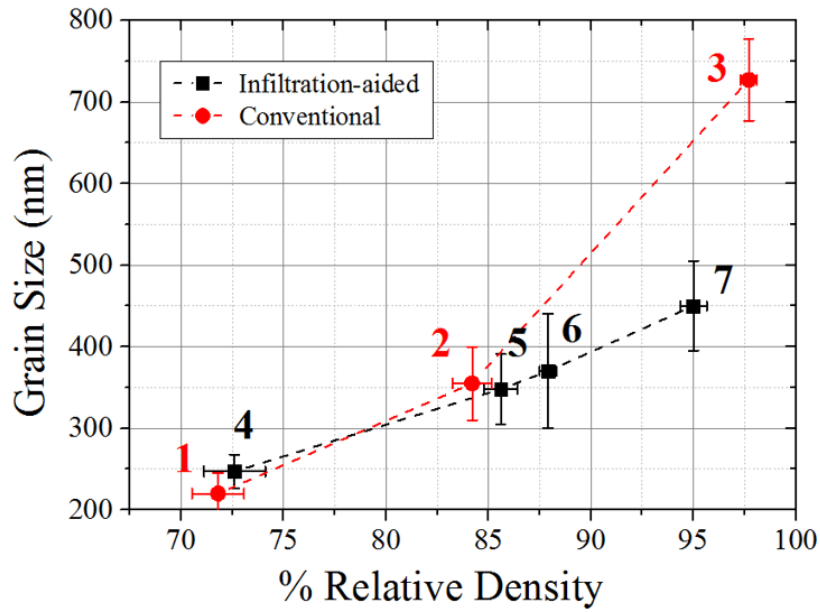


Figure 5.3. Variation of grain size with relative density for all samples 1-7.

Table 5.2. Area specific bulk (grain) and grain boundary resistances, along with the capacitance and summit frequency values extracted from the equivalent circuit fitting of the EIS data collected at 300°C.

Code Number	ASR ₁ (Ω.cm ²)	ASR ₂ (Ω.cm ²)	Capacitance from Q ₂ (nF)	Summit Frequency (kHz)	ASR ₃ (Ω.cm ²)	Capacitance from Q ₃ (μF)	Summit Frequency (Hz)
1	1480	19300	0.12	50	55500	0.60	1.6
2	1360	3430	0.41	63	36550	0.80	5
3	637	1110	1.35	63	13150	1.60	12
4	1140	6880	0.28	50	41200	0.55	3.1
5	924	3790	0.45	50	34960	0.72	6.3
6	939	2380	0.61	63	19560	0.95	7.9
7	678	973	1.04	80	11200	1.45	12.5

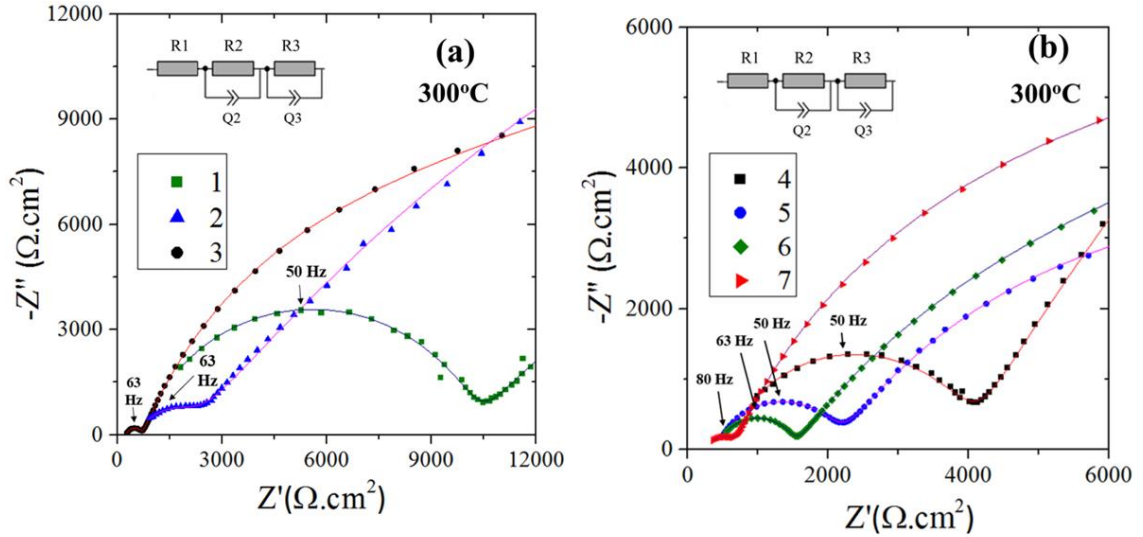


Figure 5.4. High frequency portions impedance spectra measured at 300°C for GDC fabricated by (a) conventional (b) infiltration-aided sintering along with their equivalent circuit fitting lines. The equivalent circuit models used to fit data are given as insets

For a clear understanding of the effect of microstructure on the electrical conductivity of GDC, bulk and grain boundary resistivities (ρ_b and ρ_{gb} , respectively) are calculated via Equation 5.1, where L is sample thickness, ρ and ASR are resistivity and area specific resistance respectively, both of which are applicable to bulk or grain boundary specifically.

$$\rho = \frac{ASR}{L} \quad (5.1)$$

Since the total resistivity (ρ_t) is the sum of bulk (ρ_b) and grain boundary resistivities (ρ_{gb}), contribution of grain boundary resistivity to the total resistivity can be determined by $\rho_{gb} / (\rho_{gb} + \rho_b)$, the variation of which depending on the grain size for the GDC ceramics fabricated by infiltration-aided sintering and conventional sintering are provided in Figure 5.5. At 300 and 350 °C and in the majority of the samples at 400 °C, the grain boundary resistivity is the dominant factor governing the total resistivity in all samples (Figures 5.5a and b). The blocking effect of the grain boundaries in doped ceria has been reported in the literature extensively [3,34-38] and has been attributed to i) space charge layer formation and ii) segregation of resistive, silicious impurities therein. The prevalence of gain boundary resistivity over the total resistivity appears to be less pronounced with increasing grain size and measurement temperature (Figures 5.5a-c).

In general, the effect of grain size on the $\rho_{gb}/(\rho_{gb} + \rho_b)$ value is due to the decrease in the number of grain/grain boundary interfaces that the oxygen ion needs to cross in the perpendicular direction to the grain boundary as the grain size increases, in agreement with the results observed in the literature [35, 38-40]. The decrease in the $\rho_{gb}/(\rho_{gb} + \rho_b)$ value with increasing measurement temperature has also been observed in the literature [35] and implies that ion transport perpendicular to the grain boundary is associated with a larger activation energy than through grain.

As mentioned earlier, achievement of high density is accompanied by a significant grain growth in GDCs fabricated by conventional sintering (Sample 3), while those subjected to infiltration-aided sintering retain a microstructure with fine grains (Sample 7, Figure 5.3). It is seen in Figure 5.5a that, despite the significantly larger grain size in sample 3 than in sample 7, they exhibit similar $\rho_{gb}/(\rho_{gb} + \rho_b)$ values at 300 °C, i.e., in the range of 0.6, while at higher temperatures sample 7 exhibits a much lower $\rho_{gb}/(\rho_{gb} + \rho_b)$ value than does sample 3 (Figures 5.5b and c). For example, at 400 °C, ρ_{gb} is no longer the larger part of $(\rho_{gb} + \rho_b)$ in sample 7, while in sample 3, this still is not the case (Figure 5.5c). To analyze this finding, the specific grain boundary resistivity term (ρ_{gb}^s), also used in the literature [34,38-42], representing the inherent property of the grain boundary, free from the effects of grain boundary thickness (δ_{gb}) and grain size (d_g) is introduced here (Equation 5.2).

$$\rho_{gb} = \frac{\delta_{gb} \times \rho_{gb}^s}{d_g} \quad (5.2)$$

When the ρ_{gb} and d_g values obtained from the experiments conducted on samples 3 and 7 are plugged into Equation 5.2, ($\delta_{gb} \times \rho_{gb}^s$) values of 0.201 $\Omega \cdot \text{cm}^2$ and 0.092 $\Omega \cdot \text{cm}^2$ respectively are obtained at 300 °C. The reason for this difference, thus the faster decrease in the grain boundary contribution to the total resistivity in the infiltration-aided sintering case, can either be the larger grain boundary thickness or the larger specific grain boundary resistivity of the conventionally sintered GDC (Sample 3). Smaller grain size corresponds to larger grain boundary volume available to dissolve any impurities, such as SiO_2 , that may cause an ion blocking effect and thus decrease ρ_{gb}^s [43,44]. On the other hand, since the experiments conducted in the literature on high purity ceria samples also have shown a similar effect [35,36,45], it can also be suggested that smaller grain size induces smaller δ_{gb} value, thus decreasing the overall ρ_{gb} . However, it should be noted

that the determination of the exact δ_{gb} value is certainly not straightforward due to the presence of space charge effect, even with high resolution transmission electron microscopy analyses [35].

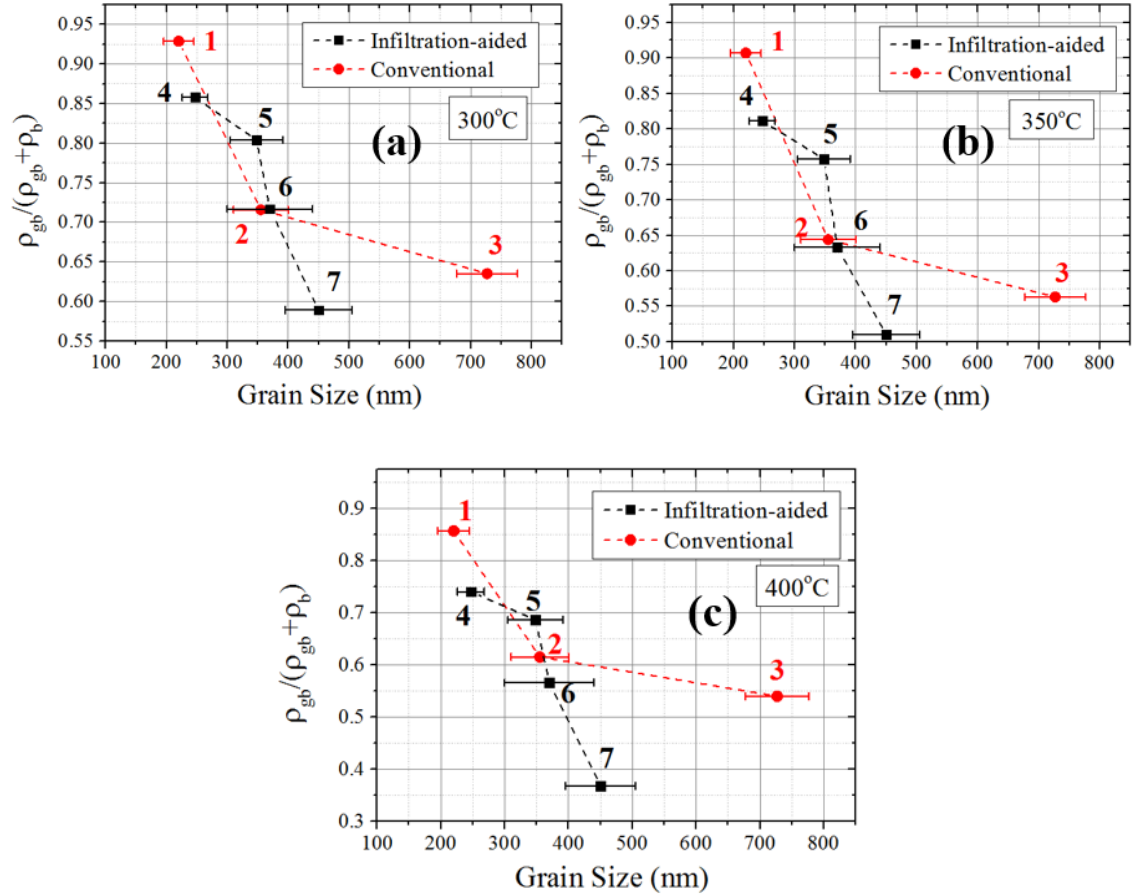


Figure 5.5. Effect of grain size on the ratio of grain boundary resistivity to total resistivity as measured at (a) 300, (b) 350 and (c) 400°C.

Temperature dependence of bulk and grain boundary conductivities (σ_b and σ_{gb} respectively), determined by taking the reciprocals of ρ_{gb} and ρ_b respectively, of GDC ceramics fabricated by conventional and infiltration-aided sintering is given in Figure 5.6. Since at temperatures exceeding 425°C, distinguishing the bulk and grain boundary contributions is practically not possible for GDC (as also was the case in Refs 8,30,46), these measurements were collected at 250-400°C in 25°C intervals, in air. To determine the effects of grain size on σ_b , samples fabricated by the two methods mentioned here having similar densities must be compared. This comparison yields that GDC ceramics fabricated by infiltration-aided sintering exhibit higher σ_b than the conventionally sintered ones at RDs below ca. 90%, despite similar densities and grain sizes while similar σ_b values are obtained in samples with RDs exceeding 95% regardless the grain size (Figure

5.5a). For example, although samples 1 and 4, and samples 2 and 5 have similar densities and grain sizes (Figure 5.3), those fabricated by infiltration-aided sintering exhibit higher σ_b values (i.e., samples 4 and 5 have higher σ_b than samples 2 and Sample 5) as seen in Figure 5.6a. On the other hand, samples 5 and 6 (both fabricated by conventional sintering) exhibit similar σ_b values (Figure 5.6a) and are determined to have similar densities and grain sizes (Figure 5.3). The comparison of the two high density samples (RDs exceeding 95%) fabricated by the two different methods discussed here (samples 3 and 7) yields similar σ_b values (Figure 5.6a) despite their significantly different grain sizes (Figure 5.3). A possible explanation is that in the case of infiltration-aided sintering, the number of coordination among the GDC particles constituting the porous scaffold is enhanced by the polymeric GDC precursor infiltration without a significant increase in RD, as suggested in Ref 21, causing an increase in the measured σ_b value. This argument is supported by the fact that no such difference in σ_b is observed between samples 5 and 6 – samples fabricated by infiltration-aided sintering with similar densities and grain sizes. In the case of samples with RDs exceeding 95%, the σ_b values are similar because the coordination between the GDC particles is at their maximum value in both cases.

A comparison among the σ_b values of GDC ceramics fabricated by the same method (i.e., conventional or infiltration aided sintering) suggests that bulk conductivity increases with increasing density (Figure 5.6a) as also reported in the literature [35, 47,48]. In addition, grain boundary conductivities (σ_{gb}) also appear to be affected by this parameter (Figure 5.6b). This apparent effect is due to the higher effective amounts of material within the measurement sample and, as discussed earlier in terms of specific grain boundary resistivity (ρ_{gb}^s) values of the highest density samples, ion transport perpendicular to the grain boundary appears to be more facile in the case of smaller grain size.

As all samples exhibit Arrhenius-type behaviors, the determination of activation energy (E_a) values is realized via Equation 5.3.

$$\sigma T = \sigma_0 \exp \left(\frac{-E_a}{kT} \right) \quad (5.3)$$

Here, σ is conductivity, E_a is the activation energy, σ_0 is the pre-exponential factor, T is the absolute temperature and k is the Boltzman's constant. Regardless the fabrication method, density or grain size, the E_a values for bulk conductivity lie in the

0.46-0.65 eV range (Figure 5.6a inset), while those for the grain boundary conductivity vary between 0.94 and 1.02 eV (Figure 5.6b inset). In general, these values explain the decrease in $\rho_{gb}/(\rho_{gb} + \rho_b)$ with increasing temperature (Figures 5.5a-c) and are consistent with those reported in the literature [39, 49-51]. In the literature, the reason for the higher activation energies observed for grain boundary conductivity in comparison to those determined for the bulk conductivity has been attributed both to the siliceous impurity segregation [37,45] and to the presence of a space charge layer at the grain boundaries [34,35].

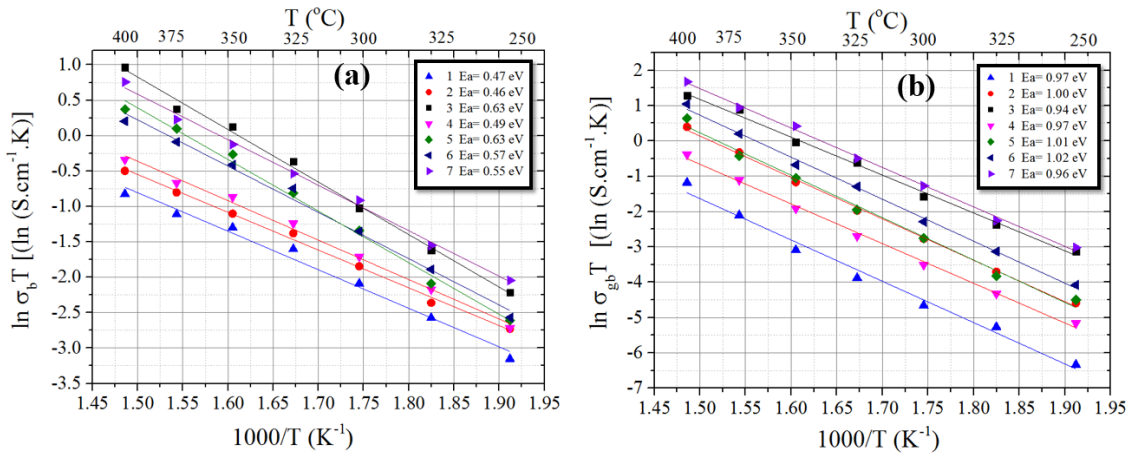


Figure 5.6. Arrhenius plots of (a) bulk (grain) and (b) grain boundary conductivities of the seven samples and their activation energies.

Figure 5.7 shows the temperature dependences of total conductivities of GDC ceramics fabricated by conventional and infiltration-aided sintering in the temperature range of 250 to 700°C, in air. A significant decrease in the slope of the electrical conductivity is observed in all samples at around 425 °C (Figure 5.7). A possible explanation of this phenomenon may be that since at low temperatures ρ_{gb} is dominant over ρ_b , the higher Ea value of the former prevails. On the other hand at higher temperatures, ρ_b with the lower Ea predominates. However, this argument is negated by the fact that ρ_{gb} is dominant in $(\rho_{gb} + \rho_b)$ by a small margin at 300 °C, which ceases to exist at ≥ 350 °C for samples 3 and 7, whereas these samples exhibit a change in the Ea of the total conductivity at much higher temperatures of 425 °C (Figure 5.7).

This change in slope has also been reported in the literature and has been attributed to the presence of associated $(Gd'_{Ce} - V_o^{\bullet\bullet})$ complexes at lower temperatures, which require extra energy to be dissociated and thusly provide available charge carriers for oxygen ion conduction [6,52]. On the other hand, at higher temperatures, these associated defects are already dissociated and the observed Ea is directly related to the migration energy of the

oxygen ions [35,52-53]. Therefore, the differences in activation energies in high and low temperature ranges provide the association energies of the complexes (i.e. $Gd'_Ce - V_o^{\bullet}$) [6]. This energy value does not appear to be affected by the densification method, but rather a gradual decrease with increasing density is observed (Table 5.3). The association energy values obtained for the highest density samples, i.e., samples 3 and 7 are found as 0.16 and 0.15 eV, respectively, agreeing well with the previous works of Steele et.al. (0.13 eV) [6], Zhou et.al. (0.12 eV) [35] and Huang et.al. (0.16 eV) [54].

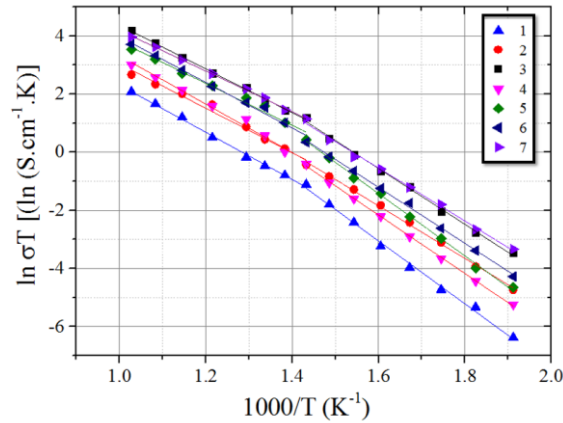


Figure 5.7. Temperature dependences of the total conductivities of all samples and their activation energies.

Regardless the fabrication method, evidently, electrical conductivity at 600 and 700 °C increases with increasing relative density, as expected (Figures 5.8a and b). The samples with RD values exceeding 95% obtained by conventional and infiltration-aided sintering (samples 3 and 7, respectively) exhibit very similar electrical conductivities over the whole temperature range (Figure 5.7). More specifically, at the targeted SOFC operation temperature of 700 °C, the GDC ceramics fabricated by conventional and infiltration-aided sintering has electrical conductivities of 0.068 and 0.054 S/cm, respectively (Figure 5.8b). These values are also in the range of what has been reported in the literature for dense GDC ceramics [6,35,49,55]. This suggests that, by infiltration-aided sintering, the sintering temperatures of GDC ceramics can be reduced by ca. 200 °C, without compromising electrical conductivity.

In the case of lower density samples, those fabricated by infiltration-aided sintering appear to exhibit higher total electrical conductivity in general (Figure 5.8), likely related to the higher number of coordination among the GDC particles ensured by the polymeric GDC precursor infiltration [21].

Table 5.3. Variation of activation energy of total electrical conductivity in the lower and higher temperature range. T* refers to the transition temperature and is 425°C for all samples in the present case.

Sample Code	Ea at T<T*	Ea at T>T*
1	0.93	0.70
2	0.82	0.67
3	0.83	0.65
4	0.89	0.72
5	0.87	0.68
6	0.83	0.64
7	0.78	0.61

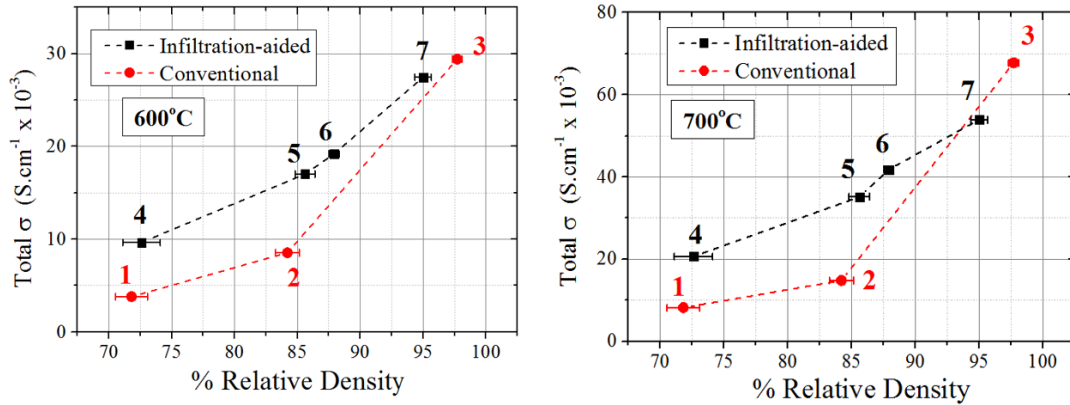


Figure 5.8. Variation of total electrical conductivity with relative density for all samples

So far, infiltrated GDC electrolytes sintered at 1200°C are shown to be highly dense and to perform well as far as their electrical conductivities are concerned. However, in addition to sufficient ionic conductivity, a suitable SOFC electrolyte material must also be impervious to hydrogen and oxygen gases at the desired operating temperatures and exhibit high open circuit voltage (OCV). Therefore, to further demonstrate the usefulness of the infiltration-aided sintering technique for SOFC electrolyte fabrication, OCV measurements are conducted on samples coded 3 and 7 between 400 and 700°C under a humidified 10 % hydrogen – 90 % argon gas flow from the anode side and stagnant air conditions at the cathode side. In addition to these two samples, data from the literature are also included in the plots for comparison [56,57]. As can be seen in Figure 5.9, for both samples, OCV is highest around 450°C and gradually decreases with increasing temperature, as predicted by the Nernst Equation. At the targeted SOFC operating

temperature of 700 °C, the conventionally sintered, dense GDC ceramic exhibits OCV values of 0.92 V, while that fabricated by infiltration-aided sintering yields an OCV of 0.83 V. These values are close to what has been reported in the literature for dense GDC ceramics and are well in the acceptable range for SOFC applications.

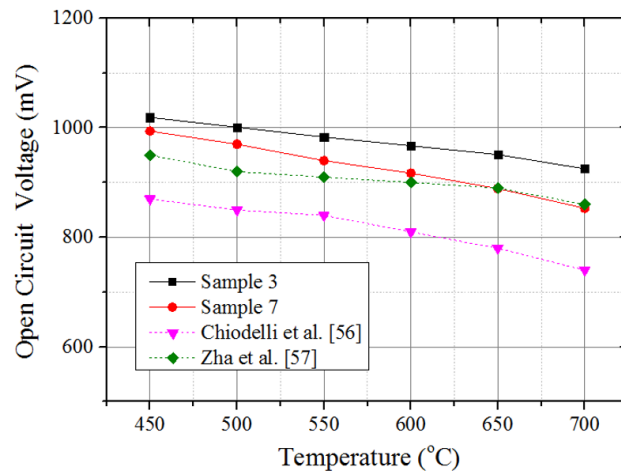


Figure 5.9. Open circuit voltage values obtained under stagnant air and 10% hydrogen – 90% argon at the cathode and anode sides respectively, at 450-700 °C in samples 3 and 7. Dotted lines are obtained from refs [56-57].

5.5. Summary

Reducing the densification temperatures of solid oxide fuel cell (SOFC) electrolyte materials is very desirable in order to i) avoid the coarsening of the anode microstructure, which is sintered together with the electrolyte layer in the anode supported SOFC fabrication scheme and ii) reduce energy consumption when manufacturing SOFCs. Our recent studies have shown that, using an infiltration-aided sintering method, the widely used gadolinia doped ceria (GDC) electrolyte ceramics could be densified up to a relative density (RD) of 95% at temperatures ca. 200 °C lower than those used in conventional sintering [21]. Achievement of high density in the GDC ceramics fabricated by infiltration-aided sintering was not accompanied by a significant grain growth, unlike the case of conventional sintering. In this work, for the first time in the literature, we have studied the electrical properties of the GDC ceramics fabricated by infiltration-aided sintering. Electrochemical impedance spectroscopy measurements were performed on GDC ceramics prepared by conventional and infiltration-aided sintering, which allowed the comparison of bulk and grain boundary conductivities at

≤ 350 °C and overall conductivities up to 700 °C obtained from ceramics fabricated via these two routes.

Regardless the fabrication method, at 300 and 350 °C, grain boundary resistivity dominated to total resistivity (i.e., $\rho_{gb} / (\rho_{gb} + \rho_b)$ value was between 0.5 and 1.0), which became less pronounced with increasing grain size and temperature, due to the smaller number of grain boundaries perpendicular to the oxygen ion motion and the higher activation energy of the oxygen ion transport therein. This dominance ceased to exist at 450 °C and at grain sizes of 450 nm in samples prepared by infiltration-aided sintering, but not in those fabricated by conventional sintering, even at a grain size of 727 nm, suggesting a higher specific grain boundary resistivity – grain boundary thickness product ($\delta_{gb} \times \rho_{gb}^s$) in the former.

Upon the comparison of grain and grain boundary conductivities of the samples fabricated by conventional and infiltration-aided sintering, it was found that, regardless the fabrication method, the grain boundary conductivities increased with increasing grain size, as expected. The grain conductivity of the ceramics fabricated by infiltration-aided sintering was larger in samples with less than 90% RD, due possibly to the enhanced coordination among the GDC particles that make up the porous GDC scaffold upon polymeric GDC precursor infiltration. This was also the case in the total electrical conductivity measurements. However, samples with RDs $\geq 95\%$, the maximum coordination of particles had been achieved, thus, similar bulk and total conductivity values were obtained.

In order to further demonstrate the usability GDC ceramics fabricated by the infiltration-aided sintering method as SOFC electrolytes, open circuit voltage (OCV) measurements were performed at 400-700 °C, under humidified 10% hydrogen – 90% argon and stagnant air atmospheres from anode and cathode sides respectively. OCV values of 0.84 and 0.93 V obtained from dense GDC ceramics fabricated by infiltration-aided and conventional sintering, respectively, suggests that the former method is also suitable for SOFC electrolyte fabrication.

Acknowledgements

This project is supported by TUBITAK (The Scientific Research Council of Turkey) through project no. 116R072. Authors would like to thank different labs in both

Izmir Institute of Technology and Gebze Technical University for their helps in materials characterization.

5.6. References

- [1] Inaba, H.; Nakajima, T.; Tagawa, H. *Solid State Ionics* **1998**, *106*, 263.
- [2] Inaba, H.; Tagawa, H. *Solid State Ionics* **1996**, *83(1)*.
- [3] Horovistiz, A.; Rocha, R.; Muccillo, E. *Ceramics International* **2013**, *39(5)*, 5887–5892.
- [4] Minh, N. Q. *Journal of the American Ceramic Society* **1993**, *76(3)*, 563–588.
- [5] Tsai, T.; Barnett, S. A. *Journal of Electrochemical Society*, **1998**, *145(5)*, 1696.
- [6] Steele, B.C.H.; *Solid State Ionics* **2000**, *129*, 95-110.
- [7] Flegler, A. J.; Burye, T. E.; Yang, Q.; Nicholas, J. D. *Ceramics International* **2014**, *40(10)*, 16323–16335.
- [8] Rahaman, M.; Zhou, Y. *Journal of the European Ceramic Society* **1995**, *15(10)*, 939–950.
- [9] Bao, W.; Chang, Q.; Meng, G. *Journal of Membrane Science* **2005**, *259(1-2)*, 103–109.
- [10] Masini, A.; Strohbach, T.; Šiška, F.; Chlup, Z.; Dlouhý, I. *Materials* **2019**, *12(2)*, 306.
- [11] Nguyen, X.-V.; Chang, C.-T.; Jung, G.-B.; Chan, S.-H.; Huang, W.; Hsiao, K.-J.; Lee, W.-T.; Chang, S.-W.; Kao, I.-C. *Energies* **2016**, *9(9)*, 701.
- [12] Kleinlogel, C.; Gauckler, L. J. *Advanced Materials* **2001**, *13(14)*, 1081–1085.
- [13] Kleinlogel, C.; Gauckler, L. J. *Solid State Ionics* **2000**, *135*, 567.
- [14] Taub, S.; Williams, R. E.; Wang, X.; McComb, D. W.; Kilner, J. A.; Atkinson, A. *Acta Materialia* **2014**, *81*, 128–140.
- [15] Spiridigliozzi, L.; Biesuz, M.; Dell’Agli, G.; Bartolomeo, E. D.; Zurlo, F.; Sglavo, V. M. *Journal of Materials Science* **2017**, *52(12)*, 7479–7488.
- [16] Biesuz, M.; Sglavo, V. M. *Journal of the European Ceramic Society* **2019**, *39(2-3)*, 115–143.

- [17] Kleinlogel, C.; Gauckler, L. J. *Journal of Electroceramics* **2000**, *5*(3), 231–243.
- [18] Fagg, D. P.; Kharton, V. V.; Frade, J. R. *Journal of Electroceramics* **2002**, *9*, 199–207.
- [19] Zhang, T. S.; Ma, J.; Kong, L. B.; Chan, S. H.; Hing, P.; Kilner, J.A. *Solid State Ionics* **2004**, *167*, 203–207.
- [20] Zhang, C.; Sunarso, J.; Zhu, Z.; Wang, S.; Liu, S. *Solid State Ionics* **2017**, *310*, 121–128.
- [21] Sındıraç, C.; Çakırlar, S.; Büyükaksoy, A.; Akkurt, S. *Journal of the European Ceramic Society* **2019**, *39*(2-3), 409–417.
- [22] Vohs, J. M.; Gorte, R. J. *Advanced Materials* **2009**, *21*(9), 943–956.
- [23] Jiang, S. P. *International Journal of Hydrogen Energy* **2012**, *37*, 449–470.
- [24] Jasinski, P.; Petrovsky, V.; Suzuki, T.; Petrovsky, T.; Anderson, H. U. *Journal of The Electrochemical Society* **2005**, *152*(2).
- [25] ASTM C20-00(2015), Standard Test Methods for Apparent Porosity, Water Absorption, Apparent Specific Gravity, and Bulk Density of Burned Refractory Brick and Shapes by Boiling Water, *ASTM International*, West Conshohocken, PA, **2015**, www.astm.org
- [26] Badwal, S. P. S.; Fini, D.; Ciacchi, F. T.; Munnings, C.; Kimpton, J. A.; Drennan, J. *Journal of Materials Chemistry A* **2013**, *1*(36), 10768.
- [27] Chourashiya, M.; Patil, J.; Pawar, S.; Jadhav, L. *Materials Chemistry and Physics* **2008**, *109*(1), 39–44.
- [28] Mendelson, M. I. *Journal of the American Ceramic Society* **1969**, *52*(8), 443–446.
- [29] Guo, X.; Waser, R. *Progress in Materials Science* **2006**, *51*(2), 151–210.
- [30] Anjaneya, K.; Nayaka, G.; Manjanna, J.; Govindaraj, G.; Ganesha, K. *Journal of Alloys and Compounds* **2013**, *578*, 53–59.
- [31] Pérez-Coll, D.; Marrero-López, D.; Núñez, P.; Piñol, S.; Frade, J. *Electrochimica Acta* **2006**, *51*(28), 6463–6469.
- [32] Gerstl, M.; Navickas, E.; Friedbacher, G.; Kubel, F.; Ahrens, M.; Fleig, J. *Solid State Ionics* **2011**, *185*(1), 32–41.
- [33] Anjaneya, K.; Nayaka, G.; Manjanna, J.; Govindaraj, G.; Ganesha, K. *Journal of Alloys and Compounds* **2013**, *578*, 53–59.

- [34] Guo, X.; Sigle, W.; Maier, J. *Journal of the American Ceramic Society* **2003**, *86*(1), 77–87.
- [35] Zhou, X.-D.; Huebner, W.; Kosacki, I.; Anderson, H. U. *Journal of the American Ceramic Society* **2004**, *85*(7), 1757–1762.
- [36] Tschope, A.; Kilassonia, S.; Birringer, R. *Solid State Ionics* **2004**, *173*(1-4), 57–61.
- [37] Wang, D. Y.; Nowick, A. *Journal of Solid State Chemistry* **1980**, *35*(3), 325–333.
- [38] Avila-Paredes, H. J.; Choi, K.; Chen, C.-T.; Kim, S. *Journal of Materials Chemistry* **2009**, *19*(27), 4837.
- [39] Wang, Z.; Kale, G. M.; Tang, X. *Journal of Materials Science* **2014**, *49*(8), 3010–3015.
- [40] Lee, K.-R.; Lee, J.-H.; Yoo, H.-I. *Journal of the European Ceramic Society* **2014**, *34*(10), 2363–2370.
- [41] Kim, D. K.; Cho, P.-S.; Lee, J.-H.; Kim, D.-Y.; Park, H.-M.; Auchterlonie, G.; Drennan, J. *Electrochemical and Solid-State Letters* **2007**, *10*(5).
- [42] Lee, J.-H.; Mori, T.; Li, J.-G.; Ikegami, T.; Komatsu, M.; Haneda, H. *Journal of The Electrochemical Society* **2000**, *147*(7), 2822.
- [43] Martin, M. C.; McCartney, M. L. *Solid State Ionics* **2003**, *161*, 67-79.
- [44] Verkerk, M.; Middelhuis, B.; Burggraaf, A. *Solid State Ionics* **1982**, *6*(2), 159–170.
- [45] Gerhardt, R.; Nowick, A. S. *Journal of the American Ceramic Society* **1986**, *69*(9), 641–646.
- [46] Chourashiya, M.; Patil, J.; Pawar, S.; Jadhav, L. *Materials Chemistry and Physics* **2008**, *109*(1), 39–44.
- [47] Souza, E. C. C.; Chueh, W. C.; Jung, W.; Muccillo, E. N. S.; Haile, S. M. *Journal of The Electrochemical Society* **2012**, *159*(5).
- [48] Hara, A.; Hirata, Y.; Sameshima, S.; Matsunaga, N.; Horita, T. *Journal of the Ceramic Society of Japan* **2008**, *116*(1350), 291–297.
- [49] Reddy, K. R.; Karan, K. *Journal of Electroceramics* **2005**, *15*(1), 45–56.
- [50] Bowman, W. J.; Zhu, J.; Sharma, R.; Crozier, P. A. *Solid State Ionics* **2015**, *272*, 9–17.
- [51] Christie, G. M.; van Berkel, F.P.F. *Solid State Ionics* **1996**, *83*, 17.

- [52] Ramesh, S.; Raju, K. C. J. *Electrochemical and Solid-State Letters* **2012**, *15*(3).
- [53] Zhang, C.; Li, C.-J.; Zhang, G.; Ning, X.-J.; Li, C.-X.; Liao, H.; Coddet, C. *Materials Science and Engineering: B* **2007**, *137*(1-3), 24–30.
- [54] Huang, K.; Feng, M.; Goodenough, J. B. *Journal of the American Ceramic Society* **1998**, 357–362.
- [55] Coles-Aldridge, A. V.; Baker, R. T. *Solid State Ionics* **2018**, *316*, 9–19.
- [56] Chiodelli, G.; Malavasi, L. *Ionics* **2013**, *19*(8), 1135–1144.
- [57] Zha, S.; Xia, C.; Meng, G. *Journal of Power Sources* **2003**, *115*(1), 44–48.

CHAPTER 6

CONCLUSIONS

Reducing the operating temperature of conventional SOFCs is one of the most important obstacles for full commercialization of this clean energy source. This reduction is essential to reduce the cost of the system and to extend the lifespan of the cell. Intermediate Temperature SOFC (IT-SOFC) has been getting popular in the last two decades because of these improvement possibilities. Some approaches have been proposed to overcome performance issues arising from temperature reduction since cell reactions are mostly thermally activated processes (i.e., oxygen conductivity). These approaches are mostly based on electrode and electrolyte layers because of the fact that polarization losses of the cell are dominated by performance issues in these layers. Therefore, this dissertation is focused on tailoring the microstructure of these two layers by using polymeric precursors which lead to nano-sized particles. In contrast with traditional aqueous precursor solutions, polymeric solutions give rise to particles that are mixed homogeneously in nano-sized dimensions without much agglomeration. GDC and LSCF are state-of-the-art electrolyte and cathode materials, respectively. Hence, these two materials have been selected to be used in this thesis.

In the second chapter, a thin layer of the cathode (air electrode) is deposited symmetrically by using polymeric precursor solutions of LSCF and LSCF-GDC (60%-40% volume percentage mixture). Promising results are obtained, especially in single phase LSCF. EIS measurements depict that approximately $0.6 \Omega \cdot \text{cm}^2$ electrode polarization is obtained at 600°C . However, in conflict with general view of literature, the addition of GDC into the LSCF solution lowered the electrochemical activity. However, GDC addition leads to a better microstructural dispersion, and hence, electrochemical longevity is obtained over 100h. This contradiction was explained by XPS analysis. It is observed that Fe segregation occurs on the surface of single phase LSCF since Co segregation takes place on the LSCF-GDC cathode surface, as opposed to the findings in the literature (i.e. A-site segregation). Furthermore, another reason for this contradiction can be explained as the addition of GDC (ionic conductor phase) caused a reduction of the electro-catalytical active area of LSCF.

Infiltration is another facile method which gives superior control over the electrode microstructure. Due to low-temperature calcination, infiltration technique has advantages to overcome co-sintering performance and longevity issues. Thus, in chapter 3, two different polymeric electrocatalyst ($\text{La}_{0.6}\text{Sr}_{0.4}\text{Co}_{0.2}\text{Fe}_{0.8}\text{O}_3$ - LSCF) and the polymeric mixture of electrocatalyst ($\text{La}_{0.6}\text{Sr}_{0.4}\text{Co}_{0.2}\text{Fe}_{0.8}\text{O}_3$ - LSCF) and ionic conductor $\text{Ce}_{0.9}\text{Gd}_{0.1}\text{O}_{2-\delta}$ (GDC) are infiltrated into the previously sintered porous GDC scaffold. Therefore, improved electrode performance was aimed via increasing electrocatalyst/ionic conductor interfacial area. EIS measurements indicate that an increasing number of infiltration cycles lead to an enhancement in electrode performance 45x for LSCF and 30x for LSCF+GDC infiltration. Further loading induces a poisoning effect in the electrode performance and these effects can be seen in Nyquist diagrams. Longevity test depicts that addition of GDC phase into the LSCF phase in polymeric precursor solution leads to stability over 60 hours. Same phenomena are also observed in Chapter 2.

Having success in developing cathode layers with improved electrochemical performance by infiltration, tests were conducted to see if infiltration could be employed to enhance densification of the electrolyte at lower temperatures. The added benefit of this was in ensuring co-sintering without compromising performance. Thus, infiltration of GDC polymeric precursor inside into the previously fired 60% dense GDC allows filling the pores and eventually decreasing the sintering temperature without using any sintering additive which effect the electrochemical properties of GDC. In Chapter 4, microstructural evolution is investigated, and 95% dense GDC is obtained at 1200°C instead of 1400°C which is required for conventional solid state sintering method. In Chapter 5, these densified electrolytes were analyzed by EIS methods to check their ionic conductivities and OCV values which is important for practical use. Observations indicated that GDC electrolytes could be densified by GDC infiltration and still could provide sufficient electrochemical properties which offers an alternative for co-sintering in SOFC applications.

VITA

Can SINDIRAÇ was born in 1987 in İzmir-TURKEY. After he graduated with a BS degree from Mechanical Engineering Department in Karadeniz Technical University in 2010, he earned his M.Sc. degree in 2013 from Mechanical Engineering Department in Izmir Institute of Technology. Between the years of 2012-2019, he has been working as a research assistant at Mechanical Engineering Department of Izmir Institute of Technology (IZTECH). His research interests are cathodes and electrolytes of solid oxide fuel cells, their synthesis and characterizations. Some of his publications are listed below:

Selected Journal Papers:

- [1] Sındıraç, C.; Akkurt, S. *International Journal of Hydrogen Energy* **2016**, *41*(40), 18157-18165.
- [2] Sındıraç, C.; Çakırlar, S.; Büyükaksoy, A.; Akkurt, S. *Journal of the European Ceramic Society* **2019**, *39*(2-3), 409–417.
- [3] Sındıraç, C.; Büyükaksoy, A.; Akkurt, S. *Solid State Ionics* **2019**, *340*, 115020.
- [4] Sındıraç, C.; Büyükaksoy, A.; Akkurt, S. *Journal of Sol-Gel Science and Technology* **2019**.

Selected Conference Proceedings:

- [1] Sındıraç, C.; Büyükaksoy, A.; Akkurt, S. *Proceedings of the First Workshop for Young Ceramists*, November 26-27, **2018**, Bologna, Italy, ISBN: 978-88-7586-599-3, page:139-142
- [2] Akkurt, S.; Sındıraç, C.; Büyükaksoy, A. *Proceedings of the 4th Anatolian Energy Symposium with International Participation*, Edirne, April 2018, ISBN: 978-975-374-224-5, page: 1214-1221